Prediction of Transition for Attached and Separated Shear Layers in Turbomachinery

by

Robin Blair Langtry B. Eng. (Aerospace)

A thesis submitted to the Faculty of Graduate Studies and Research
in partial fulfillment of the requirements for the degree of

Master of Applied Science
in Aerospace Engineering

Ottawa-Carleton Institute for Mechanical and Aerospace Engineering

Department of Mechanical and Aerospace Engineering

Carleton University
Ottawa, Ontario
Canada

Your file Votre référence
ISBN: 0-612-95898-1
Our file Notre référence
ISBN: 0-612-95898-1

PAGINATION ERROR.

TEXT COMPLETE.

ERREUR DE PAGINATION.

LE TEXTE EST COMPLET.

Abstract

A simple, new model is developed to predict the transition in attached and separated shear layers in turbomachinery. The model controls the onset of transition through the production of turbulence kinetic energy and is based on the value of the vorticity Reynolds number, a concept introduced by Van Driest and Blumer (1963). The model has been calibrated for use with the Menter (1994) SST turbulence model. No additional transport equations are solved. The new transition model has been validated against a large number of challenging experimental cases, including the ERCOFTAC T3 series (Savill, 1993a,b) of test cases and a low-pressure turbine blade operating at very low Reynolds numbers under steady conditions and subjected to periodically impinging wakes. For the attached shear layers, the predictions were as good as or better than those obtained with well-established empirical correlations. Surprisingly, the model gave good results even for cases where the transition occurred in the free shear layer of a separation bubble or was caused by a periodically impinging wake.

Acknowledgements

I would like to express my profound gratitude to my thesis supervisor, Professor S.A. Sjolander. His support and guidance during the course of this thesis was invaluable. I would also like to thank him for proposing the idea of attending graduate studies in the first place. I would be on a very different path right now if it were not for him and I am truly grateful.

I would also like to thank my colleagues, Ali Mahallati and Xue Feng Zhang for their insight and numerous thoughtful discussions. This thesis would never have been possible without the challenging experiments they conducted during the timeframe of this thesis. Finally, I would like to thank my family and especially Stacie Burchell for their love and encouragement.

Financial support for this study provided by the Natural Sciences and Engineering Research Council of Canada through a Research Grant (S.A. Sjolander) is gratefully acknowledged.

Table of Contents

List of Tables

List of Figures

Nomenclature

Cp	pressure coefficient, $p_{total}-p/(0.5\rho U_{ref}^2)$
Cf	skin-friction coefficient, T3 series: $\tau/(0.5\rho U_o^2)$; PAK-B: $\tau/(0.5\rho U_{ref}^2)$
Cf'	quasi-skin-friction coefficient, $\tau'/(0.5\rho U_{ref}^2)$
E	voltage reading from the surface hot film
E_o	zero velocity voltage reading from the surface hot film
FSTI	freestream turbulence intensity (percent), $100(2k/3)^{1/2}/U_{ref}$
k	turbulent kinetic energy
K	flow acceleration parameter, see Equation 3.33
l	turbulent length scale, $k^{1/2}/\omega$
L	axial reference length
p	local static pressure
p_{total}	inlet total pressure
Re_x	Reynolds number, $\rho L U_{ref}/\mu$
Re_θ	momentum thickness Reynolds number, $\rho\theta U_0/\mu$
$Re_{\theta t}$	transition onset momentum thickness Reynolds number, $\rho\theta_t U_0/\mu$
R_T	viscosity ratio, see Equation 3.12
R_y	wall-distance based turbulent Reynolds number, see Equation 3.13
Re_v	vorticity Reynolds number, see Equation 3.11
S	absolute value of strain rate, $(2\Omega_{ij}\Omega_{ij})^{1/2}$
S_{ij}	strain rate tensor, $0.5(\partial u_i/\partial x_j + \partial u_j/\partial x_i)$
U	local velocity
U_o	local freestream velocity
U_{ref}	inlet reference velocity
u'	local fluctuating streamwise velocity
u_τ	friction velocity, $(\tau/\rho)^{0.5}$
x/C, x/B_x	axial distance over axial chord
y	distance to nearest wall
y^+	distance in wall coordinates, $\rho y u_\tau/\mu$

δ	boundary layer thickness
ε	turbulence dissipation rate
θ	momentum thickness
λ_θ	pressure gradient parameter, $(\rho\theta^2/\mu)(dU/ds)$
μ	molecular viscosity
μ_t	eddy viscosity
ρ	density
τ	wall shear stress
τ'	quasi-wall shear stress, $((E^2 - E_o^2)/E_o^2)^3$
Ω	absolute value of vorticity, $(2\Omega_{ij}\Omega_{ij})^{1/2}$
Ω_{ij}	vorticity tensor, $0.5(\partial u_i/\partial x_j - \partial u_j/\partial x_i)$
ω	specific turbulence dissipation rate, ε/k

Subscripts

t	transition onset
s	streamline

Chapter 1
Introduction

Laminar to turbulent flow transition has been recognized as one of the most important phenomena in fluid flows that is not yet fully understood (Zheng et al, 1998). The accurate prediction of transition is particularly important for gas turbine engines where the onset and extent of transition can have a significant effect on the performance of the turbomachinery (Mayle, 1991). This is particularly true for low-pressure turbines which operate at low values of Reynolds number, especially at high-altitude cruise.

At the take off condition the Reynolds number through the low-pressure turbine is large which results in turbulent flow around the blades. However, at the high altitude cruise condition the Reynolds number is significantly reduced which results in a large amount of laminar flow on the turbine blades (Mayle, 1991). This usually produces a laminar separation bubble on the blade suction side that transitions in the free-shear layer and reattaches as turbulent flow. If the bubble fails to reattach the efficiency of the turbine blade will be significantly reduced. It has been estimated that a 1% improvement in the efficiency of a low pressure turbine would result in a saving of $52,000 per year on a typical airliner (Suzen and Huang, 2001). As a result, the ability to predict transition accurately is of great importance for the design of future, ever more highly-loaded but efficient turbines for gas turbine engines.

Recently, great strides have been made to improve the capability of computational fluid dynamics (CFD) codes and they now constitute a standard tool in the aerodynamic design cycle. Navier-Stokes codes are used routinely to predict with reasonable accuracy fully laminar or fully turbulent flows of great complexity (Zheng et al, 1998). If a reliable means of predicting transition from laminar to turbulent flow could be incorporated into the existing CFD codes this would greatly enhance their capabilities. This thesis will

present a new, relatively simple transition model which is compatible with current Navier-Stokes codes and appears to predict with good accuracy the transition in both attached and separated shear layers.

To be useful for turbomachinery design, a transition model should meet several requirements (Suzen et al, 2001):

(i) It must be sensitive to the flow physics that affect transition in turbomachinery, notably freestream turbulence intensity, strong pressure gradients and flow separation.

(ii) It must be computationally inexpensive. This disqualifies methods that require prior solution of the mean flow field, such as methods based on parabolized stability equations or the e^n type methods.

(iii) It should be fairly easy to incorporate into existing CFD codes and should be compatible with one or more widely-accepted turbulence models. Ideally, the transition model would be represented as an algebraic function so that no extra transport equations must be solved.

(iv) Finally, the transition model must be compatible with unstructured codes. This requirement is necessary because unstructured methods are becoming increasing popular due to their ability to model complicated geometries and reduce pre-processing time.

In this thesis a novel approach to simulating laminar to turbulent transition is proposed that satisfies all of the desired requirements. The approach is new and it uses Van Driest and Blumer's (1963) concept of vorticity Reynolds number to make a two-equation turbulence model capable of predicting transition under the influence of turbulence intensity, pressure gradient and flow separation.

In practice, most low-Reynolds number two-equation turbulence models are capable of simulating laminar to turbulent transition. However, these models suffer from the fact that the onset point occurs far too early and they do not properly reproduce the effects of pressure gradients or separation (Zheng et al, 1998). The new approach that is proposed here is to use the local vorticity Reynolds number to control the production of turbulent-kinetic-energy up to the onset of transition. It will be shown that this results in a two-equation turbulence model that is just as capable of reproducing experimental transition data as many of the commonly used empirical correlations.

A review of pertinent literature on boundary layer transition mechanisms is presented in Chapter 2. A summary of the different methods that are currently used to predict transition is also discussed in this chapter. Chapter 3 describes in detail the development of the new transition model and how it has been calibrated. The new transition model has been validated against a large number of diverse and challenging test cases. The predicted results for the ERCOFTAC T3-series of transitional test cases is detailed in Chapter 4. As well, the new transition model has been used to predict the experiment of Zhang (2002) on the PAK-B low-pressure turbine blade at steady conditions and influenced by a periodic impinging wake. The steady results are detailed in Chapter 5 and the unsteady results are detailed in Chapter 6. Finally, conclusions and recommendations for future work are discussed in Chapter 7.

Chapter 2
Literature Review

2.1 Introduction

The purpose of this chapter is to review previous research that has been conducted on laminar to turbulent transition in boundary layers. The first section of this chapter will discuss the various modes by which transition is generally believed to occur. The primary modes are often referred to as natural, bypass and separated flow transition. Recently, the unsteady effects of an impinging wake have been found to have a significant effect on the transition process. The impinging wakes usually cause earlier transition and this mode is often referred to as wake induced transition. As well, it has been determined experimentally that if the boundary layer is strongly accelerated it can revert from turbulent flow back to laminar flow. This mode has been classified as reverse transition (Mayle, 1991).

The second section of this chapter will summarize the various methods that have been used to predict transition along with their advantages and disadvantages. The major emphasis will be on evaluating the methods for their suitability towards industrial applications.

2.2 Transition Modes

2.2.1 Natural Transition

When the freestream turbulence level is low (<1 percent, Mayle (1991)) a laminar boundary layer becomes linearly unstable beyond a critical Reynolds number at which Tollmien-Schlichting waves start to grow. The instability is via a subtle mechanism whereby viscosity destabilizes the waves and they begin to grow very slowly. Because the growth is so slow, transition to turbulence might occur at a streamwise distance 20 times farther downstream from the starting position of linear instability (Durbin et al. 2002). Orderly transition occurs only after the waves have become nonlinear and inviscid mechanisms have come into play. At this point turbulent spots are born. The spots grow in the surrounding laminar layer until they eventually coalesce into a turbulent boundary layer. A schematic of the natural transition process is shown in Figure 2.1.

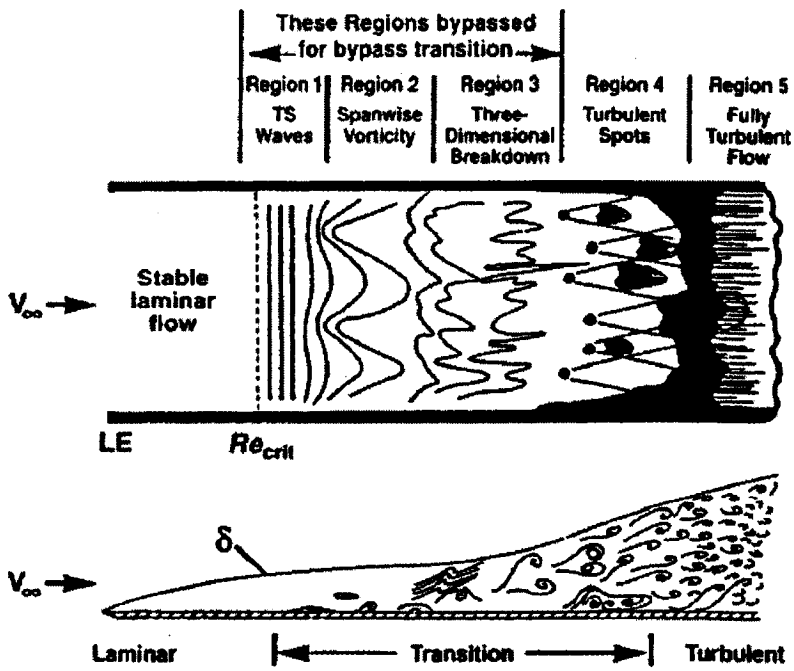

Figure 2.1 The natural transition process (from Schlichting, 1979)

2.2.2 Bypass Transition

For transition at high freestream turbulence levels, the first and possibly second and third stages of the natural transition process are completely bypassed such that turbulent spots are directly produced within the boundary layer by the influence of freestream disturbances (Mayle, 1991). It is often argued that for bypass transition linear stability is irrelevant and to date no one has been able to detect Tollmein-Schlichting waves when the freestream turbulence level was greater than 1 percent (Mayle, 1991). For this reason, a freestream turbulence level of 1 percent is often taken as the boundary between natural transition and bypass transition.

Bypass transition from a practical standpoint is often considered to start when the skin friction deviates from the laminar value. This has been shown to be the location where the first turbulent spots appear (Mayle, 1996a). As a result, everything that occurs before the spots are formed happens in a completely laminar boundary layer. However, measurements show that this pre-transitional flow is not steady and actually has significantly large levels of velocity fluctuations, often referred to as laminar fluctuations (Mayle, 1996a). This is clearly illustrated for a flat plate in Figure 2.2, where transition did not start until a Reynolds number of 1.3×10^5.

The growth of the laminar fluctuations is believed to be caused by the pressure fluctuations in the turbulent freestream (Mayle, 1996a). These pressure waves propagate into the boundary layer and similar to the Tollmien-Schlichting waves, cause the growth of velocity fluctuations until eventually they are large enough that turbulent spots form. The growth of the laminar fluctuations for a flat plate is shown in Figure 2.3. Interestingly, the growth becomes almost linear once the freestream turbulence level decreases below 1 percent.

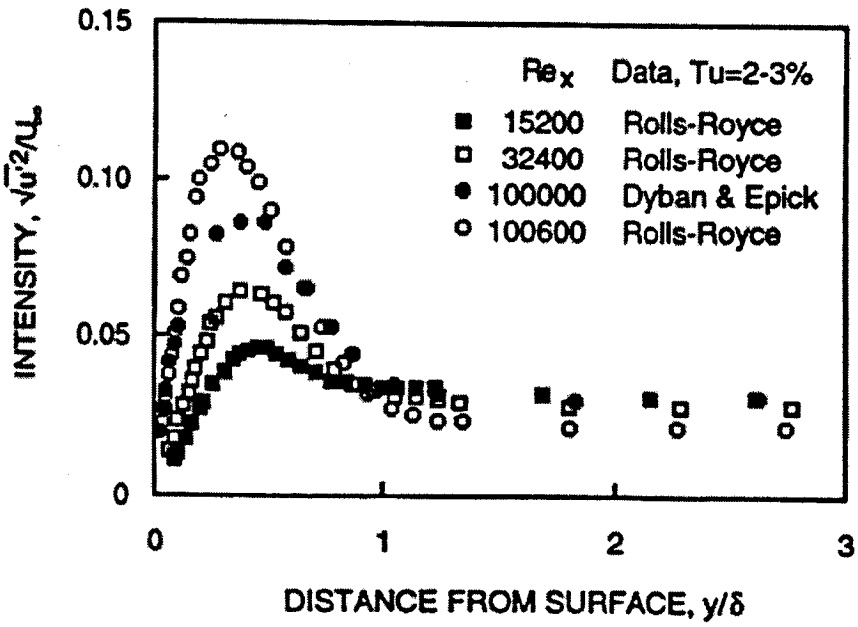

Figure 2.2 Fluctuations in a laminar boundary layer before the onset of transition (reproduced from Mayle, 1996a).

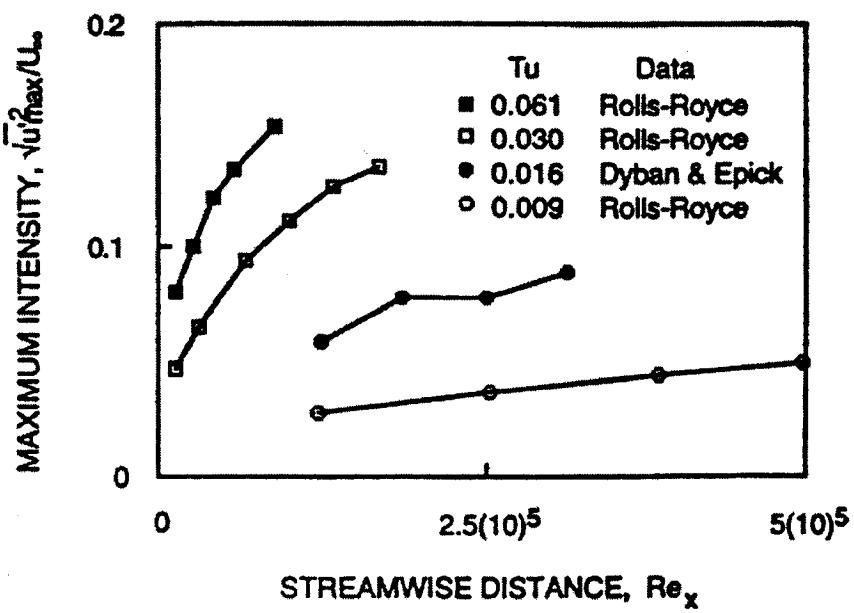

Figure 2.3 The growth of fluctuations in a laminar boundary layer before transition (reproduced from Mayle, 1996a).

2.2.3 Separated Flow Transition

When a laminar boundary layer separates, transition may occur in the free shear layer of the separated flow. In this case, due to the enhanced mixing present in turbulent flow, the shear layer may reattach. This reattachment forms a laminar-separation / turbulent-reattachment bubble on the surface (Mayle, 1991). This type of transition can occur behind boundary layer trip wires and also as a result of separation due to a strong adverse pressure gradient.

The bubble length depends on the transition process within the free shear layer and may involve all of the stages listed for natural transition. Because of this, it is generally accepted that the freestream turbulence level plays a large role in determining the length of the separation bubble. Traditionally, separation bubbles have been classified as long or short based on their effect on the pressure distribution around an airfoil (Mayle, 1991). Short bubbles reattach shortly after separation and only have a local effect on the pressure distribution. Long bubbles can completely alter the pressure distribution around an airfoil (see Figure 2.4). Since long bubbles produce large losses and large deviations in exit flow angles, they should be avoided (Mayle, 1991). Short bubbles on the other hand, can be used to trip the boundary layer and thus allow larger adverse pressure gradients downstream of the reattachment point. One of the major challenges lies in determining whether or not a separation bubble will be long or short. This is aggravated by the fact that small changes in either Reynolds number or angle of attack of an airfoil can cause a bubble to change dramatically from short to long (Mayle, 1996b). The sudden change in bubble length is often referred to as bursting. It can result in a dramatic loss of lift and could even cause the airfoil to stall if the bubble fails to reattach.

A schematic of a transitional separation bubble is shown in Figure 2.5. The forward portion of the bubble is a constant pressure region. It is comprised of a laminar shear layer that is inherently unstable due to the inflexion point in the velocity profile and the large distance away from the region of wall damping. The inflexion point promotes the growth of disturbances which eventually break down into turbulence at the location

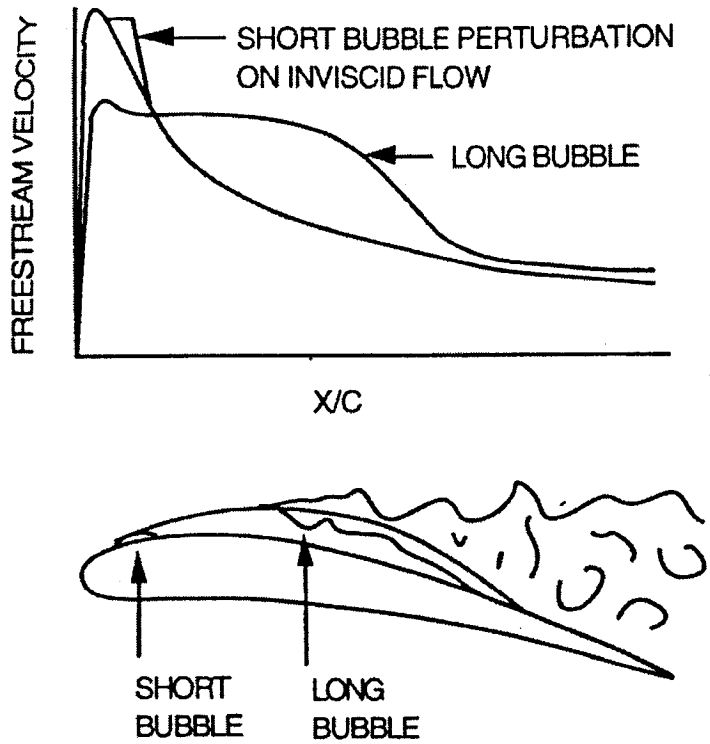

Figure 2.4 Separation bubble effects on suction side velocity distribution (reproduced from Mayle, 1996b).

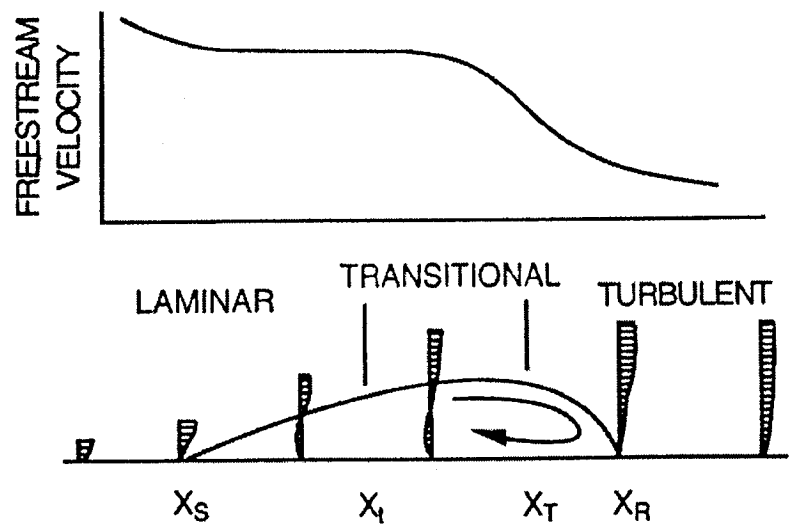

Figure 2.5 Velocity distribution over a separation bubble (reproduced from Mayle, 1996b).

marked X_t. The transition process is usually complete before the shear layer reattaches.

2.2.4 Wake Induced Transition

One very important instance of bypass transition arises in turbomachinery where the blade rows are subjected to periodically passing turbulent wakes. It has been found experimentally that the wakes are so disruptive to the laminar boundary layer that turbulent spots often form in the location where the wake impinges on the surface. From the available literature it is not clear whether the transition is caused by the enhanced turbulence in the wake or the freestream momentum deficit and the interaction of this with the boundary layer. It is for this reason that this mode of transition is usually differentiated from bypass transition and is often referred to as wake induced transition.

If one subtracts the unsteady velocity field by the time average value to obtain a relative velocity field, the wake can be visualized as a negative jet that impinges on the surface (Durban et al, 2002). This results in a backwards jet which is strongly destabilizing due to the inviscid instability mode. Shortly after the wake passes the flow breaks down and a turbulent spot is formed. A Direct Numerical Simulation (DNS) computation illustrating this phenomena is shown in Figure 2.6.

In between the wakes transition can occur via any of the other possible modes and this has been detected experimentally (Mayle, 1991). As the wake passes the boundary layer will slowly relax from turbulent flow to laminar flow. This region is often referred to as the calmed region (Howell et al, 2001). The calmed region has a full velocity profile which is very stable and does not separate in adverse pressure gradients as easily as a laminar profile. Howell et al (2001) have argued that it was this ability to withstand adverse pressure gradients that allowed the spots to keep the flow from separating.

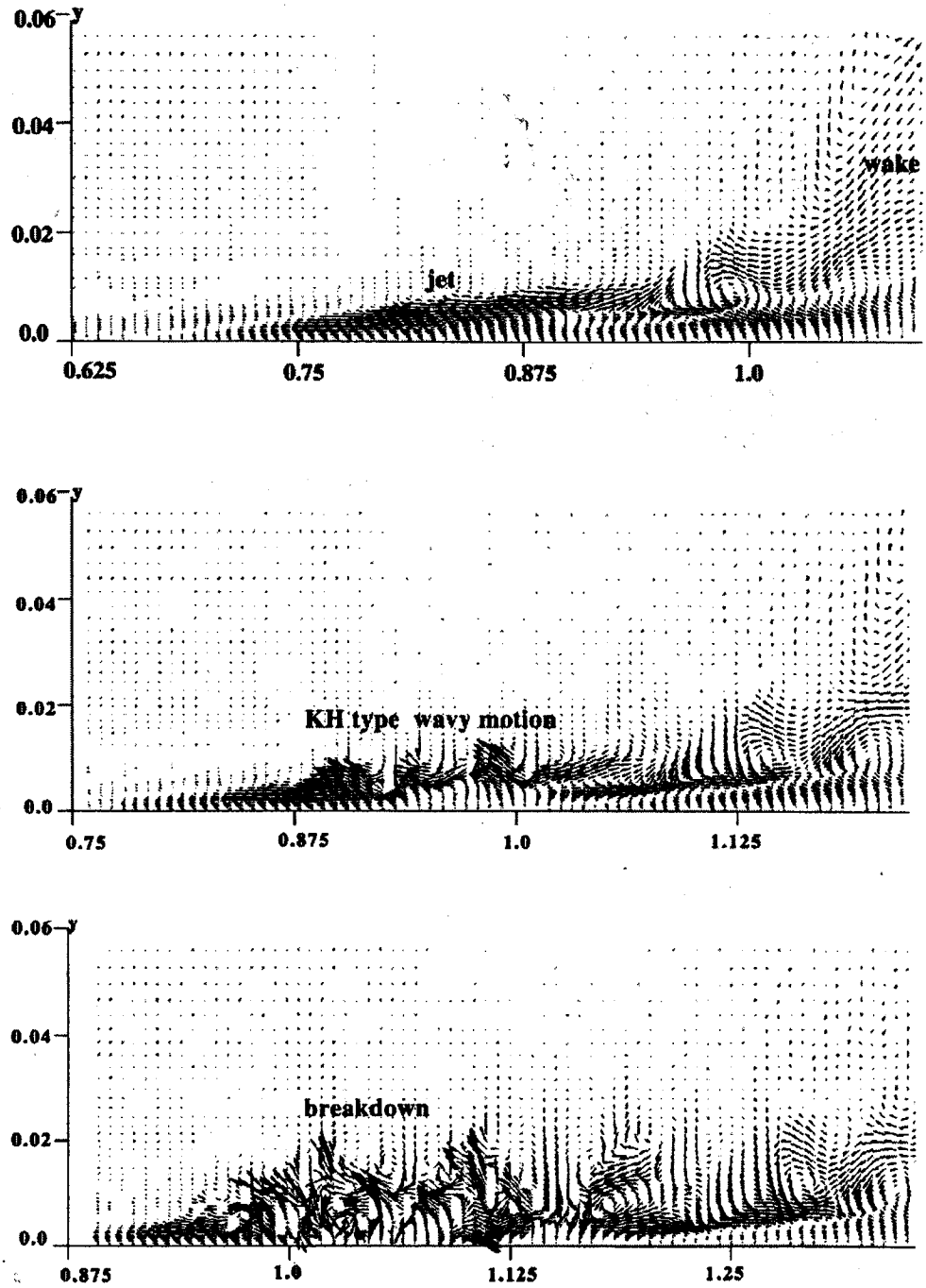

Figure 2.6 DNS simulation of the development of a backward jet in the relative velocity field and its breakdown to turbulence (reproduced from Durban et al., 2002).

A space-time (ST) diagram can be very useful for illustrating the unsteady transition process because it places the variations of boundary layer skin friction in time and space on a single diagram. An idealized example of an ST diagram for a low-pressure turbine is show in Figure 2.7. The y axis shows multiples of wake passing periods, the x axis indicates the position along the airfoil chord and the colour flood shows the surface skin friction. Transitional flows caused by wakes are labeled W, turbulent flow caused by separated flow transition is marked T, and calmed flow is marked C. The diagram illustrates two cases of wake induced transition each one with a different wake passing frequency. At the lower wake passing frequency (Figure 2.7a), the flow at the trailing edge of the blade is turbulent because of the wakes, then calmed and then turbulent again due to separated flow transition. If the time between wake passing periods is sufficiently short (Figure 2.7b) then the separation bubble will not have time to reestablish itself and thus the losses associated with the bubble will be diminished (Howell et al, 2001). Figure 2.8 illustrates the measured reduction in losses due to the suppression of the separation bubble by periodically passing wakes. A flap was mounted at the end of a turbine blade which allowed the turning angle to be increased. The lift ratio is defined as the ratio of produced lift to the baseline blade where the flap is not deflected

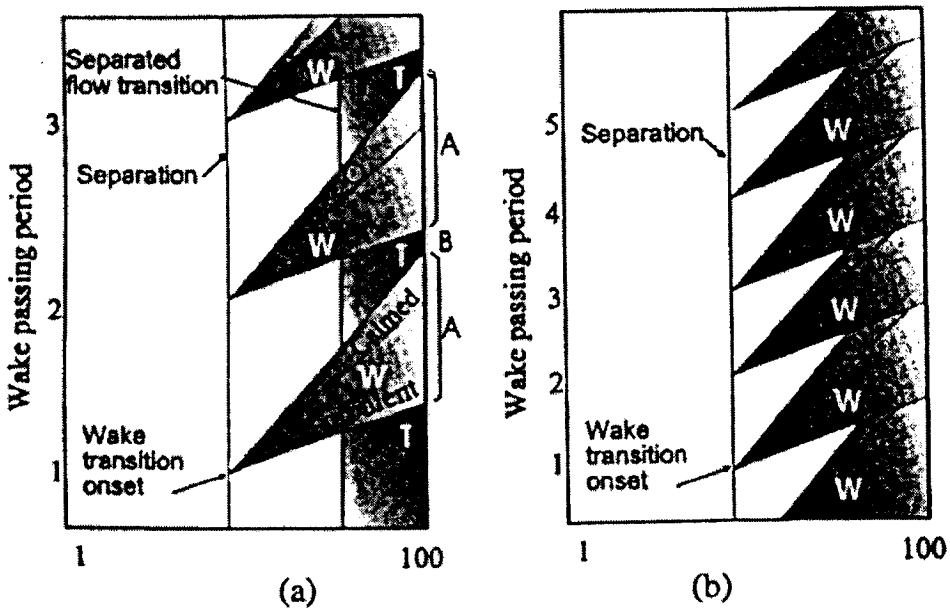

Figure 2.7 Idealized ST diagram of wake-induced transition showing two different wake passing frequencies (reproduced from Howell et al., 2001).

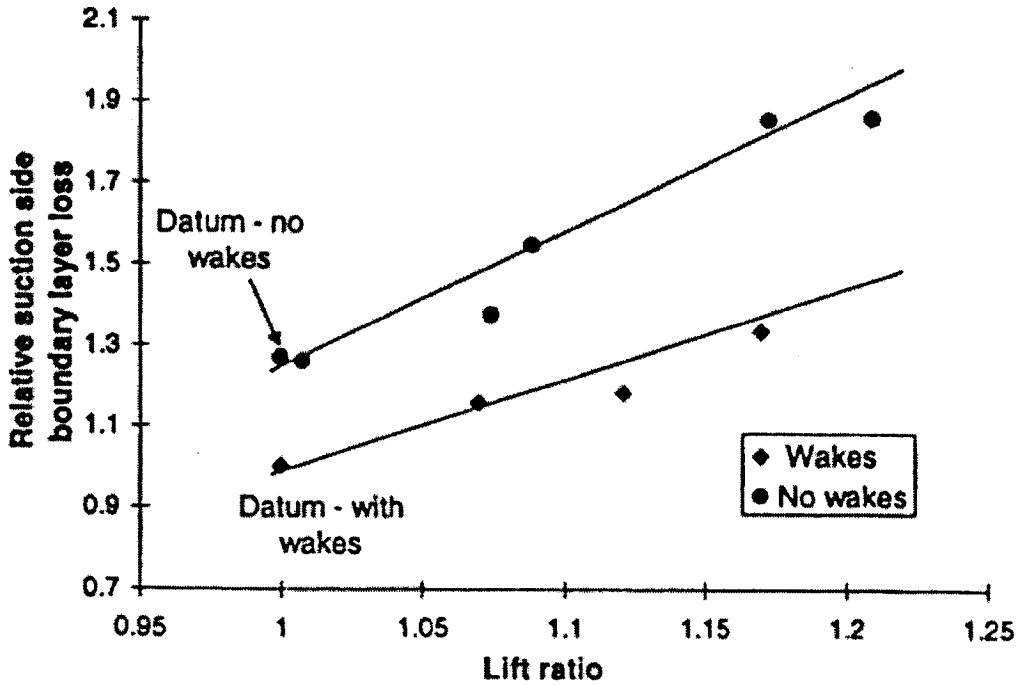

Figure 2.8 Variation in loss with increased lift (increased lift results in larger separation bubbles) for a turbine blade with and without wakes (reproduced from Howell et al., 2001).

2.2.5 Reverse Transition

Transition from turbulent to laminar flow is possible if the flow is strongly accelerated. This is often referred to as either "reverse" transition or "relaminarization". The acceleration on the trailing edge pressure side of most airfoils and on the leading edge suction side of most turbines is large enough to cause reverse transition (Mayle, 1991). There is not a lot of experimental data on reverse transition but it is know to occur when the acceleration parameter, $K = \upsilon/U^2(dU/dx)$, is greater than about $3x10^{-6}$ (Mayle, 1991). An example of reverse transition is shown in Figure 2.9.

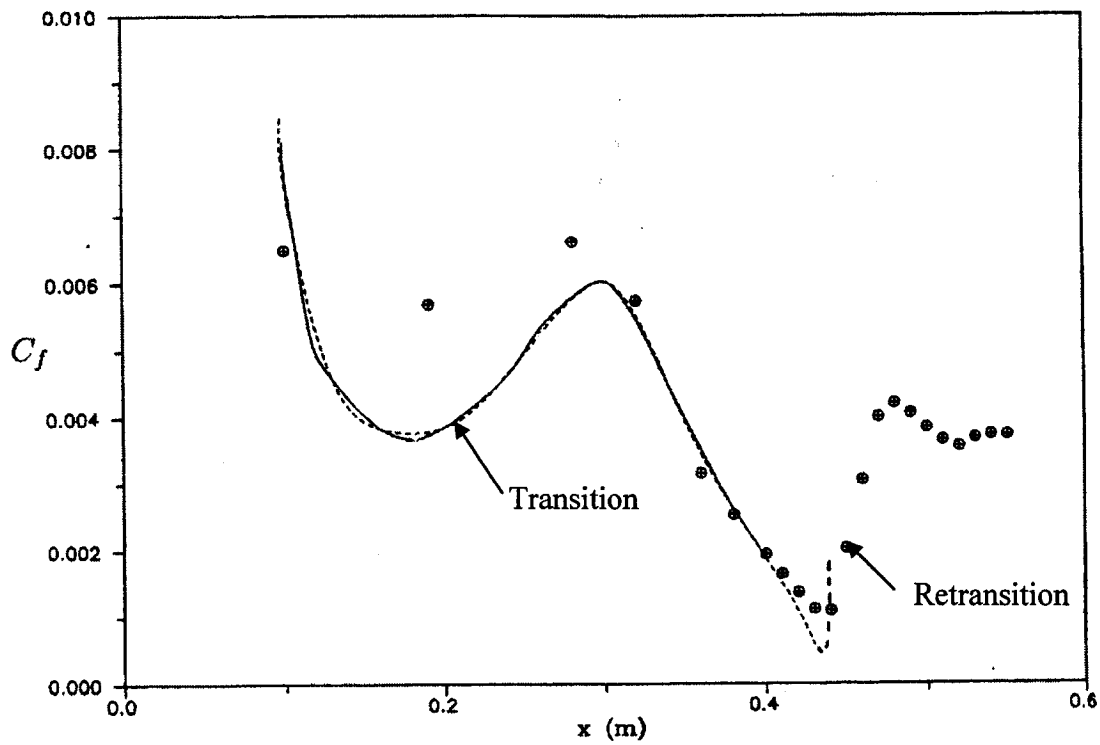

Figure 2.9 Relaminarisation and retransition with a freestream turbulence level of 0.1 percent (reproduced from Savill, 2002).

2.3 Transition Prediction

2.3.1 Direct Numerical Simulation

In principle, laminar flow break down, the development of turbulent spots and transition to fully turbulent flow can be simulated quit accurately using Direct Numerical Simulation (DNS) (Zheng et al, 1998). A DNS computation is performed by solving the full unsteady Navier-Stokes equations. Since there is no Reynolds averaging there is no requirement for turbulence closure from a turbulence model. In order to capture the small scales of turbulence a DNS computation requires an extremely fine grid. A DNS of transition on a flatplate is shown in Figures 2.10 and 2.11. This simulation had approximately 50 million grid points and was performed on a supercomputer with 64 processors in about four weeks.

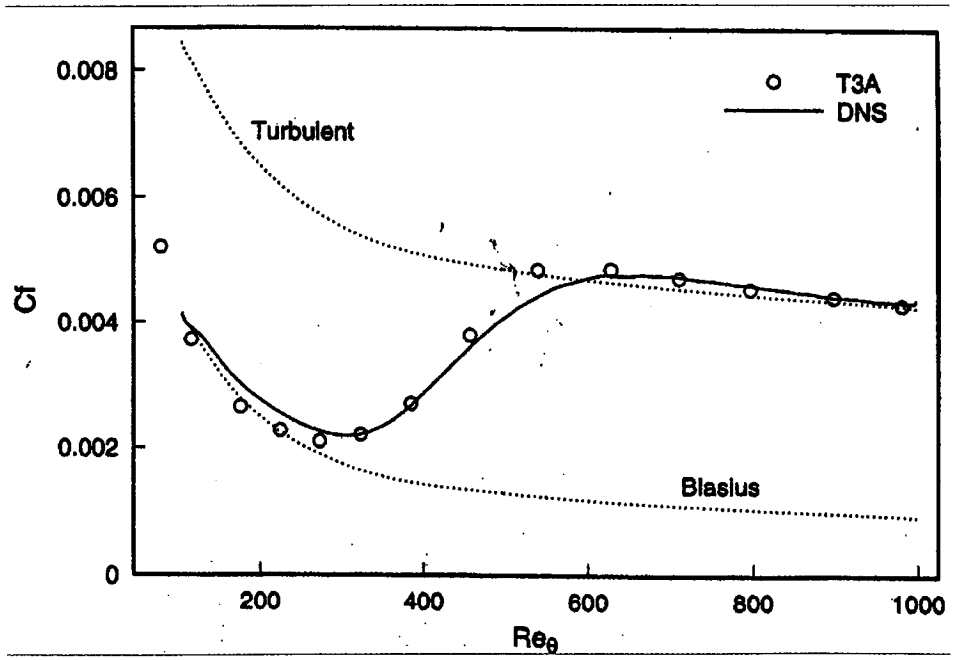

Figure 2.10 Direct Numerical Simulation of transition on a flatplate (reproduced from Durbin et al, 2002)

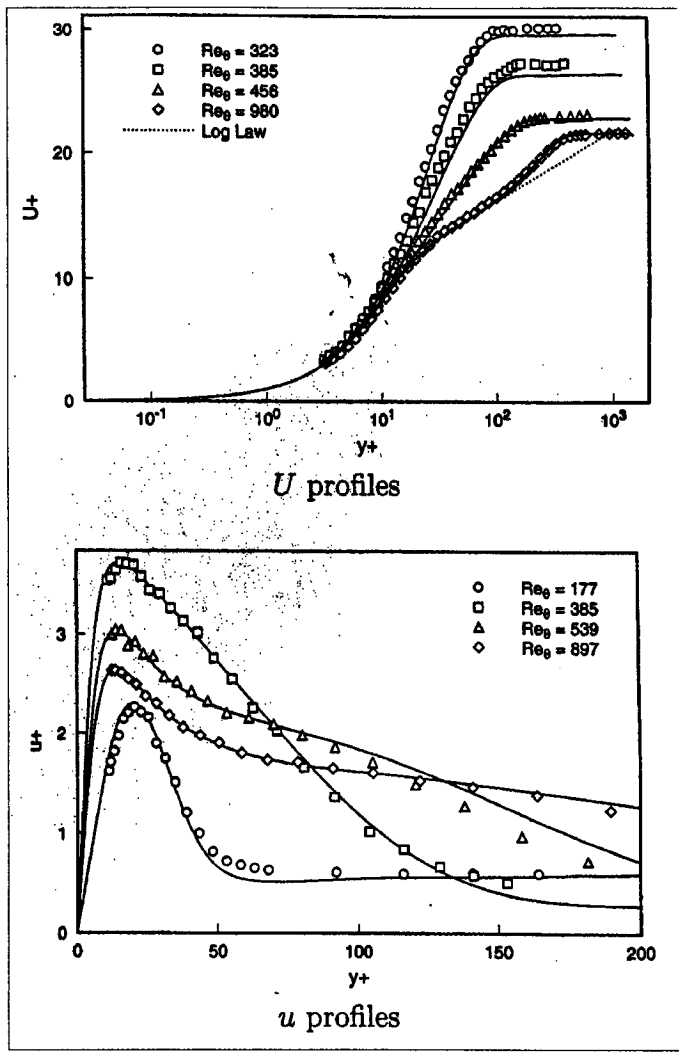

Figure 2.11 DNS and experimental profiles of mean (U) and fluctuating (u) velocities at various streamwise locations for the T3A test case (reproduced from Durbin 2002).

Clearly, DNS is not yet at the stage where it can serve as a practical tool for engineering design applications due to the large computing requirements. This will be the case for a long time as additional computing resources in industry are being used to simulate larger more complicated geometry, not for improved modeling. The strength of DNS lies in the wealth of full-field instantaneous and ensemble averaged data that is provided as well as the ability to prescribe precise inflow conditions (Durbin et al, 2002). DNS databases are quickly becoming an invaluable tool for developing and testing turbulence models as well as improving our understanding of fluid dynamics. However, it will be a very long time before DNS itself can replace turbulence/transition modeling.

2.3.2 e^n Method and Parabolized Stability Equations

One of the more widely used methods for predicting transition is the so-called e^n method. This method is based on linear stability theory and requires three successive steps (Zheng et al, 1998). The first step consists in the calculation of the laminar velocity and temperature profiles along the body of interest. In the second step, the local growth rates of the unstable waves are computed for each of these profiles. This can be accomplished by solving either the local stability equations or the Parabolized Stability Equations (PSE). In the third step, the local growth rates are integrated along each streamline in order to determine the *n* factor.

The major problem with the e^n method is that the n factor does not represent the amplitude of a disturbance in the boundary layer but rather the amplification factor from an initial unknown amplitude (Warren and Hassan, 1997). The initial amplitude of the disturbance in the boundary layer is related to the external disturbance environment through some generally unknown receptivity process. For this reason the *n* factor at the onset of transition is not universal and must be determined on a case by case basis. Typical values can vary from 7 to 9.

Another major problem with the e^n method occurs for separated flow transition where the onset of transition causes the boundary layer to reattach. In this case, often the purely laminar solution is massively separated and exhibits unsteady vortex shedding (Zheng et al, 1998). Since the steady solution is not available, the local growth rates can not be computed using the local stability equations or PSE and the e^n method is completely inappropriate for predicting these types of flows.

The e^n method can only be used to predict the onset of transition, it cannot be used to predict the subsequent transitional region. For this reason there is now growing interest in approaches that solve the non-linear Parabolized Stability Equations because the development of the unstable waves up to the weakly non-linear regime can be simulated

(Savill, 2002). An example of this is shown in Figure 2.12. This approach is still not appropriate for solving problems with separation induced transition.

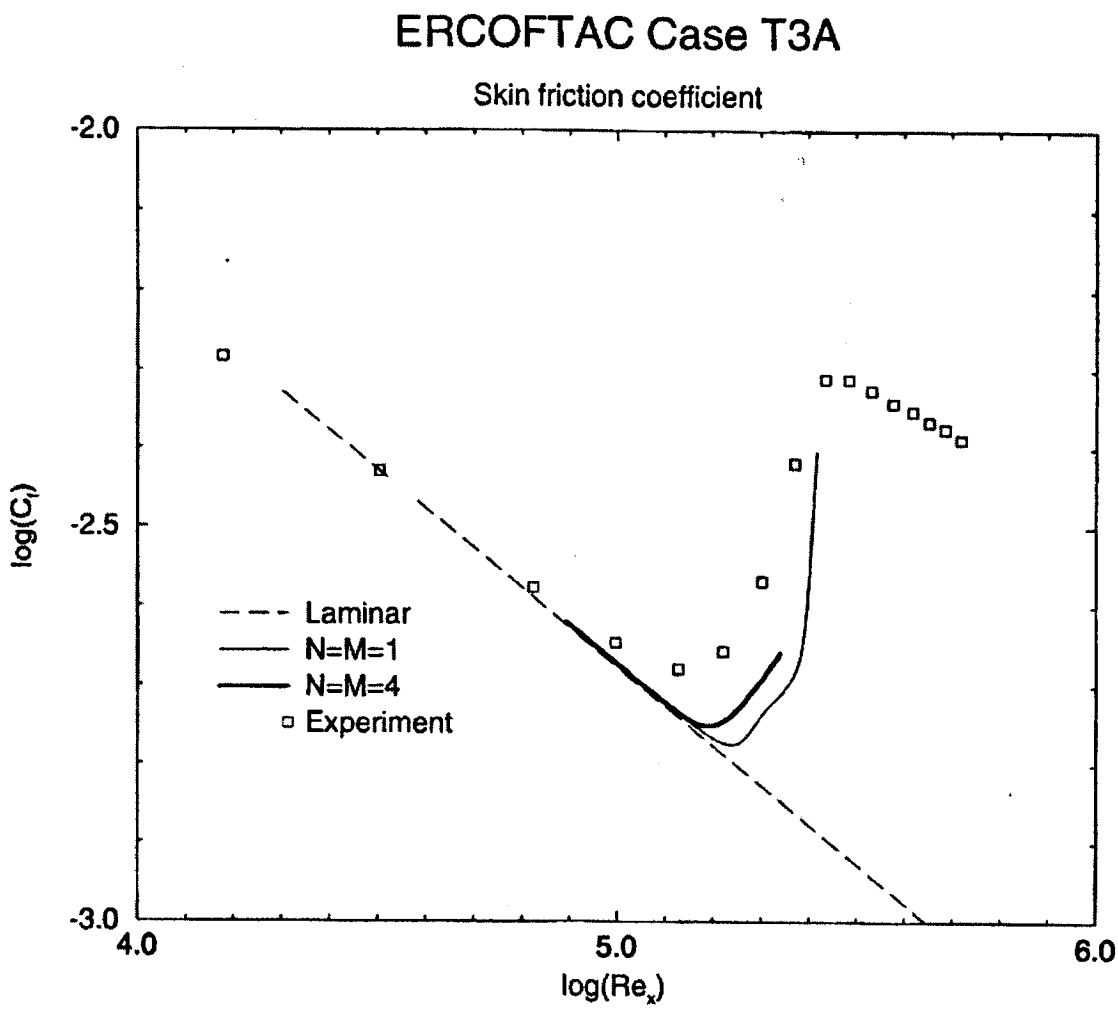

Figure 2.12 PSE predictions of skin friction (Cf) versus experimental data for a freestream turbulence of 3 percent (reproduced from Savill, 2002).

Finally, all the approaches based on linear stability theory are very difficult to implement in three-dimensional flows because of the need to track the growth of the unstable waves along the streamlines. This problem is aggravated by modern unstructured parallel Navier-Stokes codes because often the grid lines are not normal to the body surface and the streamline can pass through different grid partitions. For all of these reasons methods based on linear stability are not favored for general prediction of transition.

2.3.3 Empirical Correlations

One of the most common ways of predicting boundary layer transition in industrial CFD codes is to employ empirical correlations. The empirical correlations usually relate the freestream turbulence intensity (Tu) to the transition Reynolds number based on momentum thickness ($Re_{\theta t}$). A typical example is the Mayle (1991) correlation which is shown in Figure 2.13. This correlation is based on some fairly recent high quality experimental data for transition onset. Another popular correlation is that of Abu-Ghannam and Shaw (1980). This correlation is shown in Figure 2.14. It is based on older data but it can account for the effect of pressure gradient on the transition onset location.

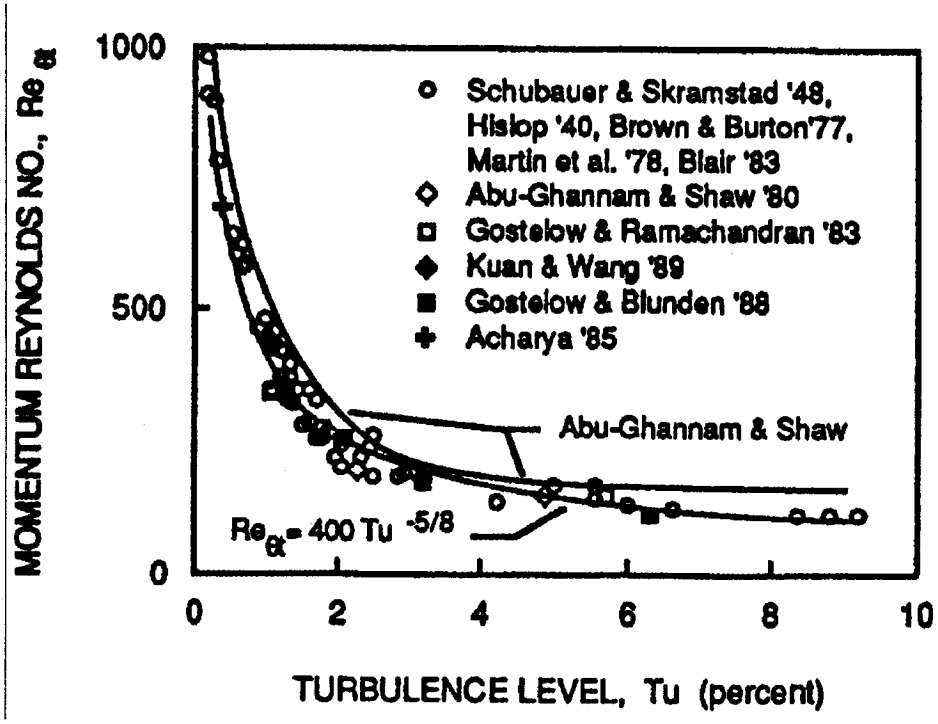

Figure 2.13 The Mayle (1991) correlation for transition momentum thickness Reynolds number (reproduced from Mayle, 1991).

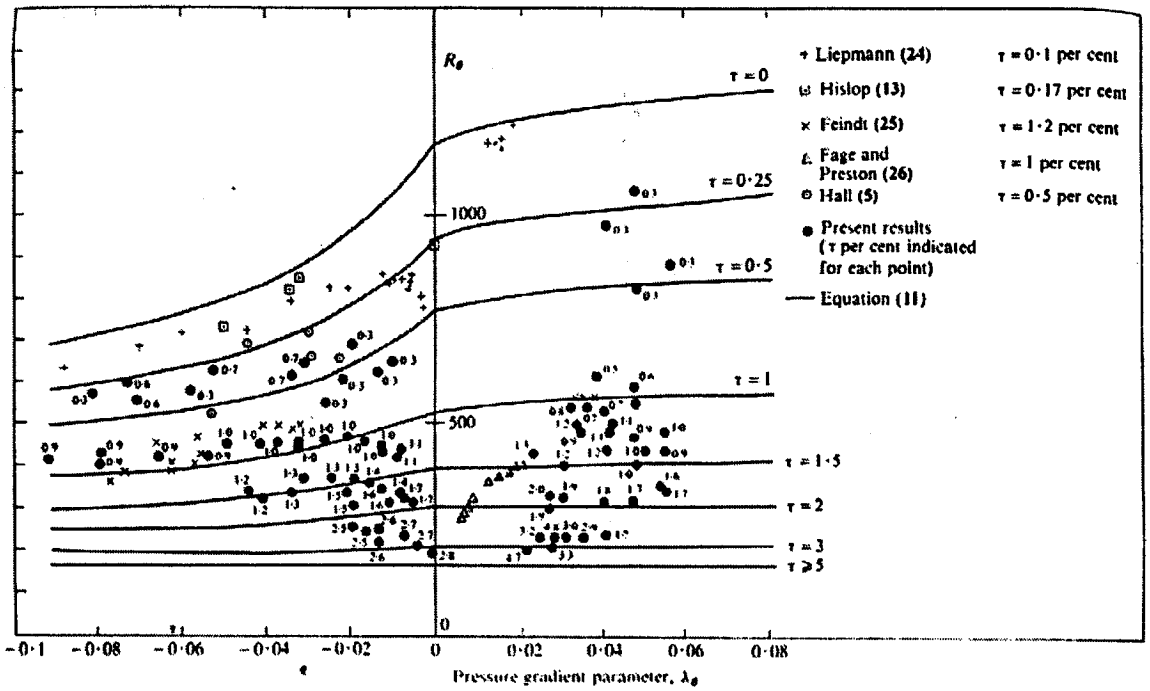

Figure 2.14 The correlation of Abu-Ghannam and Shaw (1980) (reproduced from Abu-Ghannam and Shaw, 1980).

In order to employ an empirical correlation for transition onset the laminar solution around the body of interest must first be calculated. After this has been accomplished the boundary layer quantities are than integrated to obtain the momentum thickness Reynolds number (Re_θ) at every point on the body. Transition onset is then assumed to occur at the position where the local value of the momentum thickness Reynolds number exceeds that predicted by the correlation. Once the starting location of transition has been determined a turbulence model is turned on and the subsequent flow development is calculated. Although only as reliable as the underlying correlations, this approach can give fairly satisfactory results.

The main problem with empirical correlations is the necessity to compare actual momentum thickness Reynolds numbers with the critical value from the correlation. In unstructured CFD codes it is very difficult to determine a proper integration strategy for the boundary layer quantities because often the grid lines are not normal to the surface.

This problem is further aggravated by parallel codes where half the boundary layer could be located on a different grid partition.

2.3.4 Low-Re Turbulence Models

The preferred method for predicting transition with unstructured codes is to use a low-Reynolds number two-equation turbulence model. This is because these models are relatively easy to implement and are applicable to predicting transition even in 3d flows. Low-Reynolds number turbulence models employ damping functions that are designed to model viscous sublayer behavior so that wall functions are not required (Schmidt and Patanker, 1991).

A large number of low-Reynolds number turbulence models have been developed since the concept was first proposed by Jones and Launder (1973). A few of these models were found to predict transition at reasonable Reynolds numbers when the freestream turbulence level was sufficiently high. However, the ability of these models to predict transition is coincidental and is due to the similarities between the viscous sublayer and the developing laminar boundary layer where the production of turbulence is damped (Schmidt and Patanker, 1991). The transition predicted by a number of low-Reynolds number turbulence models is shown in Figures 2.15 and 2.16. Clearly, none of the models is very good at predicting the onset location or the subsequent transitional region. According to Zheng et al (1998) without further modifications low Reynolds number turbulence models tend to predict the onset of transition far too early, do not have the proper sensitivity to strong pressure gradients and do not predict transition well in separated shear layers

One notable exception is the low Reynolds number k-ε model developed by Biswas and Fukuyama (1994). This model has been shown to predict attached transition quite accurately when the freestream turbulence level was greater than 1 percent. Biswas and

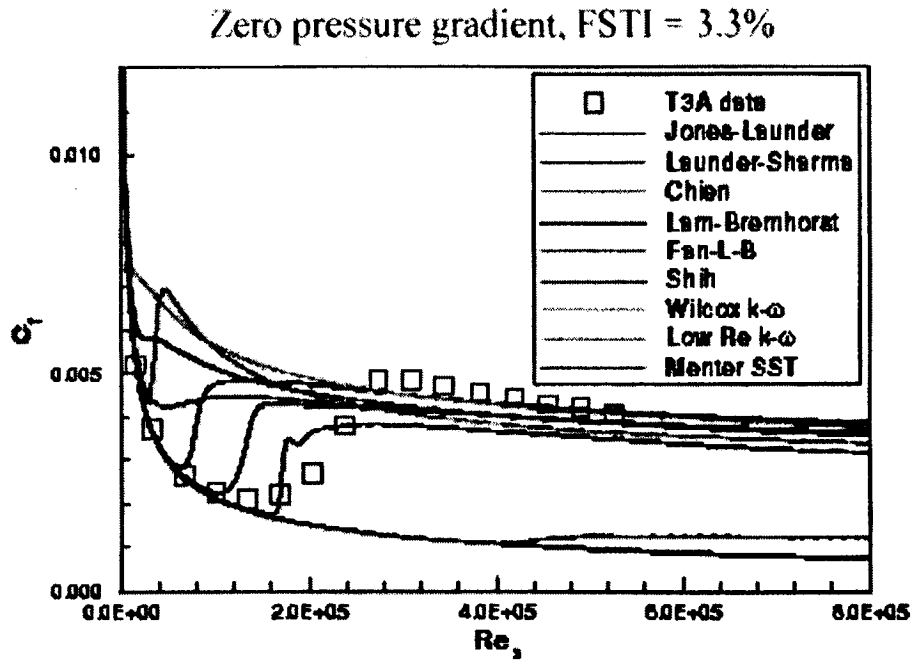

Figure 2.15 Transition in zero pressure gradient predicted by a variety of low-Reynolds number turbulence models (courtesy of Suzen and Huang).

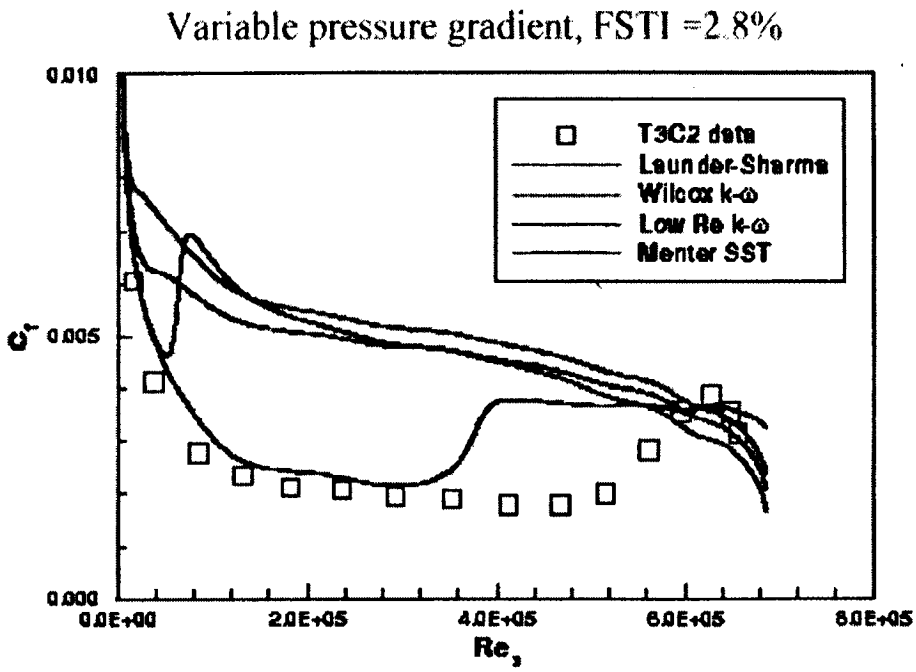

Figure 2.16 Transition in variable pressure gradient predicted by a variety of low-Reynolds number turbulence models (courtesy of Suzen and Huang).

Fukuyama successfully applied their model to variety of test cases which included transition on flat plates as well as a nozzle guide vane. The results for a flat plate are shown in Figures 2.17 and 2.18.

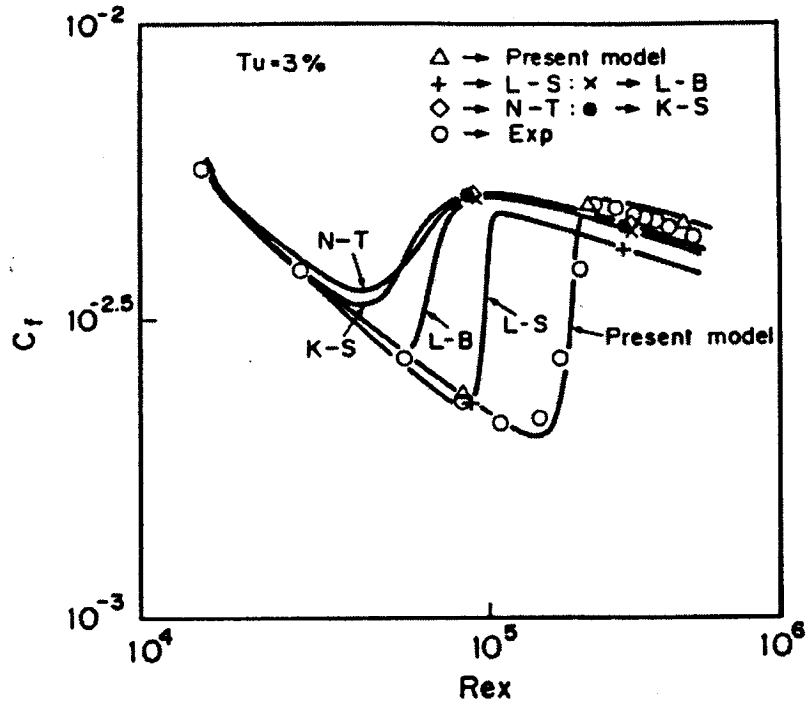

Figure 2.17 Skin friction (Cf) predicted by the low Reynolds number turbulence model of Biswas and Fukuyama (1994) (reproduced from Biswas and Fukuyama, 1994).

The present author implemented the Biswas and Fukuyama model into a Navier-Stokes code at the beginning of this thesis and while the predictions of attached transition onset and length were reasonable, the model had poor numerical robustness. In order to converge a solution the equations for k and ε had to be under-relaxed by a factor of 0.1. This resulted in a solution time that was approximately ten times longer then what would be required for a fully turbulent computation. For the case of separation induced transition on a flat plate a steady converged solution could not be obtained.

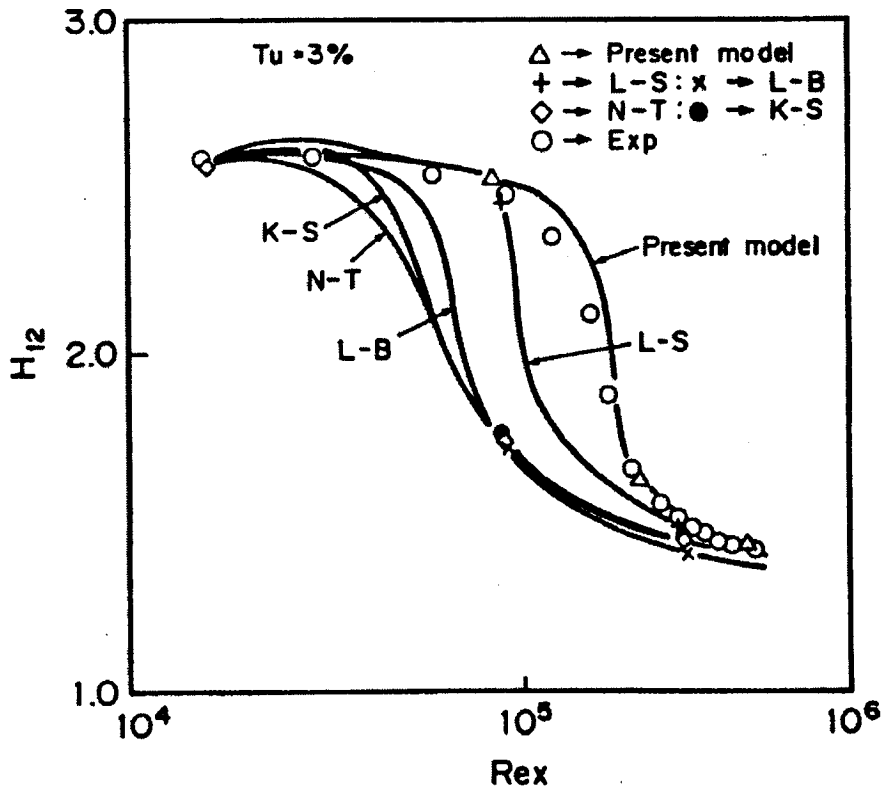

Figure 2.17 Shape factor (H) predicted by the low Reynolds number turbulence model of Biswas and Fukuyama (1994) (reproduced from Biswas and Fukuyama, 1994).

In order for a low Reynolds number turbulence model to be useful for industrial predictions of transition not only must it be accurate but it must also be robust. To date none of the low Reynolds number models satisfy both of these requirements and there is clearly a need in industry for such an accurate and robust model. It is for these reasons that the present thesis was undertaken. The next chapter will detail the modifications that have been made to a low Reynolds number turbulence model in order to improve the predictions of transition while ensuring that it is numerically robust. The remainder of this thesis will be concerned with validating the new model against a variety of test cases that include transition under the influence of freestream turbulence intensity, pressure gradients, separation and unsteady impinging wakes.

Chapter 3
Development of the Transition Model

3.1 Introduction

As the capabilities of CFD improve, it is used increasingly in the aerodynamic design cycle to reduce the costs associated with experimental validation. Since many practical engineering flows experience transition from laminar to turbulent flow, the ability to predict with reasonable accuracy such transitional flows is becoming increasingly important. This chapter describes a novel approach to simulating laminar to turbulent transition.

As indicated in Chapter 1, a transition model should meet several requirements:

(i) It must be sensitive to the flow physics that affect transition.

(ii) It must be computationally inexpensive.

(iii) It should be fairly easy to incorporate into existing CFD codes and should be compatible with one or more widely accepted turbulence models.

(iv) Finally, the transition model must be compatible with unstructured grids.

The model developed here meets all of these requirements.

In principle, the model should be usable with any turbulence model that employs the turbulence kinetic energy equation. The transition model has been implemented here in terms of Menter's (1994) two-layer (SST) turbulence model. Menter's model, along with some other modifications made to it, is therefore described first. This is followed by a detailed description of the new transition model.

3.2 Menter's SST Turbulence Model

Menter's k-ω shear-stress transport (SST) model has become a popular turbulence model and it is now being used in a large number of academic and industrial CFD codes. This is primarily due to the fact that it is better at predicting strongly adverse pressure gradient boundary layers than the k-ε and k-ω models and because it corrects the harmful freestream ω sensitivity of Wilcox's (1988) k- ω model (Hellsten and Laine, 1998). The k-ω SST model combines several desirable characteristics from existing one and two-equation models, notably a zonal weighting of model coefficients and a limitation on the growth of the eddy viscosity in rapidly strained flows (Bardina et al, 1997).

The zonal weighting of the model coefficients uses Wilcox's k-ω model in the viscous sublayer and logarithmic region of the boundary layer and gradually switches to the standard k-ε model (in a k-ω formulation) in the wake region and in free-shear layers (Menter, 1994). In order to blend the k-ω and the k-ε model, the k-ε model is transformed into a k-ω formulation. Since $\varepsilon = 0.09\ k\ \omega$ (Wilcox, 1994) it is possible to transform the transport equation for ε into an ω formulation (see Menter, 1993). The difference between the k-ε model (in a k-ω formulation) and the original k-ω model is that an additional cross-diffusion term appears in the ω equation and that the modeling constants are different. The original k-ω model is then multiplied by a function F_1 and the transformed k-ε model by a function $(1- F_1)$ and the corresponding equations of each model are added together. The function F_1 is equal to 1.0 in the near wall region and tends to 0.0 away from the wall (Menter, 1994).

The SST model also modifies the definition of the turbulent eddy viscosity to improve the prediction of strongly adverse pressure gradient flows. Two-equation models generally over predict the skin friction and under predict the size of a separation bubble in adverse pressure gradients. The reason for this deficiency is that two-equation models do not correctly account for the important effects of transport of the turbulent shear stresses. The importance of accounting for shear stress transport effects was first demonstrated by the Johnson-King (JK) model (Johnson and King, 1985). The JK model

showed that significantly improved results could be obtained based on Bradshaw's assumption that the shear stress in a boundary layer is proportional to the turbulent kinetic energy (Bardina et al. 1997). This assumption is only valid for boundary layer flows and must be disabled outside of a boundary layer. The Bradshaw assumption was incorporated into the SST model (see Equation 3.1) along with the blending function F_2, which is equal to 1.0 in a boundary layer and 0.0 outside of a boundary layer where the Bradshaw assumption is not valid.

The CFD code that was used for all the computations in this thesis is the commercial program FLUENT (ver.5.7). This code has the ability to solve additional (i.e. along with the Navier-Stokes equations) user-defined scalar (UDS) transport equations. Menter's SST turbulence model was not available in the present version of FLUENT and it was therefore implemented through the use of two user-defined scalar transport equations (one for k and one for ω). The implementation of Menter's SST model into FLUENT will be discussed in section 3.3. The formulation of Menter's SST model will now be defined.

Eddy viscosity: $$\mu_t = \min\left[\frac{\rho k}{\omega};\frac{a_1 \rho k}{\Omega F_2}\right] \qquad a_1 = 0.31 \tag{3.1}$$

k-equation:

$$\frac{\partial}{\partial t}(\rho k)+\frac{\partial}{\partial x_j}(\rho u_j k) = P_k - \beta^* \rho \omega k + \frac{\partial}{\partial x_j}\left((\mu+\sigma_k \mu_t)\frac{\partial k}{\partial x_j}\right) \tag{3.2}$$

ω-equation:

$$\frac{\partial}{\partial t}(\rho \omega)+\frac{\partial}{\partial x_j}(\rho u_j \omega) = \frac{\alpha \rho P_k}{\mu_t} - \beta \rho \omega^2 + \frac{\partial}{\partial x_j}\left((\mu+\sigma_\omega \mu_t)\frac{\partial \omega}{\partial x_j}\right) + 2\rho(1-F_1)\sigma_{\omega 2}\frac{1}{\omega}\frac{\partial k}{\partial x_j}\frac{\partial \omega}{\partial x_j} \tag{3.3}$$

The set of constants Φ for the SST model are calculated from the constants Φ_1 and Φ_2 as follows:

$$\Phi = F_1\Phi_1 + (1-F_1)\,\Phi_2 \tag{3.4}$$

The constants of set 1 (Φ_1) are (k-ω):

$\sigma_{k1} = 0.85$, $\sigma_{\omega 1} = 0.5$, $\beta_1 = 0.0750$, $\beta^* = 0.09$, $\kappa = 0.41$

$$\alpha_1 = \beta_1 / \beta^* - \sigma_{\omega 1}\kappa^2 / \sqrt{\beta^*}$$

The constants of set 2 (Φ_2) are (standard k-ε):

$\sigma_{k2} = 1.0$, $\sigma_{\omega 2} = 0.856$, $\beta_2 = 0.0828$, $\beta^* = 0.09$, $\kappa = 0.41$

$$\alpha_2 = \beta_2 / \beta^* - \sigma_{\omega 2}\kappa^2 / \sqrt{\beta^*}$$

The production (P_k) of turbulent kinetic energy in Equation 3.2 is calculated from:

$$P_k = \tau_{ij}\frac{\partial u_i}{\partial x_j} \tag{3.5}$$

$$\tau_{ij} = 2\mu_t\left[S_{ij} - \frac{1}{3}\frac{\partial u_k}{\partial x_k}\delta_{ij}\right] - \frac{2}{3}\rho k\delta_{ij} \tag{3.5.1}$$

$$S_{ij} = \frac{1}{2}\left(\frac{\partial u_i}{\partial x_j} + \frac{\partial u_j}{\partial x_i}\right) \tag{3.5.2}$$

The blending function F_1 is defined as follows:

$$F_1 = \tanh\left(\arg_1{}^4\right) \quad \text{where } \arg_1 = \min\left\{\max\left[\frac{\sqrt{k}}{0.09\omega d};\frac{500\mu}{\rho d^2\omega}\right];\frac{4\rho\sigma_{\omega 2}k}{CD_{k\omega}d^2}\right\} \tag{3.6}$$

where d is the distance to the closest wall. $CD_{k\omega}$ is the positive portion of the cross-diffusion term and is given by:

$$CD_{k\omega} = \max\left[2\rho\sigma_{\omega 2}\frac{1}{\omega}\frac{\partial k}{\partial x_j}\frac{\partial \omega}{\partial x_j};10^{-20}\right] \tag{3.7}$$

The function F_2 is given by:

$$F_2 = \tanh\left(\arg_2{}^2\right) \text{ where } \arg_2 = \max\left[\frac{2\sqrt{k}}{0.09\omega d};\frac{500\mu}{\rho d^2\omega}\right] \tag{3.8}$$

Finally, the wall boundary condition for k and ω is:

$$k = 0 \qquad \omega = 10\frac{6\mu}{\rho 0.075 y^2} \tag{3.9}$$

where y is the distance of the first cell centre from the wall.

Table 3.1 summarizes the performance of the SST model for four fundamental free shear layers. The results for three other popular turbulence models are included as well. A variation in the spreading rate indicates a freestream dependency of a model on the choice of freestream ω (length scale).

It is clear from Table 3.1 that the SST model behaves essentially the same as the k-ε model for free shear layers. Results for the mixing layer and plane jet are in good agreement with experimental results. For the round jet, none of the models show very good agreement and this is a classical anomaly that is encountered when turbulence models have been fine-tuned with empirical data for mixing layers, plane jets, and/or far wake experiments (Bardina et al., 1997).

The far wake is an important free shear layer that will be encountered in this thesis. Proper wake evolution is important for computing the correct development of the impinging wake in the unsteady computations (see Chapter 6). From Table 3.1 it is clear that both the k-ε and SST models under predict the far wake spreading rate by approximately 30%. This will result in wakes that are thinner when compared to

experiment. The wake deficiency of this model must therefore be considered during any discussion of the unsteady computations in Chapter 6.

Round jet	Spreading rate
Experiment	0.086 – 0.095
Launder-Sharma k-ε	0.120
Wilcox k-ω	0.169 - 0.356
Menter SST	0.127
Spalart-Allmaras	0.253

Plane jet	Spreading rate
Experiment	0.100 – 0.110
Launder-Sharma k-ε	0.108
Wilcox k-ω	0.092 - 0.132
Menter SST	0.112
Spalart-Allmaras	0.143

Mixing layer	Spreading rate
Experiment	0.115 (±10%)
Launder-Sharma k-ε	0.099
Wilcox k-ω	0.068 - 0.143
Menter SST	0.100
Spalart-Allmaras	0.109

Far wake	Spreading rate
Experiment	0.365
Launder-Sharma k-ε	0.255
Wilcox k-ω	0.209 - 0.494
Menter SST	0.257 – 0.260
Spalart-Allmaras	0.339

Table 3.1 Comparison of non-dimensional spreading rate of four fundamental free shear layers (reproduced from Bardina et al. 1997).

An experiment was performed by Driver (1991) that is commonly used as a benchmark to test turbulence models for their ability to predict turbulent separation and reattachment. The experiment performed by Driver consists of an axial flow along the outer wall of a cylinder with a superimposed adverse pressure gradient (caused by an expansion in the wind tunnel section). Figure 3.1 shows the wall pressure distribution and the skin friction coefficient for Driver's flow as computed by the different turbulence models. It is clear that the SST model gives the best result and this is attributed to the fact that the transport of the principal turbulent shear stress is accounted for (Menter, 1994). The ability to accurately predict turbulent separation and reattachment is important for the design of turbine blades. This is one of the main reasons why the SST model was selected to form the basis of the transition model that was developed during the course of this thesis.

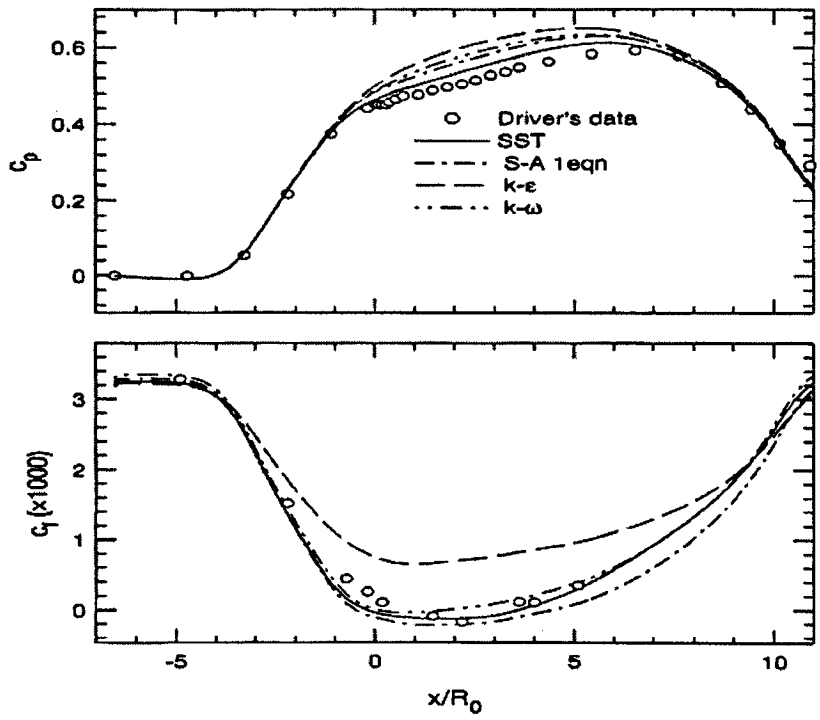

Figure 3.1 Comparison of surface pressure and skin friction coefficients for Driver's adverse pressure-gradient flow (reproduced from Bardina et al., 1997).

The final test case is the RAE 2822 transonic airfoil operating at a Mach number of 0.75 (Cooke et al, 1979). This test case is commonly used to benchmark the ability of turbulence models to predict shockwave/boundary layer interactions. While none of the test cases in this thesis are compressible, it is still desirable that the baseline turbulence model be proficient at predicting these types of flows because there are many cases in turbomachinery where shockwave/boundary layer interactions are important. The results of this test case are shown in Figure 3.2. Again, the SST model predicts results that are noticeably closer to the measurements than the other models, presumably due to its ability to model shear stress transport phenomena.

This concludes the discussion on the original SST model. The next section describes its implementation in the FLUENT commercial Navier-Stokes code.

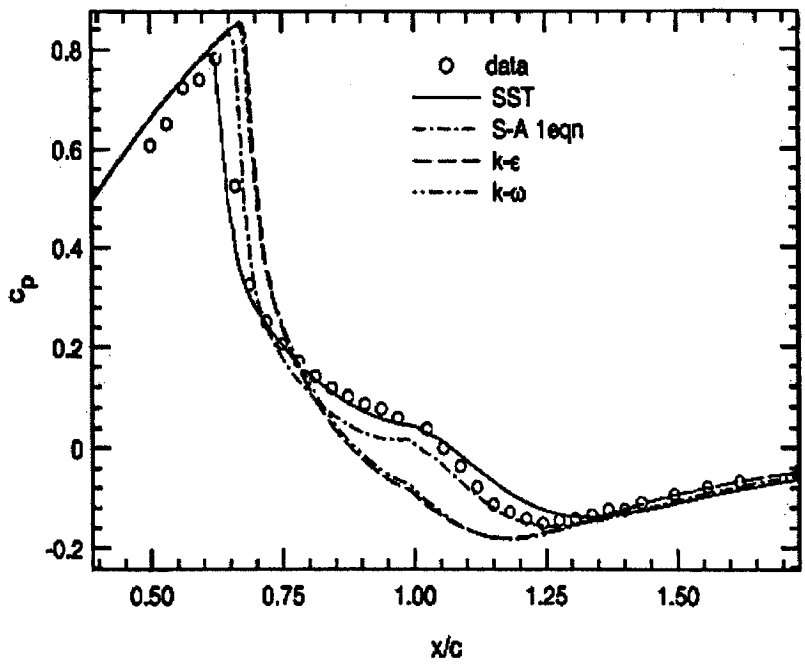

Figure 3.2 Comparison of surface pressure coefficients for the RAE 2822 transonic airfoil (reproduced from Bardina et al., 1997).

3.3 Solver Implementation

The commercial Navier-Stokes code FLUENT is a robust code that is widely used in academic and industrial applications. This code has been used for all the computations in this thesis. FLUENT is an unstructured, finite-volume based solver that is capable of very good parallel performance (Fluent, 1998). As well, the code has the capability of solving additional transport equations for arbitrary, user-defined scalars (UDS) in the same way that it solves the transport equation for a scalar such as the turbulent kinetic energy for a turbulence model.

For an arbitrary scalar Φ_n, FLUENT solves the following transport equation (Fluent, 1998):

$$\frac{\partial}{\partial x_i}\left(\rho u_i \Phi_n - \Gamma_n \frac{\partial \Phi_n}{\partial x_i}\right) = S_{\Phi_n} \qquad \text{n=0,...,N} \tag{3.10}$$

The variable n is the number of scalar transport equations. The diffusion coefficient Γ_n, and the source term $S_{\Phi n}$, as well as the boundary conditions, are supplied by the user This is accomplished using subroutines (User-Defined Functions, UDF) written in C that are compiled and linked to the main solver code upon runtime. These subroutines have full access to all the main solver variables (eg. velocity gradients, eddy viscosity, etc.). The first term in the bracket of Equation 3.10 is the convective flux term. This is computed internally by FLUENT based on the mass flow rate and does not need to be specified by the user.

Since Menter's SST turbulence model was not available in the present version of FLUENT, it has been implemented using the user-defined scalar functionality. It was found that the user-defined functions could not access and modify the solver variable for the turbulent eddy viscosity μ_t, unless one of FLUENT's own turbulence models was active. This problem was fixed by enabling an algebraic mixing length model that is present but rarely used in FLUENT. The additional computational overhead required by the mixing length model was negligible. Figure 3.3 illustrates the sequential order in which all the equations are solved. As shown, after μ_t is computed from the mixing-length model it is then recomputed (by the UDF for the source term of Φ_0) using the local cell values of k and ω. Upon the next iteration, the μ_t that is used to solve the Navier-Stokes equation is therefore that of the two-equation model, not the algebraic model. This has been verified by a flat plate simulation which confirmed that μ_t was computed properly from the two-equation turbulence model.

There are three primary solver formulations available in FLUENT: segregated, coupled implicit and coupled explicit. The segregated and coupled formulations differ in the way that the continuity, momentum and (where appropriate) energy equations are solved. The segregated solver solves these equations sequentially (i.e. one after another), while the coupled solver solves them simultaneously (Fluent, 1998). The segregated

solver was used in the present work. For all the solver formulations, extra equations such as those for turbulence and user-defined scalars are solved sequentially after the Navier-Stokes equations. For the segregated solver in incompressible flows, the coupling between the momentum and continuity equations is achieved through the use of the pressure-velocity coupling family of algorithms (i.e. SIMPLE, SIMPLEC, PISO) (Versteeg and Malalasekera, 1995).

From Fluent (1998), the segregated solver along with the PISO algorithm is the recommended solver formulation for incompressible unsteady flows. This is because the PISO pressure-velocity coupling scheme is based on a more accurate approximation of the relationship between the corrections for pressure and velocity (Fluent, 1998). As a result, fewer solver iterations are required to obtain convergence in between unsteady time steps. The PISO algorithm has also been adapted for use in steady flows. According to Versteeg and Malalasekera (1995) when coupling between the momentum equations and a scalar variable (eg. a turbulence model) is present, there is no clear advantage between PISO and the other members of the different pressure-velocity correction family of algorithms. Since it is not evident whether or not there is a clear advantage to any of the other pressure-velocity algorithms, the PISO algorithm was used for all the steady and unsteady computations in this thesis.

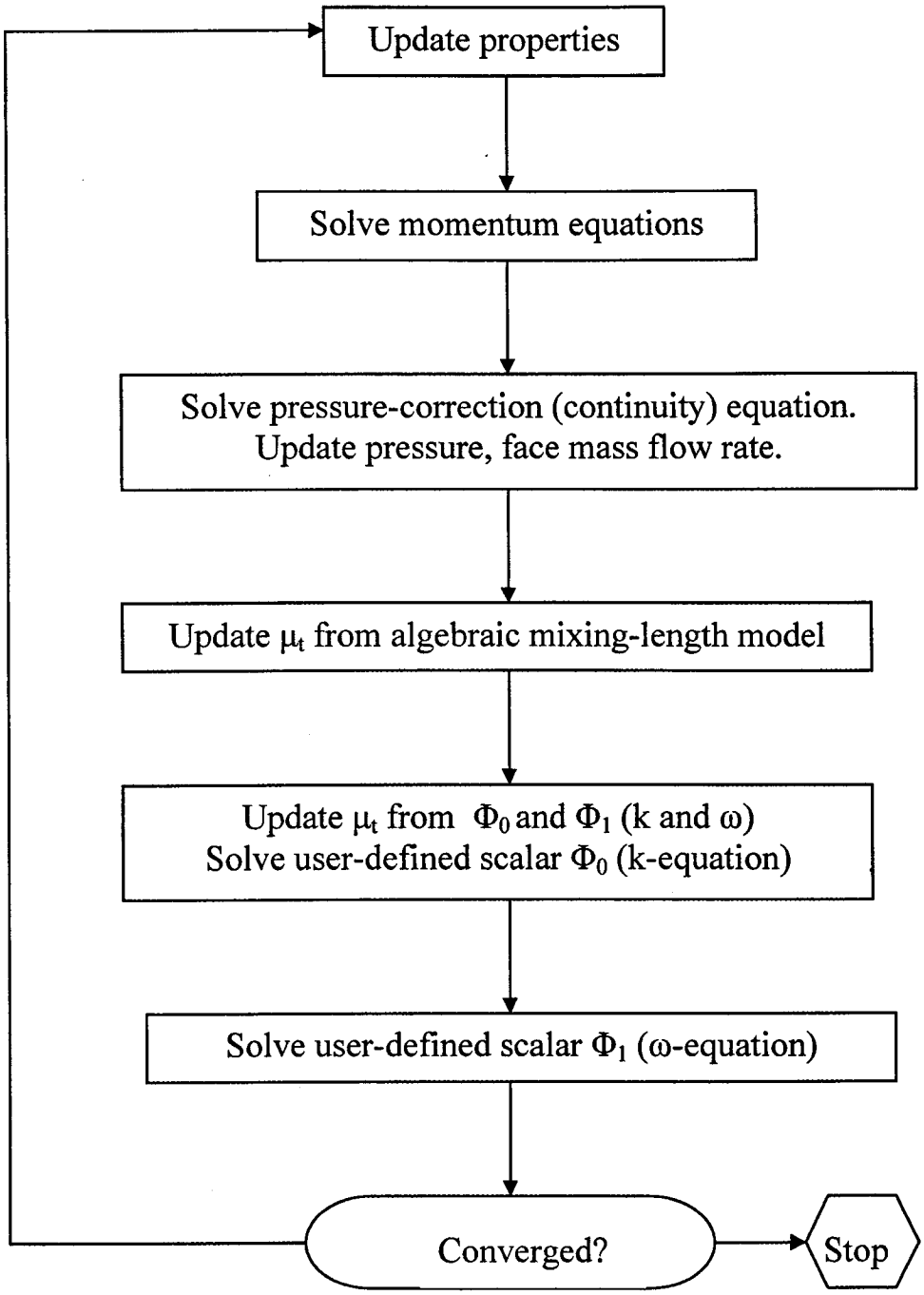

Figure 3.3 Overview of the FLUENT solution method for one solver iteration.

The PISO algorithm requires the specification of under-relaxation factors for the continuity, momentum and turbulence/UDS equations. Under-relaxation factors of 0.3 for continuity and momentum and 0.6 for turbulence/UDS equations where found to give reasonably good convergence rates.

FLUENT is capable of handling quadrilateral, triangular and mixed (hybrid) meshes. For this thesis, quadrilateral meshes were used exclusively because the cells can be aligned along the main flow direction thus reducing the numerical (false) diffusion error (Versteeg and Malalasekera, 1995). Second-order upwinding is used to compute all flux terms while second-order central differencing is used to compute all diffusive terms. All the computations in this thesis where run in parallel using a six CPU (P III 800 MHz) Linux cluster.

The classical flat plate boundary layer flow has been solved for both laminar and turbulent flow. This was done to validate the mesh that will be used to calibrate the transition model and to ensure that the Menter SST turbulence model has been properly implemented into FLUENT. The mesh is shown in Figure 3.4 and consists of 370x70 cells. The plate geometry consists of a 10 m long surface with a small elliptical leading edge whose semi-axis was 0.75 mm in the y direction and 1.5 mm in the x direction. An elliptical leading edge was used to prevent the presence of a laminar separation bubble at the plate leading edge. The distance between the first cell center and the wall was specified such that a y^+ of 1.0 or less was present at all times. The freestream flow conditions were such that the Reynolds number from the leading edge to the end of the plate was $6x10^6$.

The results of the flat plate computations for laminar flow and for the Menter SST turbulence model are shown in Figure 3.5. The skin friction (C_f) for the laminar flow computation is in excellent agreement with the exact Blasius solution (from White, 1991). For the turbulent computation, the error between the Menter SST model and the Prandtl $1/5^{th}$ law (from White, 1991) decreases as the Reynolds number increases.

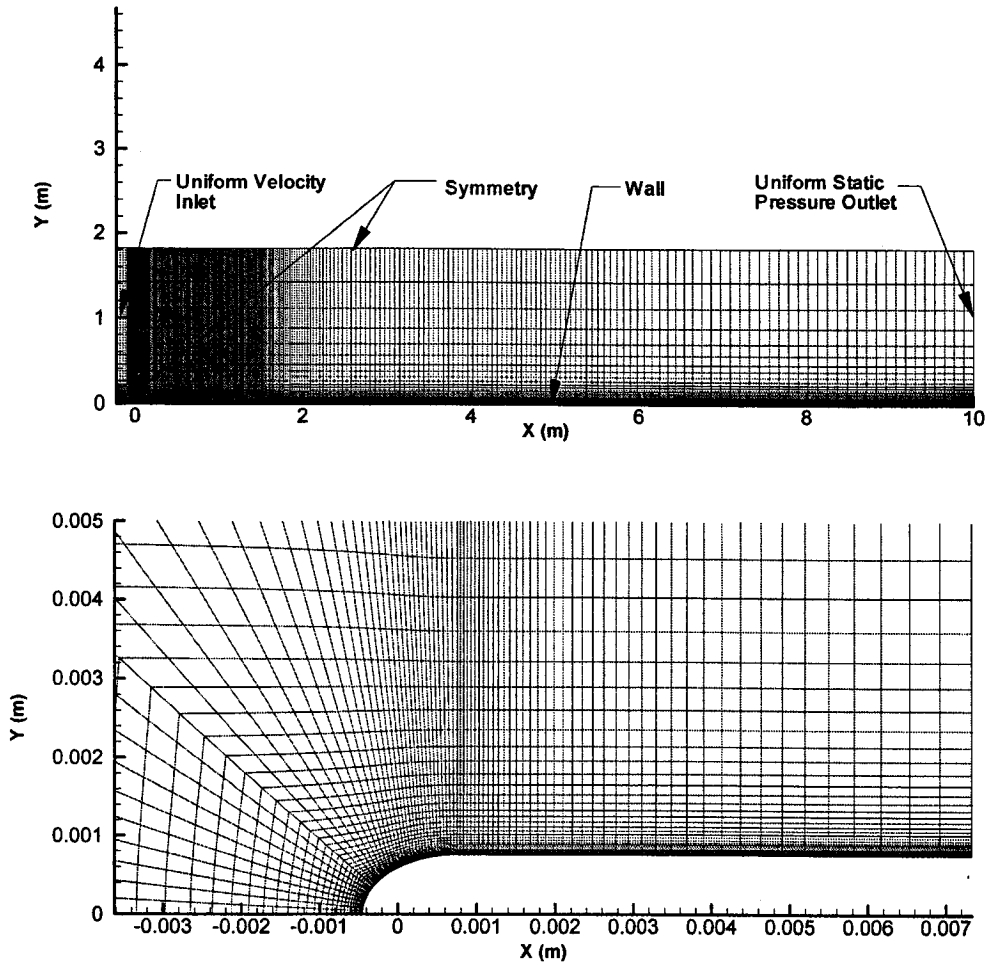

Figure 3.4 Flat plate mesh used to calibrate the new transition model and validate the Menter SST turbulence model implementation into FLUENT.

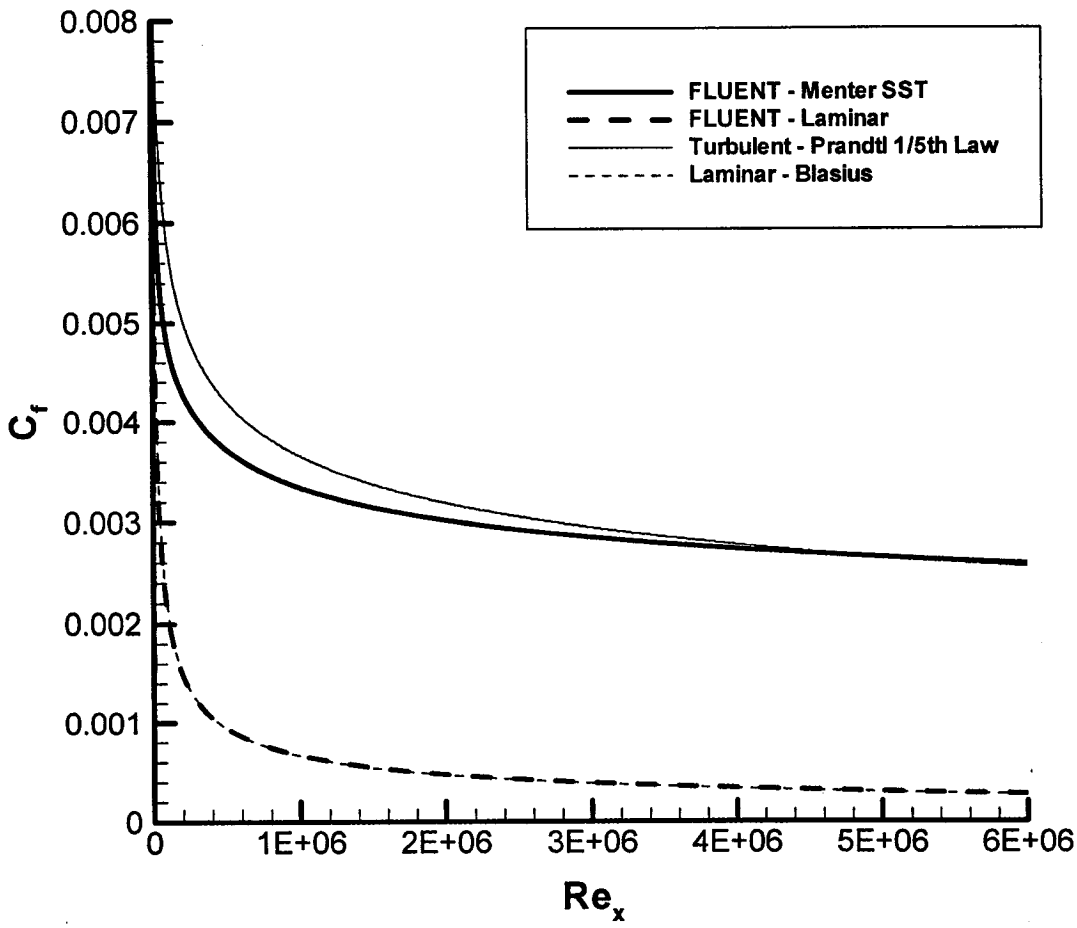

Figure 3.5 Numerical and analytical skin friction for zero pressure gradient flat plate flow.

This concludes the discussion on the FLUENT CFD code and the implementation of the Menter SST turbulence model into this code. The next section will discuss the concept of vorticity Reynolds number and how it can be used to control the transition process.

3.4 Vorticity Reynolds Number

The new transition model is based on Van Driest and Blumer's (1963) concept of vorticity Reynolds number. Van Driest and Blumer argued that disturbances in a laminar boundary layer are amplified in regions that have high vorticity (shear) but are well away from the region of wall damping. The combined influence of shear and distance from the wall was embodied in the vorticity Reynolds number (Re_v) where:

$$Re_v = \frac{\rho y^2}{\mu}\frac{\partial u}{\partial y} = \frac{\rho y^2}{\mu}\Omega \tag{3.11}$$

and y is the distance from the nearest wall and Ω is the vorticity.

The present author found from more recent data that the location within a laminar boundary layer at which the vorticity Reynolds number was a maximum corresponded surprisingly well with the experimental location of the most rapid growth of the laminar fluctuations. This is illustrated in Figures 3.6 and 3.7 which show the results for the T3A and T3C4 flat plate test cases, two of the ERCOFTAC T3-series of transitional flow experiments (Savill, 1993a,b). The velocity derivative used to calculate the local vorticity Reynolds was obtained by a second-order central difference of the experimental velocities. Both the T3A and T3C4 test cases have freestream turbulence levels of approximately 3.0 percent. The T3A test case is a zero pressure gradient flow while the T3C4 test case consists of a favorable pressure gradient followed by an adverse pressure gradient that is strong enough to cause a separation bubble before transition.

The T3C4 test case is a particularly interesting flow field because the freestream pressure variation is representative of that on the suction surface of a turbine blade. From the leading edge until a Re_x of 6.67×10^4 the flow is accelerated and as a result, the local vorticity Reynolds number and the growth of the laminar fluctuations remains small. Beyond this point, the adverse pressure gradient begins and the peak vorticity Reynolds number along with the growth of the laminar fluctuations starts to increase. At a Re_x of

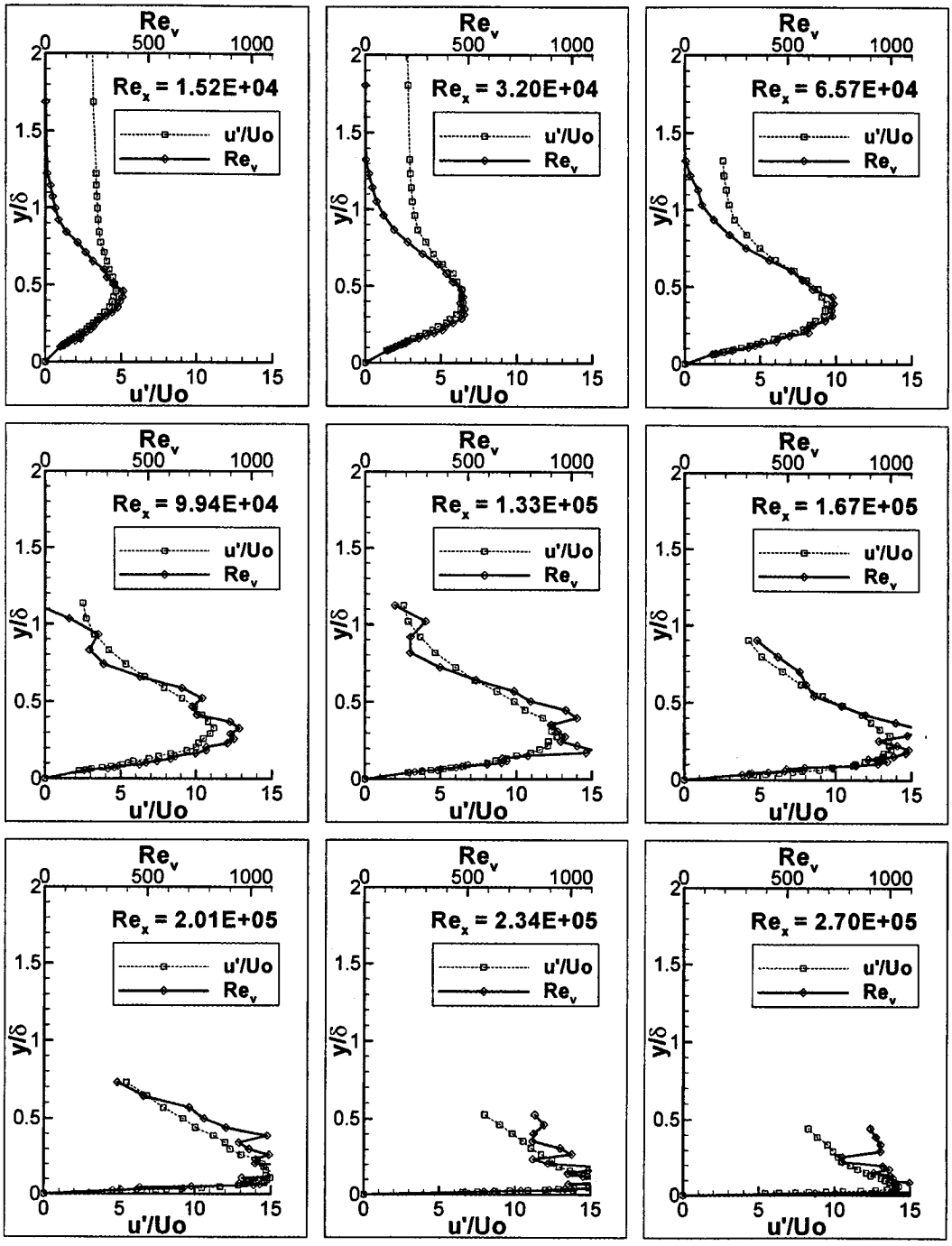

Figure 3.6 Fluctuations (u'/Uo, %) in a boundary layer as compared to the vorticity Reynolds number (Re_V) for the T3A zero pressure gradient test case.

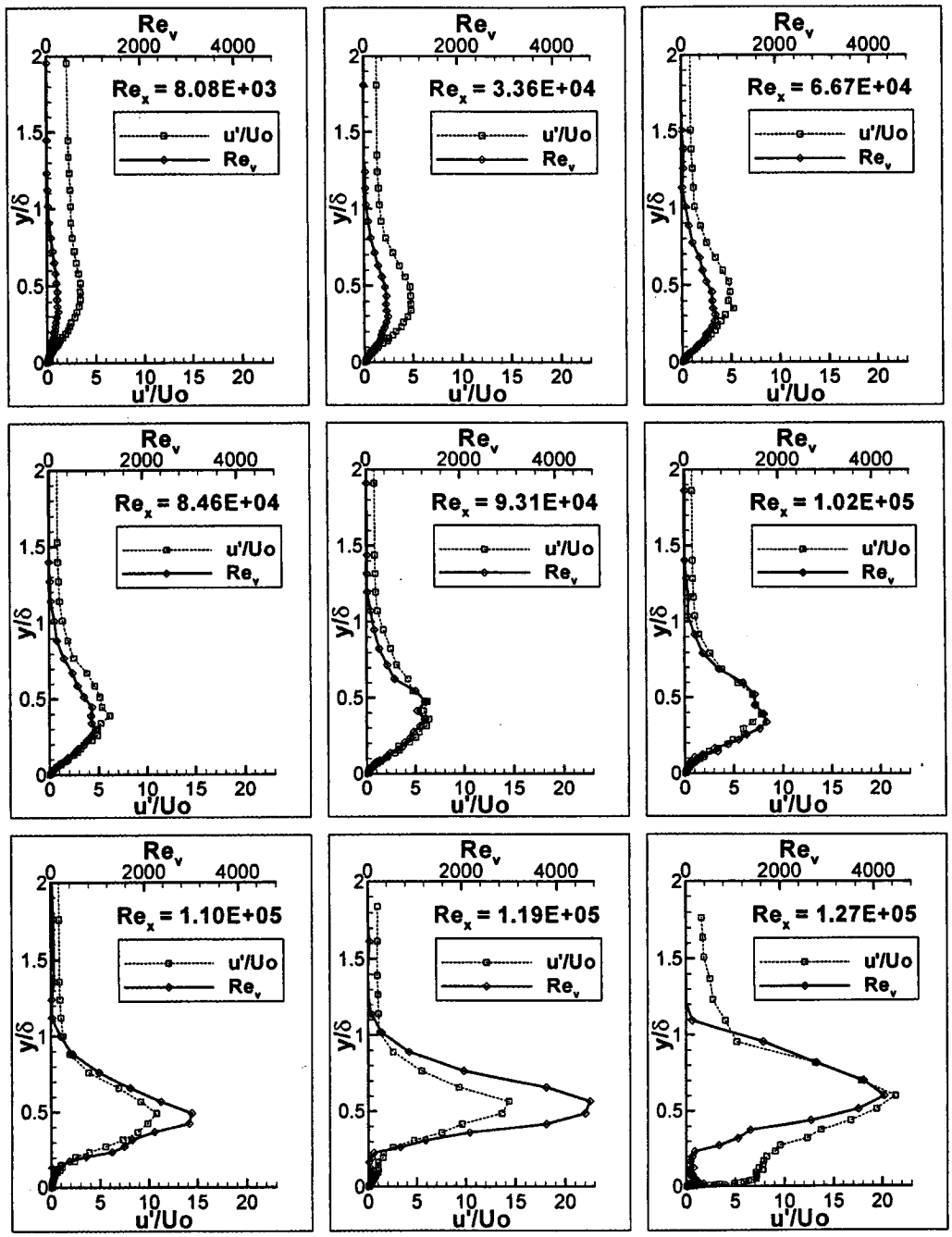

Figure 3.7 Fluctuations (u'/Uo, %) in a boundary layer as compared to the vorticity Reynolds number (Re_v) for the T3C4 Favorable-Adverse pressure gradient test case.

$1.1x10^5$ the boundary layer separates and there is a significant increase in the vorticity Reynolds number and the growth of the laminar fluctuations. The location in the boundary layer where the fluctuations and the peak vorticity Reynolds number are a maximum is in excellent agreement throughout the boundary layer development.

From Figures 3.6 and 3.7 it would appear that the local vorticity Reynolds number is an excellent indicator of local receptivity to disturbances of the laminar boundary layer. The present transition model began with the premise that the production of turbulence kinetic energy in the laminar boundary layer would therefore be influenced by the local value of the vorticity Reynolds number. This is an important idea because the vorticity Reynolds number is a local quantity (i.e. can be computed on a cell by cell basis) and hence a transition model based on it will not require the integration of boundary layer quantities to predict the onset of transition. The detailed development of the present transition model will now be discussed.

3.5 Transition Model Development

There are two ways that transitional flows are usually modeled in CFD codes. The first is to calculate the laminar solution and integrate the boundary layer quantities to obtain the momentum thickness Reynolds number (Re_θ) at different stream-wise locations. The momentum thickness Reynolds number is then used to apply an empirical onset correlation. Once the starting location of transition has been determined a turbulence model with the eddy viscosity disabled in the laminar regions is used to calculate the final solution. While fairly accurate, this method is hard to implement in unstructured codes because it is very difficult to determine a proper integration strategy for the boundary layer quantities.

The second means of simulating transitional flows is to use a two-equation low-Reynolds number turbulence model. For unstructured codes this method is favored over the empirical correlation approach. Unfortunately, these models suffer from the fact that

they often predict the onset of transition far too early and do not have the proper sensitivity to strong pressure gradients and separation induced transition (Suzen et al, 2001). The development of the present transition model is therefore concerned with controlling the production of k as a function of the local vorticity Reynolds number so that the onset of transition is correctly predicted by a low-Reynolds number turbulence model. This approach is similar to the work of Schmidt and Patankar (1991) who argued that the production term for k (P_k, see Equation 3.15) in the turbulent-kinetic-energy equation is the logical place for stability-related information to be applied.

The model is extremely simple to incorporate into an existing CFD code because it consists solely of an algebraic function of Re_v that multiplies the production term for k. In keeping with the convention established by Schmidt and Patankar this algebraic function will be referred to by the acronym "PTM" (for Production Term Modification). The PTM term has been calibrated empirically for use with the Menter (1994) SST turbulence model.

3.5.1 Modifications to SST

The SST model was originally developed for fully turbulent flows. As a result, there are a few modifications that must be made so that it will be compatible with the presence of a laminar boundary layer in the flow.

The SST model is essentially a hybrid model that uses a k-ω model in the boundary layer and a k-ε (transformed into k-ω formulation) model in the freestream. Wilcox (1994) has developed low-Reynolds number damping functions for the k-ω model that allow the transitional region to be predicted reasonably well. These damping functions are based on the viscosity ratio (R_T) where:

$$R_T = \frac{\mu_t}{\mu} = \frac{\rho k}{\omega \mu} \tag{3.12}$$

A turbulent viscosity ratio less than 1.0 ($R_T << 1$) represents essentially laminar flow. When the viscosity ratio is approximately equal to 1.0 ($R_T \approx 1$) the onset of transition occurs and the Wilcox damping functions cause the growth of k to increase significantly. As k increases, the eddy viscosity and the skin friction start to rise. Once the viscosity ratio becomes large ($R_T >> 1$), the growth of ω starts to increase until a balance between the production and dissipation of k is achieved. Once this balance occurs transition from laminar to turbulent flow is said to be complete. Consistent with experimental measurements the entire process is very sensitive to the Reynolds number at which transition commences. The larger the transition onset Reynolds number, the longer the transition length. The transition length ($Re_{\Delta xt}$) as predicted by the low-Reynolds number Wilcox model is shown in Figure 3.8. There is a large scatter in the experimental data. However, the Wilcox model appears to give reasonable agreement with the average of the experimental values.

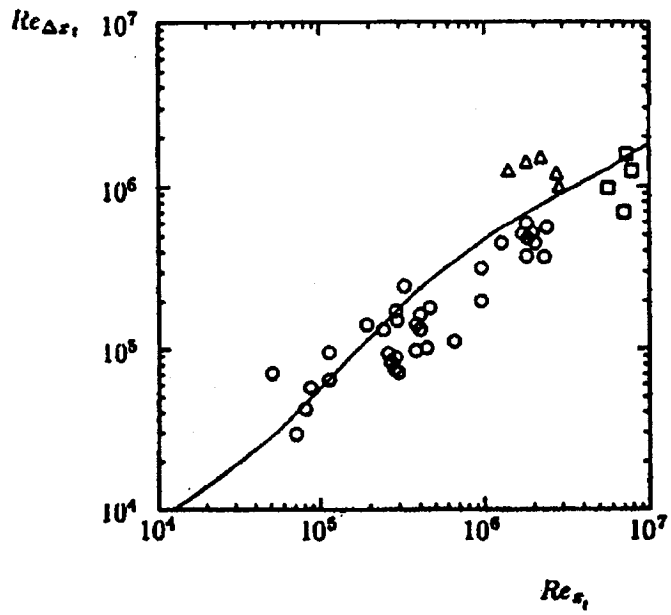

o, Dhawan-Narasimha; Δ, Schubauer-Skramstad; □, Fisher-Dougherty; ——, computed.

Figure 3.8 Transition length ($Re_{\Delta xt}$) vs. transition onset location (Re_{xt}) as computed by the low-Reynolds number Wilcox turbulence model (reproduced from Wilcox, 1994).

The Wilcox low-Reynolds number damping functions were also designed to reproduce the proper profiles of k in turbulent boundary layers as obtained from DNS computations. Wilcox's results were in very good agreement with the DNS computations. An example is shown in Figure 3.9. Of particular note is that the model predicts the peak value of k near the wall to within 4% of the DNS value (Wilcox, 1994).

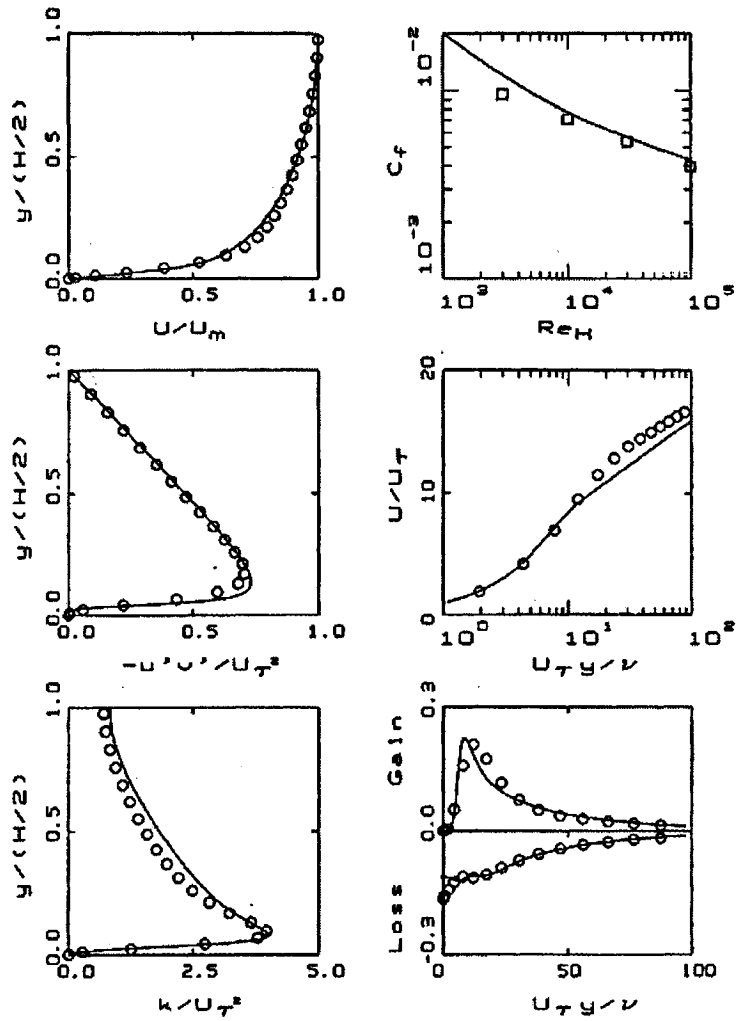

Figure 3.9 Low-Reynolds number turbulent boundary layer characteristics as computed by the Wilcox damping functions and Direct Numerical Simulation (DNS), (reproduced from Wilcox, 1994).

Wilcox's low-Reynolds number model has been incorporated into the SST model (Equations 4 and 8) so that once the onset of transition occurs the transitional region will be correctly predicted. In practice, Wilcox's (1994) low-Reynolds number model predicts the onset of transition far too early and does not have the proper sensitivity to separation induced transition (Zheng et al, 1998). The vorticity Reynolds number will therefore be used to control the growth of k and ω until the onset of transition occurs. Once transition commences (i.e. $R_T > 1.0$) the present transition model will be disabled and the growth of k and ω through the transitional region and beyond will be controlled by the modified SST model.

It is now common knowledge that most turbulence models give overly high levels of turbulent kinetic energy in stagnation point regions. This is because the Boussinesq assumption fails in flows with large normal strain and this results in excessive production of k in stagnation flows (Gehrer et al, 2000). These unphysical levels of k are convected downstream and make the prediction of transition based on the freestream turbulence intensity difficult. Most researchers who are developing transition models based on modifications to a turbulence model avoid this problem by specifying profiles of velocity and turbulence quantities as boundary conditions somewhere downstream of a stagnation point. The low-Reynolds number turbulence model developed by Biswas and Fukuyama (1994) is a good example of this practice. However, to be useful in practical applications (which almost always involve stagnation points) the unphysical production of k in a stagnation region must be eliminated.

The most common way to correct the stagnation point problem of a turbulence model is to invoke a realizability constraint on the production term. The production term is often approximated as being equal to $\mu_t S^2$ where S is the modulus of the mean rate-of-strain tensor $S = \sqrt{2S_{ij}S_{ij}}$ (Garg and Ameri, 2001). Since turbulence models that use production terms based on vorticity (Ω) do not exhibit the stagnation point problem some researchers have attempted to incorporate the vorticity magnitude into the production term for k (Menter, 1992; Kato and Launder, 1993). This is often accomplished by defining the production term as either $\mu_t S\Omega$ or $\mu_t \Omega^2$. These ideas follow from the fact that

for a stagnation flow, $\Omega = 0$ and for a simple shear flow, use of $S\Omega$ is identical to S^2 (Garg and Ameri, 2001).

Garg and Ameri (2001) conducted a study to determine the effect of the different production term formulations on the computed heat transfer on a transonic turbine blade using the Menter SST turbulence model. They concluded that production based on S^2 resulted in excessively high heat transfer rates while production based on $S\Omega$ was marginally better than Ω^2. It should be noted that Garg and Ameri where examining fully turbulent flows and that the present transition model will be far more sensitive to excessive production of k in stagnation flows.

The present author has conducted a similar study using the transition model developed in this thesis. The results where compared to the experimental ERCOFTAC T3A test case. This test case consists of a flat plate with a circular leading edge and a freestream turbulence intensity of 3.0% (for further information see chapter 4). It was determined that even when the production term was based on $S\Omega$ the generation of k in the stagnation region was excessive and would cause transition far too early. As well, there is some evidence that suggests that Ω^2 based production over-predicts the eddy viscosity at the center of a vortex (Fluent, 1998). The solution that was used with the present transition model was to define the production term as a minimum of either strain or vorticity based production (see Equation 3.26).

Based on the new production term formulation, in stagnation regions the vorticity based production will be active and in certain cases where the vorticity exceeds the strain rate the original SST model will be recovered. The results for the T3A test case are shown in Figures 3.8 and 3.9. Clearly, the new production term formulation results in a significant improvement over the original strain based version.

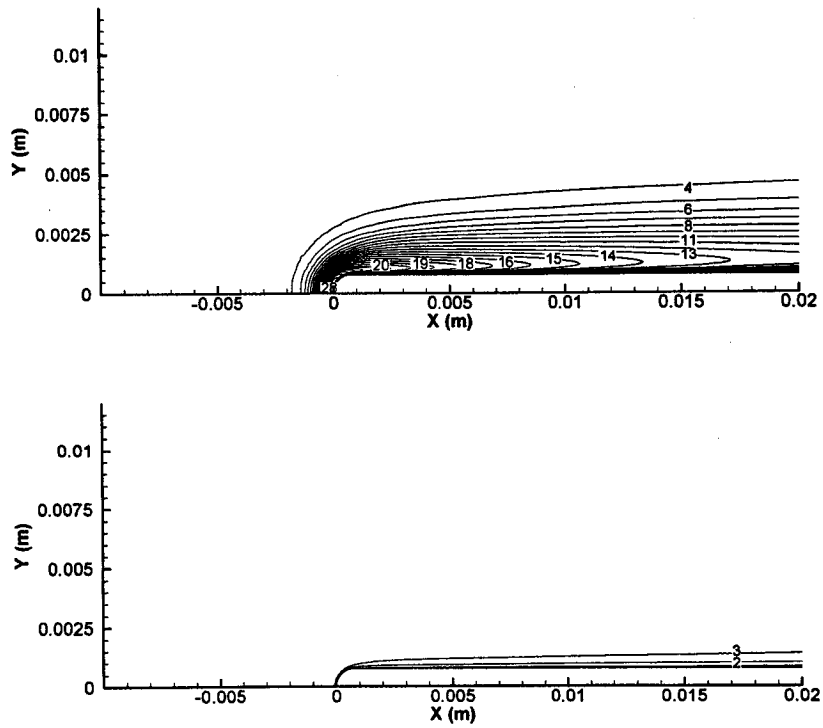

Figure 3.8 Computed contours of turbulence intensity (Tu) in percent for strain rate based production (top) and the formulation used with the present transition model (bottom).

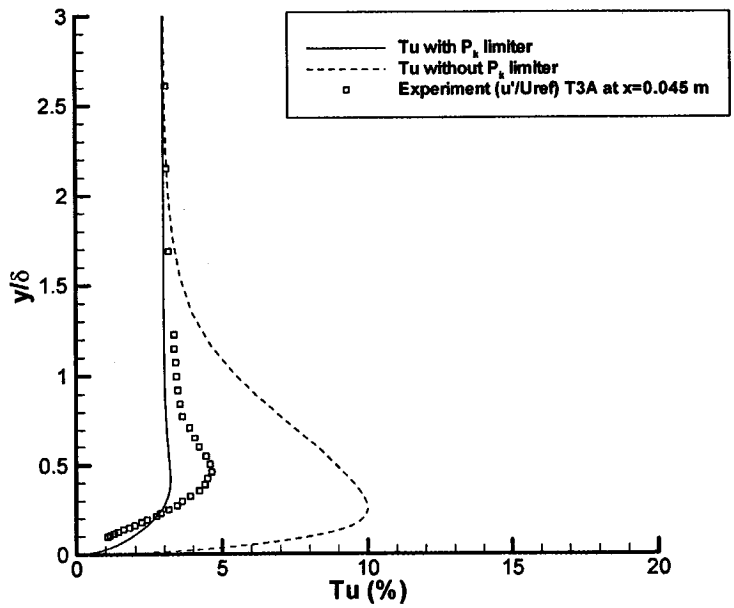

Figure 3.9 Experimental and computed boundary layer profiles of turbulence intensity (%) for strain rate based production and the formulation used with the present transition model.

The final modification to the SST model is to correct a deficiency in the blending function (F_1) responsible for switching between the k-ω and k-ε models. It was found that in the center of the laminar boundary layer F_1 could potentially switch from 1.0 (k-ω) to 0.0 (k-ε). This is not desirable because the k-ω model must be active in the laminar and transitional boundary layers. The deficiency in the blending function is not at all surprising as the equations used to define F_1 where intended solely for turbulent boundary layers.

The solution is to redefine the function F_1 in terms of a blending function that will always be equal to 1.0 in a laminar boundary layer. Based on some of the ideas discussed in Biswas and Fukuyama (1994) it was decided to base this function on the wall-distance based turbulent Reynolds number (R_y) which is defined as follows:

$$R_y = \frac{\rho y \sqrt{k}}{\mu} \tag{3.13}$$

The modified blending function is detailed in Equation 3.30. It correctly ensures that the k-ω model is active in the laminar boundary layer and does not have any adverse effects in the turbulent region.

The modified SST model is defined as follows:

$$\mu_t = \min\left[\alpha^* \frac{\rho k}{\omega}; \frac{a_1 \rho k}{\Omega F_2}\right] \qquad a_1 = 0.31 \tag{3.14}$$

$$\frac{D\rho k}{Dt} = P_k PTM - \beta^* \rho \omega k + \frac{\partial}{\partial x_j}\left((\mu + \sigma_k \mu_t)\frac{\partial k}{\partial x_j}\right) \tag{3.15}$$

$$\frac{D\rho\omega}{Dt} = \frac{\alpha \rho P_k}{\mu_t} - \beta \rho \omega^2 + \frac{\partial}{\partial x_j}\left((\mu + \sigma_\omega \mu_t)\frac{\partial \omega}{\partial x_j}\right) + 2\rho(1 - F_1)\sigma_{\omega 2}\frac{1}{\omega}\frac{\partial k}{\partial x_j}\frac{\partial \omega}{\partial x_j} \tag{3.16}$$

The function F_2 is given by:

$$F_2 = \tanh\left(\arg_2^{\,2}\right) \tag{3.17}$$

$$\arg_2 = \max\left[\frac{2\sqrt{k}}{0.09\,\omega d};\frac{500\,\mu}{\rho d^2 \omega}\right] \tag{3.18}$$

The wall boundary condition for k and ω is:

$$k = 0 \tag{3.19}$$

$$\omega = 10\frac{6\mu}{\rho 0.075(y)^2} \tag{3.20}$$

where y is the distance of the first cell centre from the wall.

The set of constants Φ for the SST model are calculated from the constants Φ_1 and Φ_2 as follows:

$$\Phi = F_1\Phi_1 + (1\text{-}F_1)\,\Phi_2 \tag{3.21}$$

The constants of set 1 (Φ_1) are (low-Re k-ω):

$$\sigma_{k1} = 0.85 \qquad \sigma_{\omega 1} = 0.5 \qquad \beta_1 = 0.0750$$

$$\alpha_o^* = \beta_1/3 \qquad \alpha_o = 1/10$$

$$\alpha_1^* = \frac{\alpha_o^* + R_T/R_k}{1 + R_T/R_k} \tag{3.22}$$

$$\alpha_1 = \frac{5}{9}\cdot\frac{\alpha_o + R_T/R_\omega}{1 + R_T/R_\omega}$$

$$\beta_1^* = 0.09\cdot\frac{5/18 + (R_T/R_\beta)^4}{1 + (R_T/R_\beta)^4}$$

$$R_k = 6 \qquad R_\omega = 2.7 \qquad R_\beta = 8$$

The constants of set 2 (Φ_2) are (standard k-ε):

$$\sigma_{k2} = 1.0 \qquad \sigma_{\omega 2} = 0.856 \qquad \beta_2 = 0.0828 \qquad \kappa = 0.41 \tag{3.23}$$

$$\beta_2^* = 0.09 \qquad \alpha_2^* = 1 \qquad \alpha_2 = \beta_2 / \beta_2^* - \sigma_{\omega 2}\kappa^2 / \sqrt{\beta_2^*}$$

The production term for k (P_k) in Equation 5 and 6 is calculated from:

$$P_{korig} = \tau_{ij} \frac{\partial u_i}{\partial x_j} \tag{3.24}$$

$$\tau_{ij} = 2\mu_t \left[S_{ij} - \frac{1}{3} \frac{\partial u_k}{\partial x_k} \delta_{ij} \right] - \frac{2}{3} \rho k \delta_{ij} \tag{3.25}$$

$$P_k = \min\left(P_{korig}; \mu_t \Omega^2\right) \tag{3.26}$$

where P_{korig} is the original strain based production term from the SST model.

The new blending function F_1 is defined as:

$$F_{1orig} = \tanh\left(\arg_1^4\right) \tag{3.27}$$

$$\arg_1 = \min\left\{ \max\left[\frac{\sqrt{k}}{0.09\omega d}; \frac{500\mu}{\rho d^2 \omega} \right]; \frac{4\rho\sigma_{\omega 2} k}{CD_{k\omega} d^2} \right\} \tag{3.28}$$

$$F_4 = \exp\left[-\left(\frac{R_y}{120} \right)^8 \right] \tag{3.29}$$

$$F_1 = \max\left(F_{1orig}; F_4\right) \tag{3.30}$$

where F_{1orig} is the original F_1 switching function from the SST model.

3.5.2 The New Transition Model

The classical flat plate boundary layer flow has been used to calibrate the new transition model. The mesh used to calibrate the model was discussed in Section 3.3. As was stated earlier, an elliptical leading edge was used to prevent the presence of a laminar separation bubble at the plate leading edge. The importance of calibrating the model with a leading edge stagnation point cannot be overstated. A major source of error in the calibration of low-Reynolds number turbulence models in the past has been due to the direct specification of starting profiles of k and length scale. The mesh used to calibrate the model was a C-mesh that consisted of 370x70 cells. A large mesh was necessary in order to obtain a grid independent solution for the transitional region at onset Reynolds numbers that varied from 50 000 to 4.0E+6. The recommended procedure for using the new transition model is to solve the flow field as a laminar solution first and then to start the transitional computation by initializing k and ω using the inlet values.

The PTM term that is used to control the production of k in a laminar boundary layer takes the following form:

$$PTM = 1 - (PTM_1 + PTM_2)F_3 \tag{3.31}$$

The PTM term can vary from 0.0 to 1.0 where 1.0 would result in the fully turbulent production term.

The F_3 term is a switching function that disables the model outside of laminar boundary layers and allows a smooth blending between the laminar region (governed by the new transition model) and the transitional region (governed by the Wilcox low-Reynolds number damping functions). The most obvious choice of a dependant variable is the viscosity ratio (R_T).

Based on the work of Biswas and Fukuyama (1994) and numerical experimentation F_3 is defined as follows:

$$F_3 = \exp\left[-\left(\frac{R_T}{6.5}\right)^4\right] \tag{3.32}$$

F_3 is equal to 1.0 in a laminar boundary layer and gradually switches to 0.0 as transition commences and the viscosity ratio starts to increase.

The PTM_1 term is used to calibrate the model so that it properly reproduces the effect of freestream turbulence intensity on the transition onset location for zero pressure gradient flow. To perform the calibration, the freestream turbulence intensity was varied from 6.0 percent to 0.1 percent over the flat plate and the corresponding transition onset location predicted by the turbulence model was recorded. For the purpose of calibrating the model the transition onset location was defined as the point of minimum skin friction. The freestream dissipation length scale (i.e. ω) was specified so that the decay rate of k was minimal. As a result, a constant freestream turbulence level was present over the entire laminar boundary layer.

The first assumption that must be made to calibrate the model is that for a vorticity Reynolds number of 0.0 the PTM_1 term must be equal to 0.0 (i.e. no growth of k). It is now possible to map out the value of the PTM_1 term (as a function of the local vorticity Reynolds number) that results in the correct onset location of transition based on the freestream turbulence intensity. This was accomplished by curve fitting a polynomial to a set of control points (see Figure 3.10, K = 0.0). The x axis of the control points is the peak vorticity Reynolds number that corresponds to a desired transition onset location. The y axis is the corresponding value of the PTM term that will be computed by the polynomial. The label below each control point in Figure 3.10 is the corresponding freestream turbulence intensity. The y value of each control point was varied iteratively until the transition onset location was in agreement with the empirical data shown in Figures 3.11 and 3.12.

The curve in Figure 3.10 for K=0.0 is described by two polynomials as follows:

$$PTM_1 = \begin{cases} 1-\left[\begin{matrix}(3.82E-04)\mathrm{Re}_v+(-3.94E-07)\mathrm{Re}_v^2 \\ +(1.43E-10)\mathrm{Re}_v^3\end{matrix}\right], \mathrm{Re}_v < 1000 \\ 1-[0.12+(1.0E-05)\mathrm{Re}_v], \mathrm{Re}_v \geq 1000 \end{cases} \tag{3.32}$$

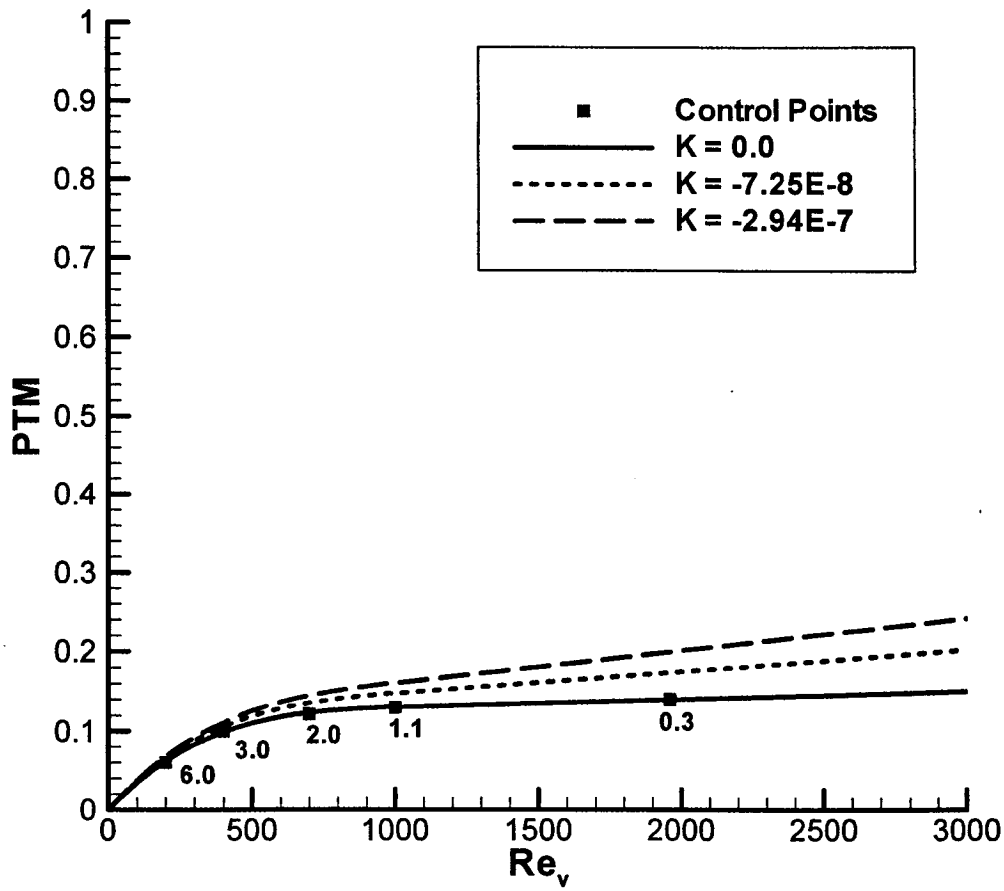

Figure 3.10 Calibration of the PTM term to reproduce the effect of turbulence intensity and pressure gradient on the transition onset location.

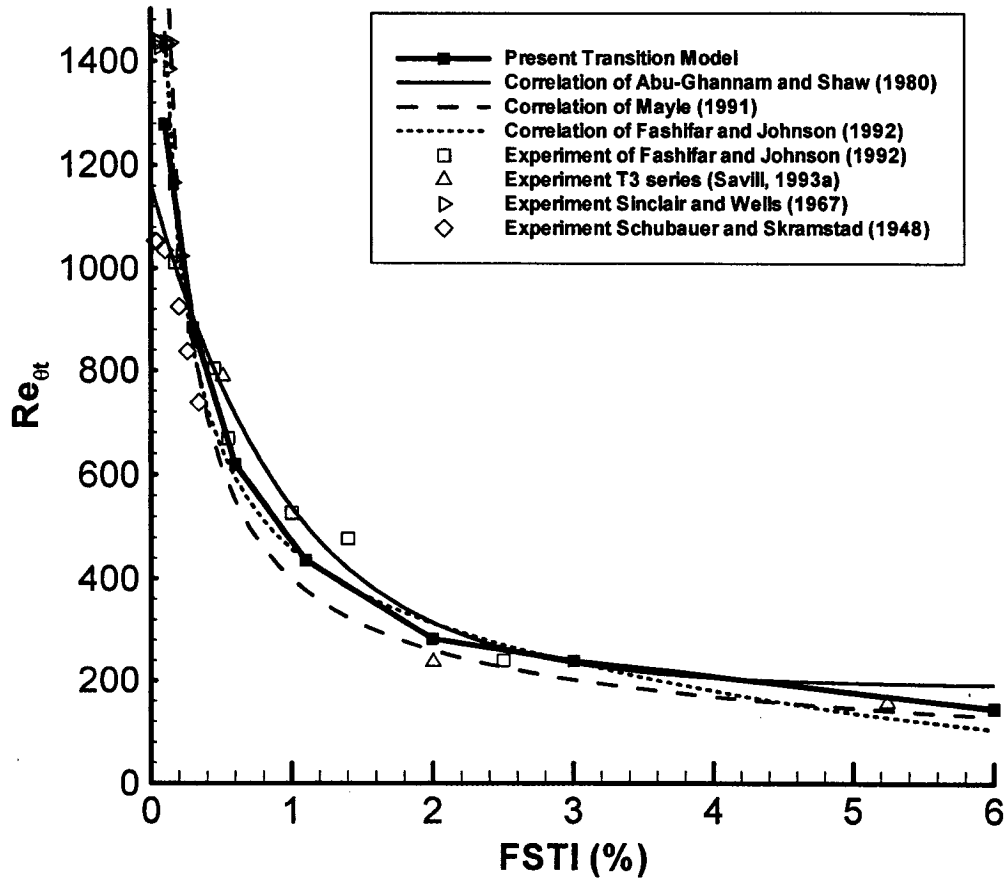

Figure 3.11 Predicted momentum thickness Reynolds number ($Re_{\theta t}$) at the onset of transition as a function of freestream turbulence intensity (FSTI) for zero pressure gradient flow.

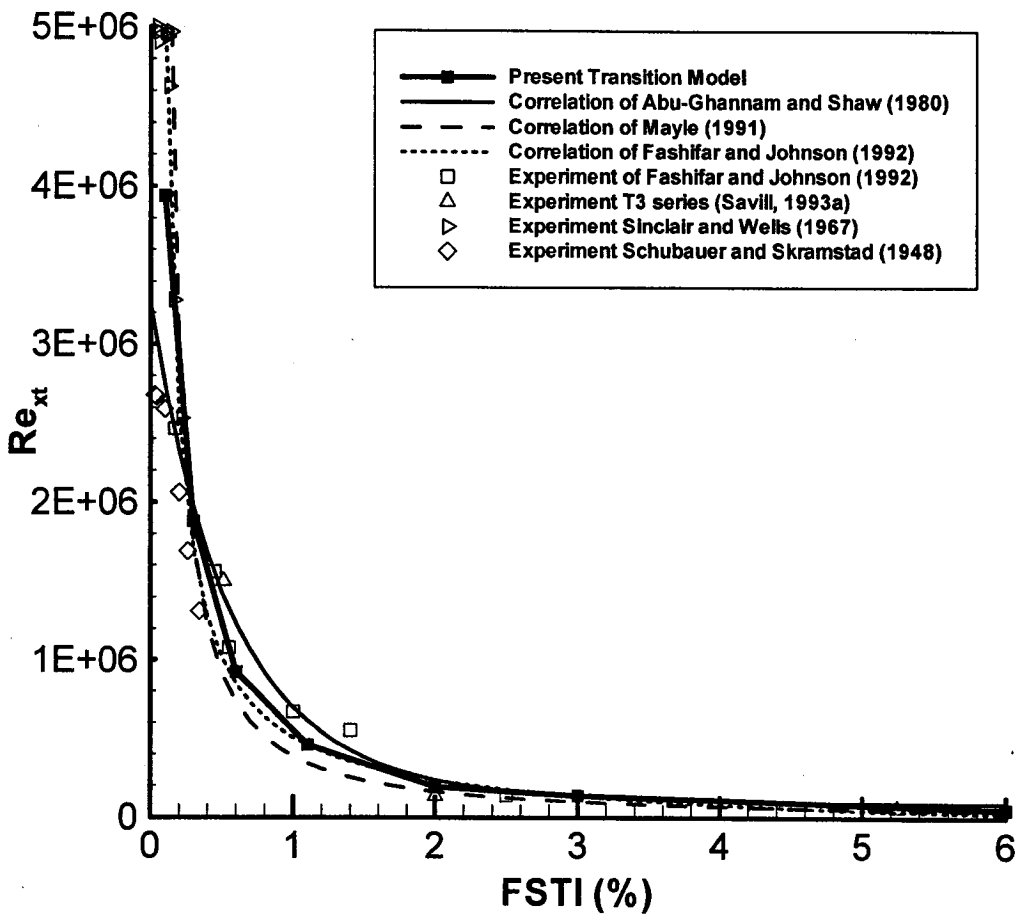

Figure 3.12 Predicted Reynolds number (Re_{xt}) at the onset of transition as a function of freestream turbulence intensity (FSTI) for zero pressure gradient flow.

We now have a low-Reynolds number turbulence model that is capable of properly reproducing the effect of the freestream turbulence intensity on the transition onset location. From Figures 3.11 and 3.12 there is a considerable amount of scatter in the empirical data and this is widely attributed to the effect of the freestream turbulent length scale and the measurement technique used to determine the onset location (Mayle, 1991). The present model has been calibrated to fall within the scatter of the empirical data.

The final step in the development of the present transition model is to examine the performance of the model under the influence of pressure gradients at different freestream turbulence intensities. From the experimental data in Figure 3.13 an adverse pressure gradient has a strong effect on the experimental transition onset location, particularly at lower turbulence intensities. The performance of the transition model under the influence of adverse and favorable pressure gradients was evaluated by varying the divergence/convergence angle of the upper wall boundary condition for the flat plate mesh. It was found that the model as it has been developed so far (i.e. the PTM_2 term equal to 0.0) predicted the zero and favorable pressure gradient data in Figure 3.13 reasonable well. However, in adverse pressure gradients the model predicted transition far too late.

In an adverse pressure gradient there exists an inflexion point in the laminar boundary layer velocity profile (White, 1991). This inflexion point has been theoretically proven to be destabilizing and is often referred to as the inviscid instability mode (White, 1991). From the poor results that were obtained in adverse pressure gradients it would appear that the vorticity Reynolds number is not capable of sufficiently accounting for the growth of k due to the presence of an inflexion point.

To incorporate the effect of an adverse pressure gradient on the onset location the PTM term must be increased whenever an adverse pressure gradient is present. This will be accomplished using the PTM_2 term that is included in Equation 3.32. The PTM_2 term will only be active in adverse pressure gradients. In zero and favorable pressure gradients it will be equal to 0.0. The logical choice for a dependant variable for the

PTM_2 term is a non-dimensional pressure gradient parameter (K). The pressure gradient parameter defined by Steelant and Dick (2001) has been used with the present transition model. Steelant and Dick based their reference quantities for μ, ρ and U on the freestream values. However, in keeping with the requirements stated in the introduction of this chapter the transition model has been calibrated using local values. Steelant and Dick's pressure gradient parameter is defined as follows:

$$K = -\frac{\mu}{\rho^2 U^3}\left[1 - M^2\right]\frac{dp}{ds} \tag{3.33}$$

where dp/ds is the pressure gradient along the streamline. A negative value for K indicates an adverse pressure gradient while a positive value indicates a favorable pressure gradient. For incompressible flows the Mach number term $[1\text{-}M^2]$ can be omitted.

Based on Figure 3.13 it is possible to determine the required form of the PTM_2 term that will allow the transition model to reproduce the empirical data. The largest effect of an adverse pressure gradient on the transition onset location occurs at smaller pressure gradient levels. For larger adverse pressure gradients levels the effect appears to approach an asymptote. This implies an inverse dependence on the magnitude of the pressure gradient parameter ($K^{1/n}$). As well, for lower transition Reynolds numbers the pressure gradient has less of an effect. This implies that there is also a dependence on the vorticity Reynolds number. The final form of the PTM_2 term is as follows:

$$PTM_2 = \begin{cases} -|K|^{0.4}\,\dfrac{\mathrm{Re}_v}{80}, K < 0 \\ 0, K \geq 0 \end{cases} \tag{3.34}$$

From Figure 3.13, the new transition model appears to be just as capable of reproducing the experimental onset data of Fashifar and Johnson (1992) as the widely used empirical correlation of Abu-Ghannam and Shaw (1980). The effect of an adverse

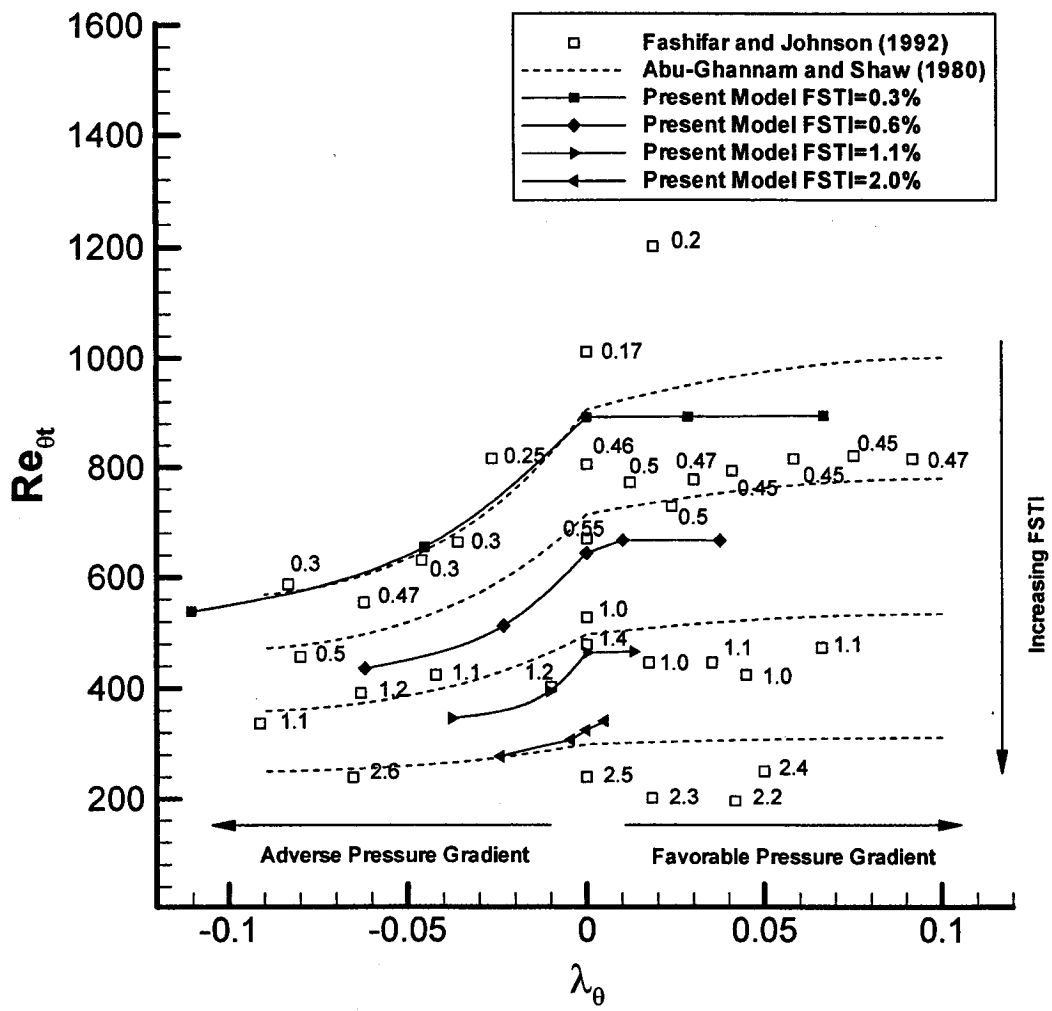

Figure 3.13 Predicted transition onset under the influence of pressure gradient and freestream turbulence intensity (FSTI).

pressure gradient on the PTM term is shown in Figure 3.10 for two different values of K, -7.25E-8 and -2.94E-7. These values of K are representative of those encountered in the two adverse pressure gradient cases used to calibrate the model in Figure 3.13. Increasing the PTM term increases the production of k in the laminar boundary layer and hence causes earlier transition. From Mayle (1991) the effect of a pressure gradient is negligible for freestream turbulence intensities greater than 3 percent. From Figure 3.10, the PTM term computed for different pressure gradient levels is almost identical to the zero pressure gradient value for Re_v values representative of transition at 3 percent freestream turbulence intensity. The new transition model therefore appears to capture quit well the combined effect of freestream turbulence intensity and pressure gradient.

This concludes the development of the new transition model. From Figures 3.11, 3.12 and 3.13 the model appears to have the proper sensitivity to freestream turbulence intensity and pressure gradient. The new transition model has been validated against a large number of diverse and challenging test cases. The next three chapters will present the results from these test cases, which include the ERCOFTAC T3-series and the PAK-B low-pressure turbine blade at steady conditions and influenced by a periodic impinging wake.

Chapter 4
ERCOFTAC Test Cases

4.1 Introduction

The new transition model developed in the previous chapter has been used to predict the European Research Community On Flow Turbulence And Combustion (ERCOFTAC) T3 series of experimental test cases. These experiments were performed by researchers at Rolls Royce in the early 1990's (Savill, 1992). The T3 series of test cases (T3A, T3B, T3AM, T3C5, T3C2, T3C3, T3C4) have often been used to evaluate the ability of transition models to predict the onset and length of transition. They have become the standard test cases against which all transition models are compared.

The T3 measurements were performed on a flat plate subjected to different levels of isotropic freestream turbulence and pressure gradient. Test cases T3A, T3B and T3AM had zero pressure gradient with freestream turbulence intensities of 3, 6 and 1 percent. These test cases are primarily used to determine the ability of a transition model to predict the effect of freestream turbulence intensity on the onset location of transition. The T3C test cases had a pressure gradient that is representative of an aft-loaded turbine blade and freestream turbulence levels of 2.5 percent. The Reynolds number for these test cases was progressively lowered so that the transition onset location moved from the favorable pressure gradient region at the leading edge to the adverse pressure gradient at the end of the plate. The T3C test cases are therefore excellent tests for the combined effect of pressure gradient and boundary layer history on the predicted onset and length of transition.

4.2 Problem Geometry and Mesh definition

The T3 computations were performed with a C-mesh that consisted of 236x90 cells. The flat plate had a circular leading edge with a radius of 0.75 mm. The mesh used for the zero pressure gradient test cases is shown in Figure 4.1. The distance between the first cell center and the wall was specified so that a y^+ of 1.0 or less was present at all times. There were at least 25 cells in the laminar boundary layer at all stream-wise locations. For the T3C test cases the pressure gradient was imposed by varying the contour shape of the upper slip wall. The required area variation between the flat plate and the upper slip wall was computed from the experimental C_p data. The mesh used for the T3C pressure gradient cases is shown in Figure 4.2. The Reynolds number (Re_x) for all the T3 test cases is based on the freestream velocity at the flat plate leading edge. For all the computations, further grid refinement had no significant effect on the final solution.

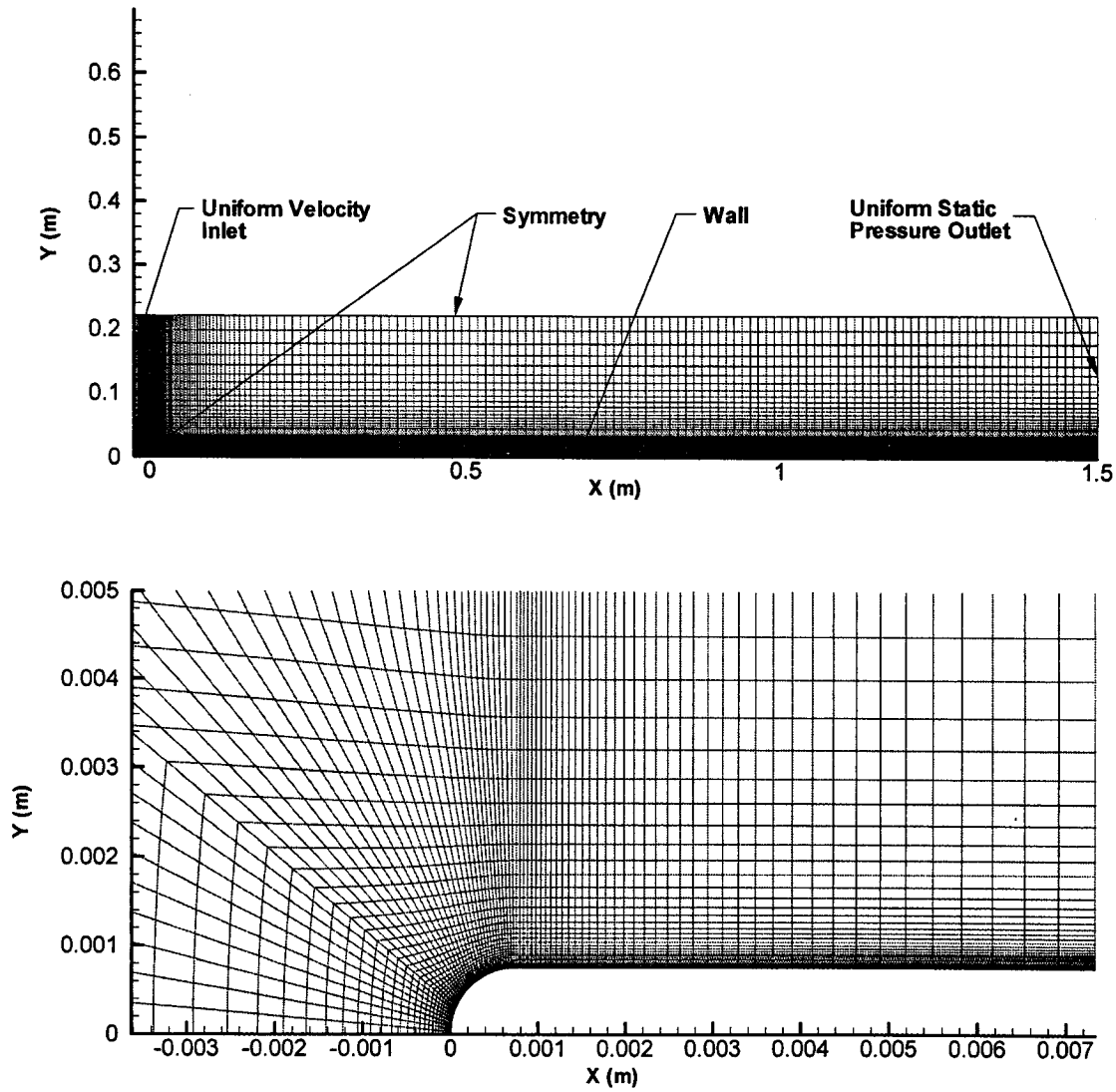

Figure 4.1 Flat plate mesh used to compute the T3A, T3B and T3AM test cases.

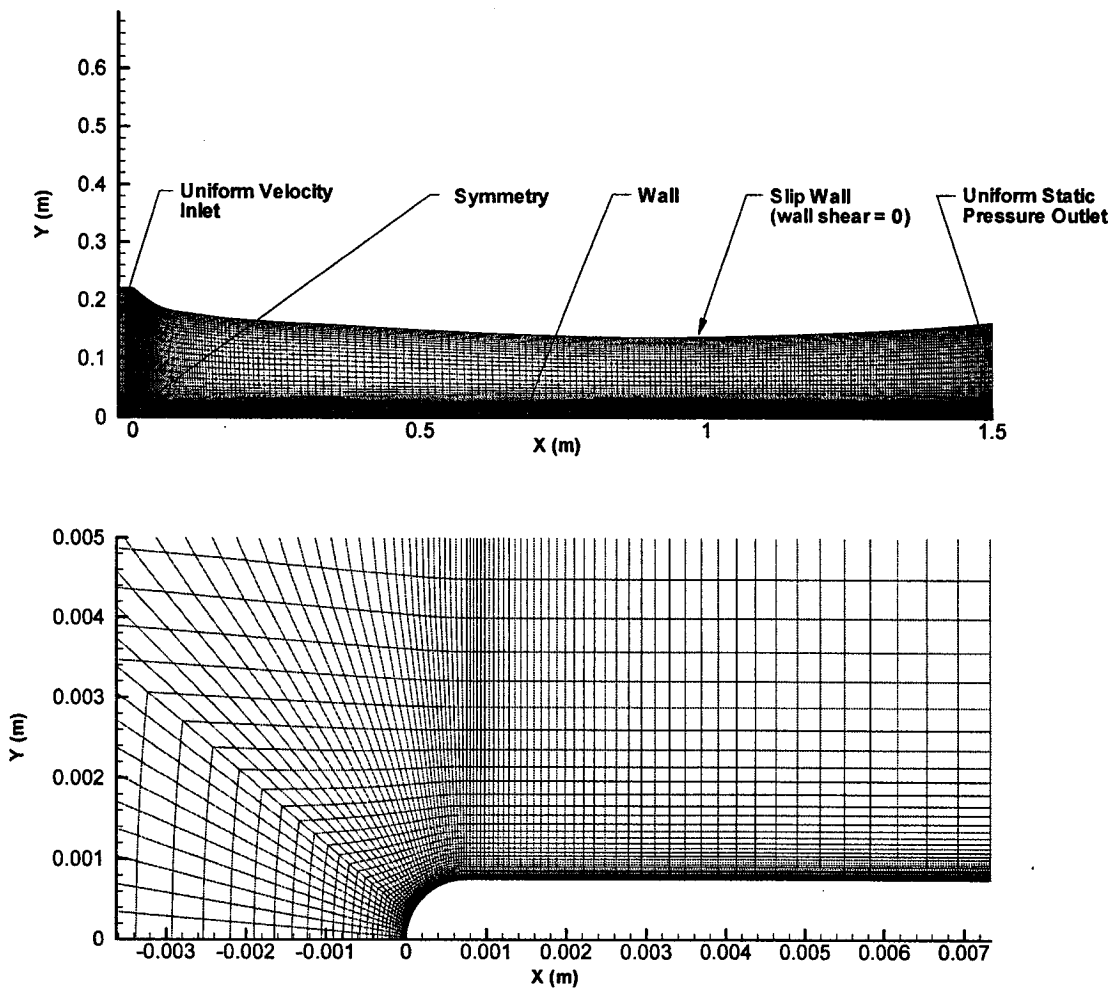

Figure 4.2 Flat plate mesh used to compute the T3C test cases.

4.3 Zero Pressure Gradient Test Cases

4.3.1 T3A

The freestream turbulence intensity at the leading edge of the flat plate for the T3A test case was 3.3 percent. The decay of freestream turbulence intensity was matched with the experimental data by specifying an inlet freestream viscosity ratio of 12.4. Since the onset of transition predicted by the model is dependent on the local freestream intensity an accurate onset prediction requires that the decay rate match the experiment. The freestream turbulence intensity from the experiment and the simulations is shown in Figure 4.3. The predicted decay rate is in reasonably good agreement with the experiment.

The computed skin friction coefficient is compared to the experimental data in Figure 4.4. Also shown are the transition onset locations given by the empirical correlations of Mayle (1991), Abu-Ghannam and Shaw (1980) and Fashifar and Johnson (1992). The new transition model predicts the onset of transition within the range of the correlations and is in generally good agreement with the experimental measurements.

From Figure 4.4, the skin friction starts to deviate from the Blasius value as the flow develops. In the experiment, this effect is caused by the distortion of the boundary layer profile due to the growing laminar fluctuations. It is interesting that this effect is reproduced by the computations, although it is somewhat over predicted.

4.3.2 T3B

The freestream turbulence intensity at the leading edge of the flat plate for the T3B test case was 6.2 percent. The decay of freestream turbulence intensity was matched with the experimental data by specifying a freestream viscosity ratio of 86.7. The freestream turbulence intensity from the experiment and the simulations is shown in Figure 4.5. The

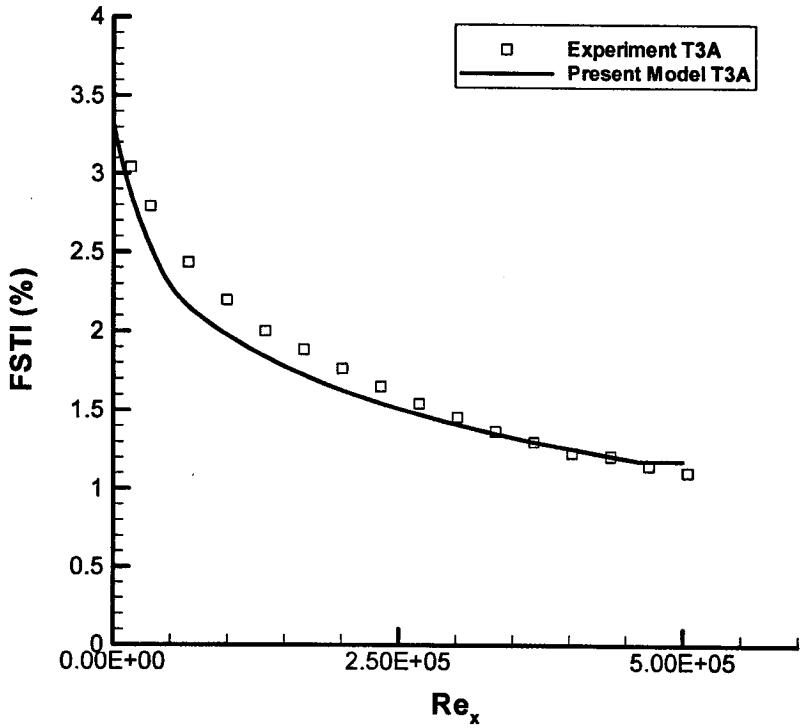

Figure 4.3 Comparison of freestream turbulence intensity (FSTI) for the T3A test case.

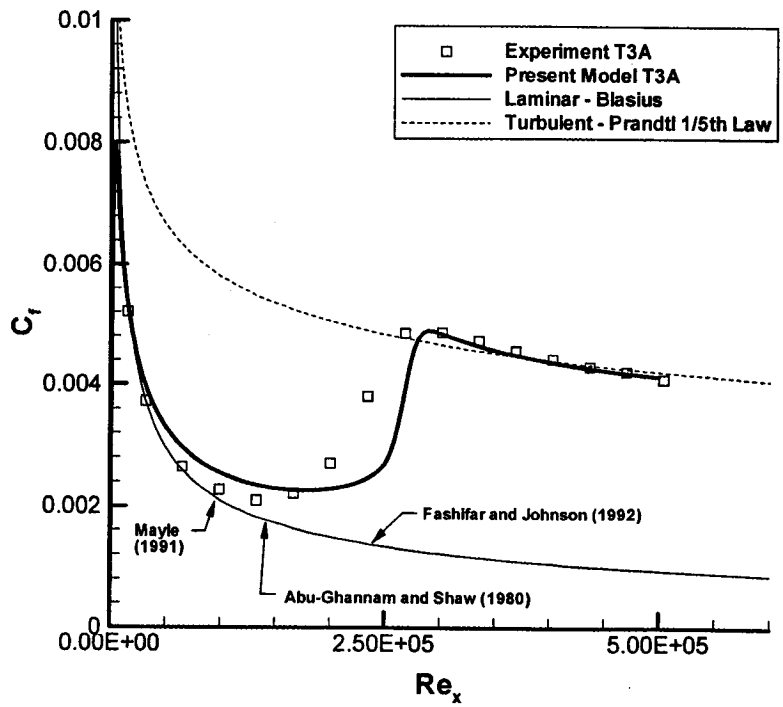

Figure 4.4 Comparison of skin friction coefficient (Cf) for the T3A test case.

predicted decay rate is somewhat larger than the measurements. However, near the leading edge where the onset of transition occurs the freestream turbulence intensity in the computation and experiment are reasonably close.

The computed skin friction coefficient is compared to the experimental data in Figure 4.6. The transition model has predicted the onset of transition slightly before the experimental location. As well, the deviation from the Blasius skin friction is quite significant in this case due to the proximity of the transition to the circular leading edge.

4.3.3 T3AM

The freestream turbulence intensity at the leading edge of the flat plate for the T3AM test case was 0.9 percent. The decay of freestream turbulence intensity was matched with the experimental data by specifying a freestream viscosity ratio of 8.9. The freestream turbulence intensity from the experiment and the simulations is shown in Figure 4.7. For this case, the predicted decay rate is in very good agreement with measurements.

The computed skin friction coefficient is compared to the experimental data in Figure 4.8. Clearly, the model has predicted a turbulent boundary layer over the entire length of the flat plate. This is because in the computation a small separation bubble was present at the leading edge of the plate (see Figure 4.9 and 4.10, top). We know from Chapter 3, Figure 3.7, that a separation bubble results in a large increase in the local vorticity Reynolds number. As a result, the local PTM term became quite large and the model predicted a significant increase in the growth of k. This in turn caused transition to occur in the free shear layer of the separation bubble.

According to Savill (2002), in the T3 experiments the incidence of the flat plate was carefully controlled to avoid leading-edge separation. It is therefore quite possible that in the T3AM test case the stagnation point was located somewhere on the upper surface of the flat plate and thus the separation bubble was suppressed. A simple way to suppress the separation bubble in the computations is to change the circular leading edge to an

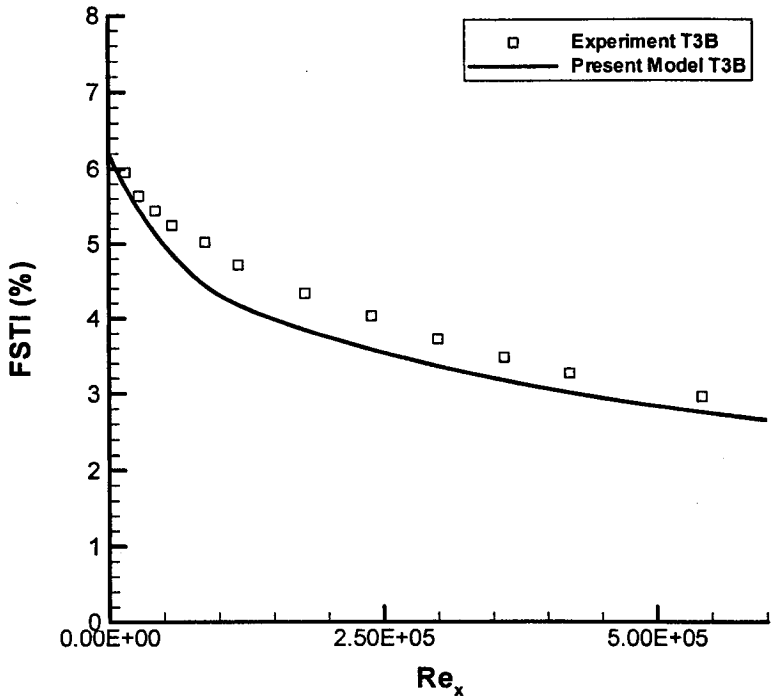

Figure 4.5 Comparison of freestream turbulence intensity (FSTI) for the T3B test case.

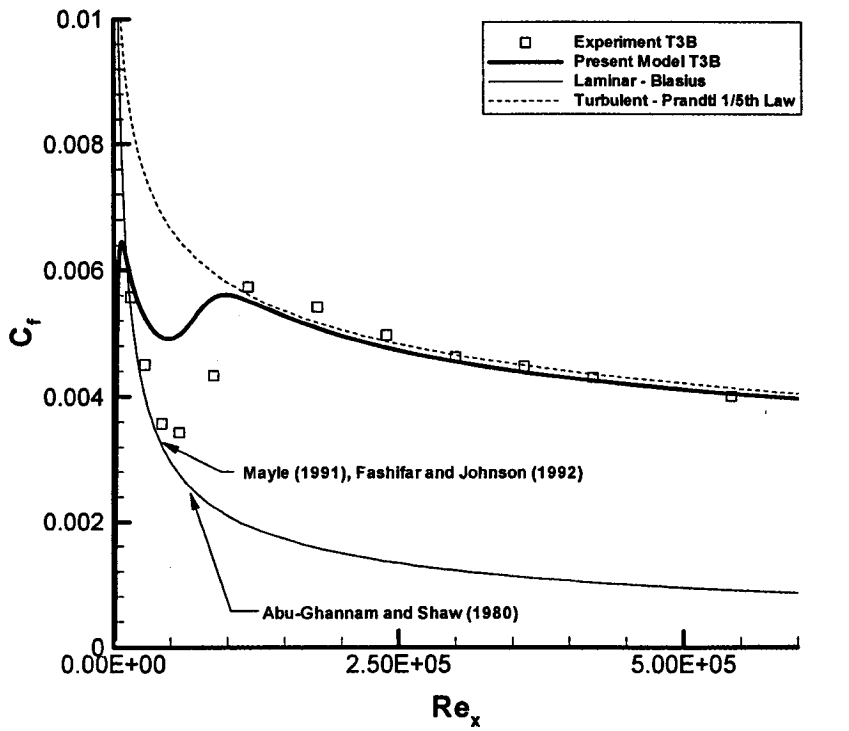

Figure 4.6 Comparison of skin friction coefficient (Cf) for the T3B test case.

elliptical leading edge. The results of this change are shown in Figures 4.8, 4.9 and 4.10 (bottom). Clearly, once the bubble is suppressed the transition onset is located far downstream of the leading edge. It is well known that leading edge separation bubbles can trip the flow and result in a turbulent boundary layer. In light of this, the fact that the model predicted transition due to the presence of the leading edge separation bubble is actually quite encouraging.

From Figure 4.8 even with an elliptical leading edge the onset is predicted far too early compared to the experiment. However, the predicted onset is within the scatter of the different empirical correlations. From Chapter 3, Figure 3.12 for a constant freestream turbulence intensity of 0.45 percent (i.e. the local turbulence intensity at the T3AM experimental onset location) the model predicts a transition Reynolds number of 1.4×10^6, which is comparable to the T3AM experiment. The discrepancy between the experimental onset location and that predicted by the model could simply be due to the fact that the model (and the empirical correlations to a certain extent) is far more sensitive to the freestream turbulence intensity at the leading edge of the plate then the local turbulence intensity.

4.4 Pressure Gradient Test Cases

4.4.1 T3C5

For the T3C5 test case, transition occurs in a favorable pressure gradient. The freestream turbulence intensity at the leading edge is 2.8 percent. The decay of the measured freestream turbulence intensity was matched by specifying a freestream viscosity ratio of 13.5. The freestream turbulence intensity from the experiment and the simulations is shown in Figure 4.11. For this case, the predicted decay rate is in excellent agreement with the experiment.

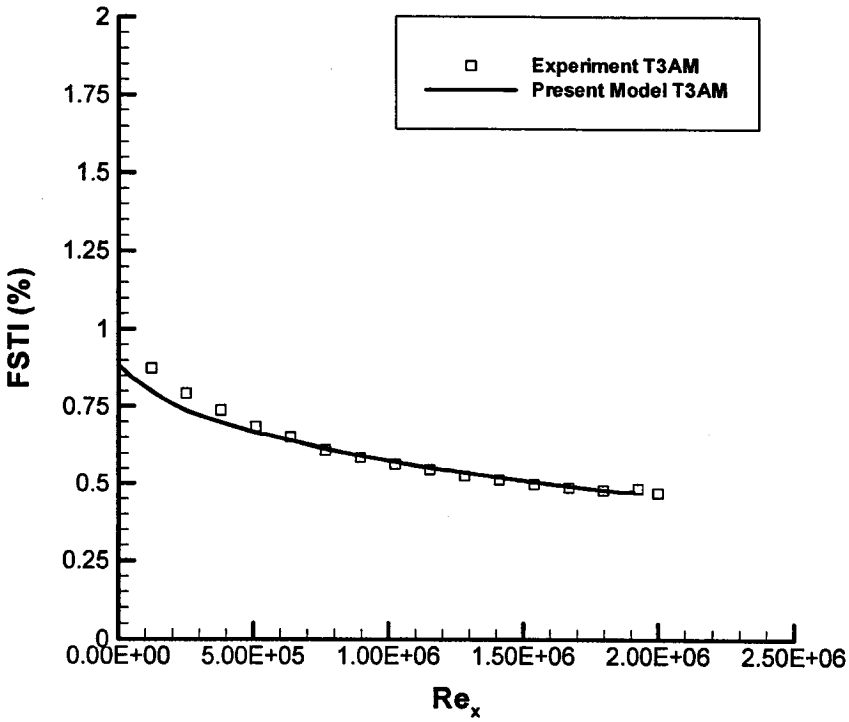

Figure 4.7 Comparison of freestream turbulence intensity (FSTI) for the T3AM test case.

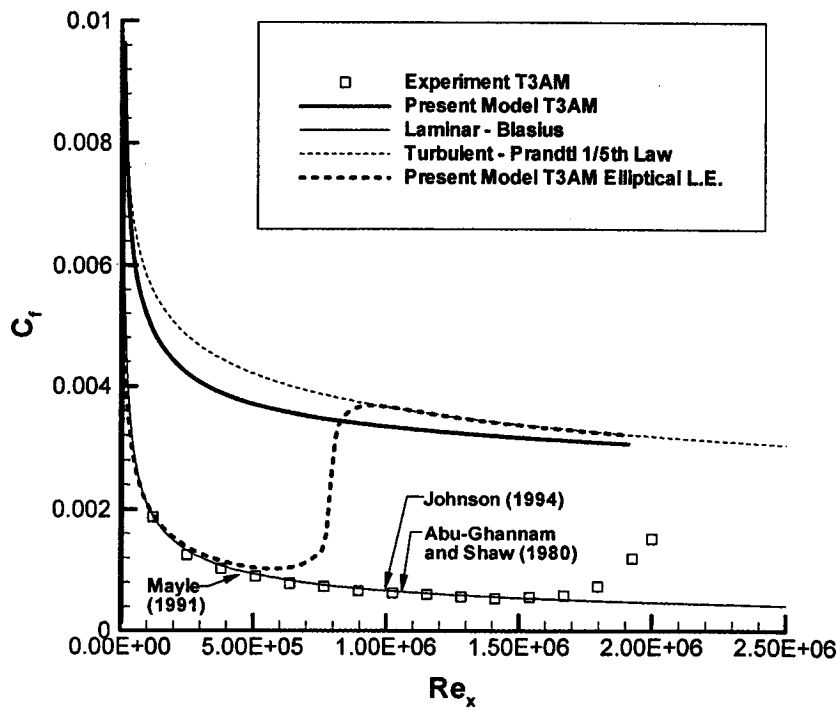

Figure 4.8 Comparison of skin friction coefficient (Cf) for the T3B test case.

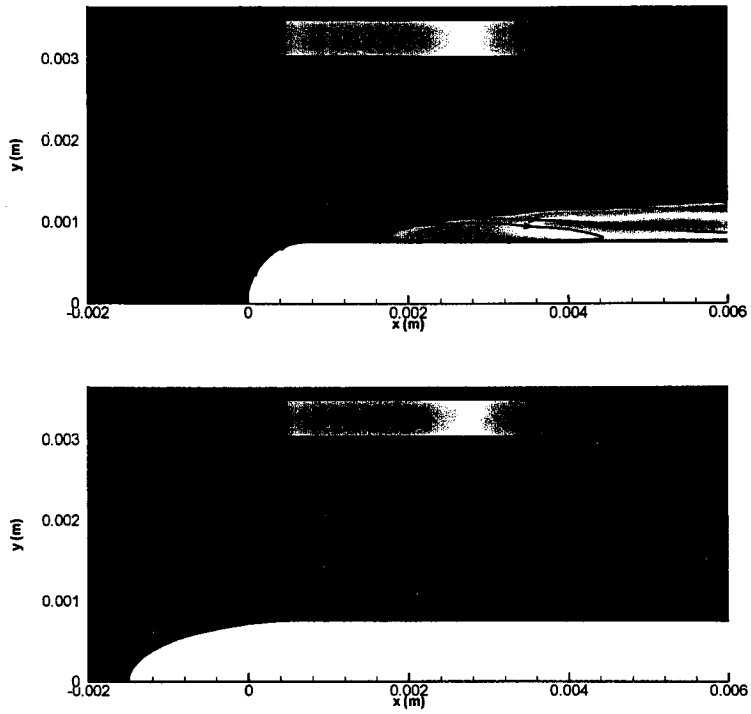

Figure 4.9 Contour plot of local turbulence intensity (Tu) in percent for T3AM with a circular leading edge (top) and an elliptical leading edge (bottom).

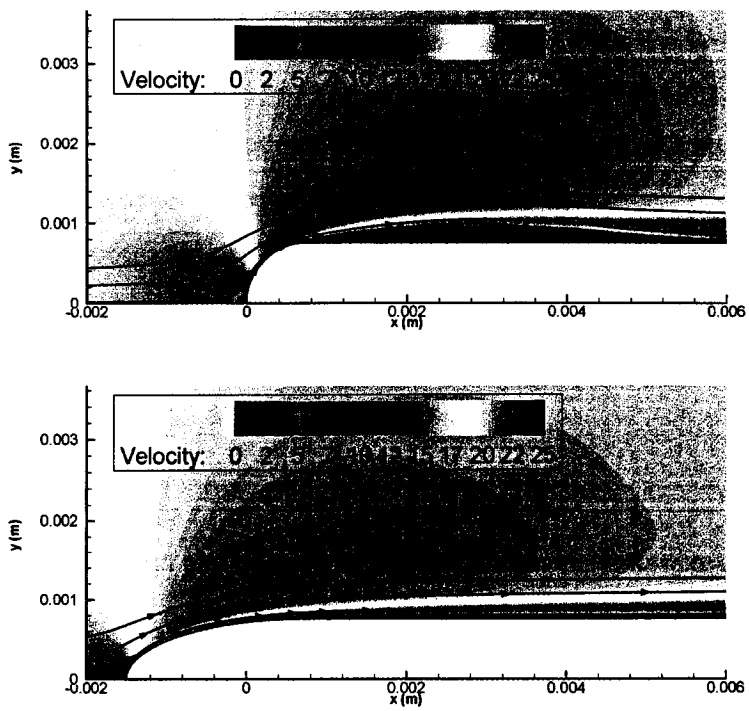

Figure 4.10 Contour plot of local velocity (m/s) for T3AM with a circular leading edge (top) and an elliptical leading edge (bottom).

The computed skin friction coefficient and freestream velocity are compared to the experimental data in Figure 4.12. The onset of transition was predicted significantly downstream of the experimental location. The momentum thickness Reynolds number (Re_θ) at the onset of transition in the experiment was 322 whereas in the simulation it was 403. For the same freestream turbulence intensity and local pressure gradient, the empirical correlations of Mayle (1991), Abu-Ghannam and Shaw (1980) and Fashifar and Johnson (1992) predict an onset Re_θ of 228, 313 and 446 respectively. Again, the new transition model gives results that are comparable in quality with the predictions from the established correlations.

4.4.2 T3C2

The experimental start of transition in the T3C2 case occurs in a favorable pressure gradient and the end of transition occurs in an adverse pressure gradient. The freestream turbulence intensity at the leading edge of the flat plate for the T3C2 test case was 2.8 percent. The decay of freestream turbulence intensity was matched with the experimental data by specifying a freestream viscosity ratio of 7.7. From Figure 4.13 the predicted decay rate is in excellent agreement with the measurements. The computed skin friction coefficient and freestream velocity are compared to the experimental data in Figure 4.14. The onset of transition was predicted slightly downstream of the experimental location in the adverse pressure gradient region and the transitional length was shorter than the experiment. Overall, the agreement between the computations and the experiment is fairly good.

4.4.3 T3C3

The experimental start and end of transition for this case occurs in an adverse pressure gradient. The freestream turbulence intensity at the leading edge was again 2.8 percent and the decay of freestream turbulence was matched with a freestream viscosity ratio of 4.8. The freestream turbulence intensity from the experiment and the simulations is shown in Figure 4.15. Again the predicted decay rate is in good agreement with the experiment.

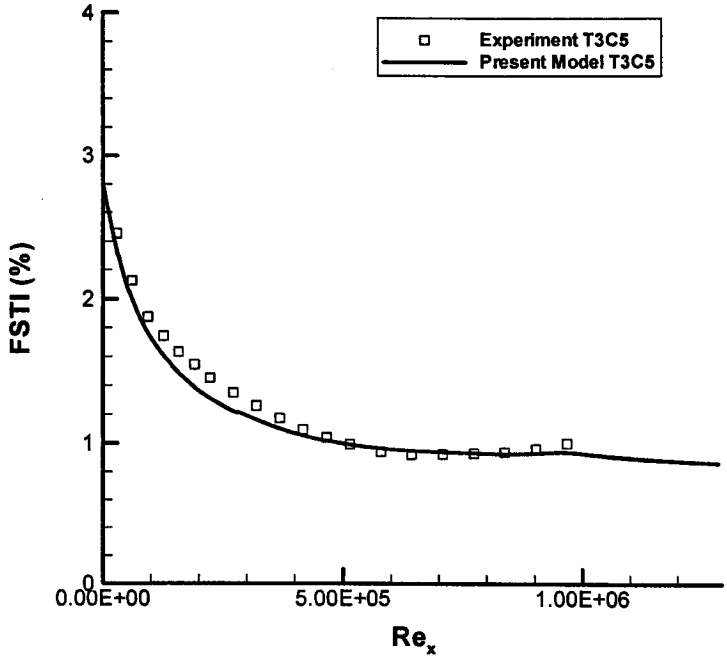

Figure 4.11 Comparison of freestream turbulence intensity (FSTI) for the T3C5 test case.

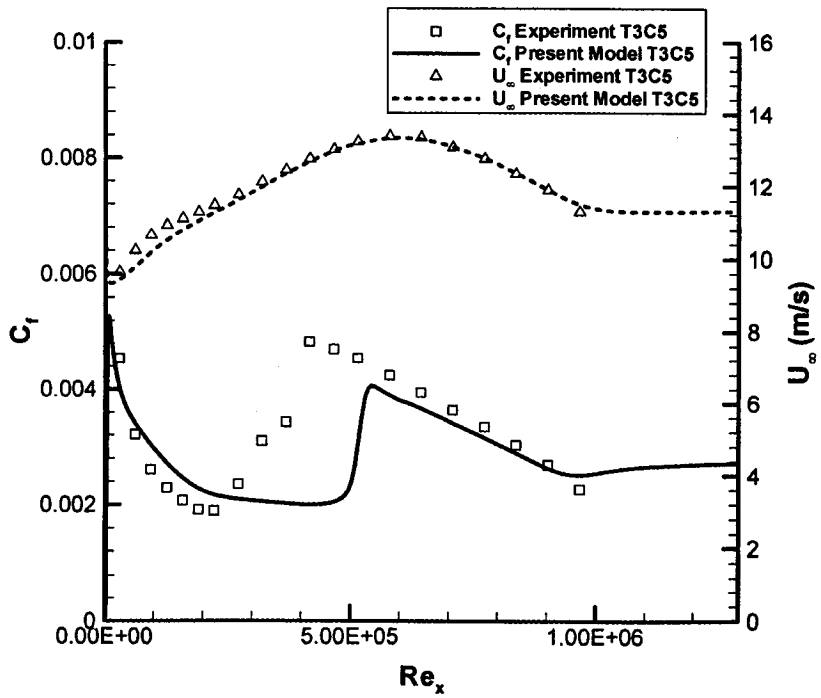

Figure 4.12 Comparison of skin friction coefficient (Cf) and freestream velocity (U_∞) for the T3C5 test case.

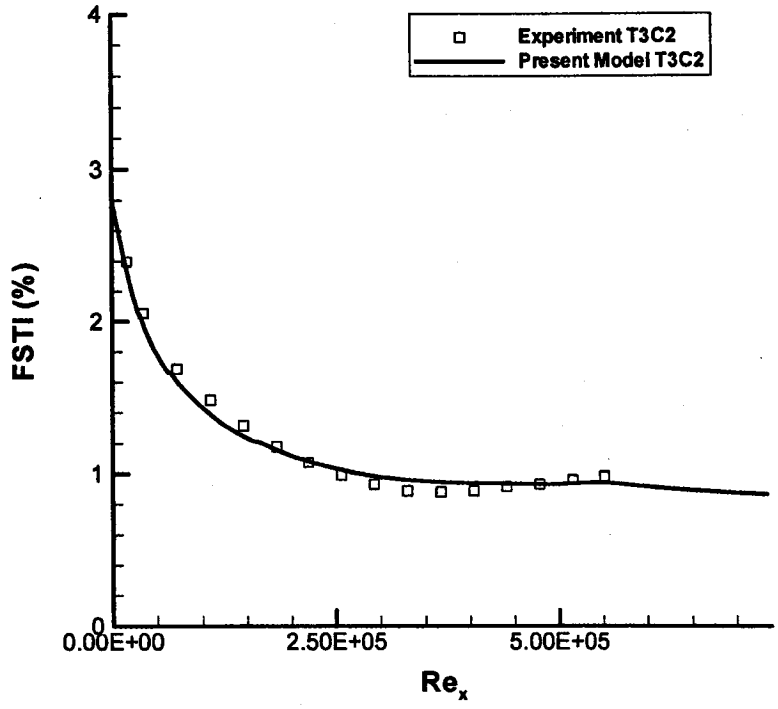

Figure 4.13 Comparison of freestream turbulence intensity (FSTI) for the T3C2 test case.

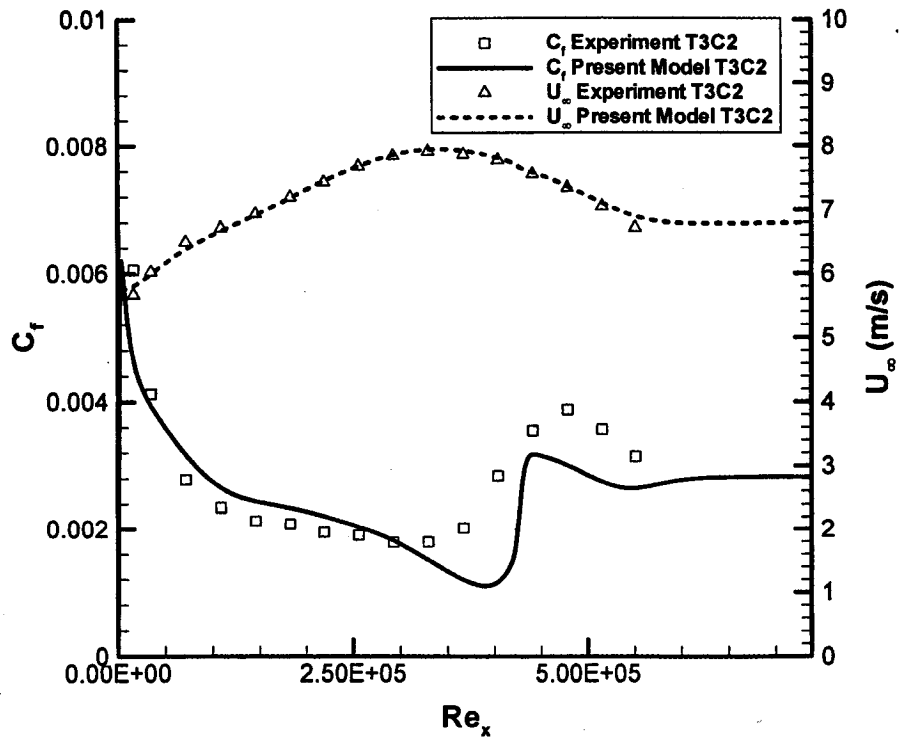

Figure 4.14 Comparison of skin friction coefficient (Cf) and freestream velocity (U_∞) for the T3C2 test case.

The computed skin friction coefficient and freestream velocity are compared to the experimental data in Figure 4.16. The predicted onset of transition is in excellent agreement with the experiment. However, the predicted transitional length is somewhat shorter than the experiment.

4.4.4 T3C4

For the last T3 test case, T3C4, the transitional boundary layer separates at a Re_x of 129 000 and reattaches as a turbulent boundary layer. The freestream turbulence intensity at the leading edge was 2.8 percent and the measured decay rate was matched by using a freestream viscosity ratio of 2.0. The experimentalal and computation freestream turbulence intensities are show in Figure 4.17.

The computed skin friction coefficient and freestream velocity are compared with experiment in Figure 4.18. The boundary layer separates at the same location in both the computation and the experiment. However, the separation bubble in the computation is roughly twice the size of that in the measurements. Interestingly, the empirical correlation of Hatman and Wang (1998) for short separation bubbles indicates that the reattachment Reynolds number should be 172 000 and this compares quite well with the predicted reattachment Reynolds number of 165 000. The experiments of Hatman and Wang (1998) were for freestream turbulence intensities of 0.3 to 0.6 percent. One would expect that the reattachment Reynolds number would be reduced by the slightly higher freestream turbulence levels present in the T3C4 test case.

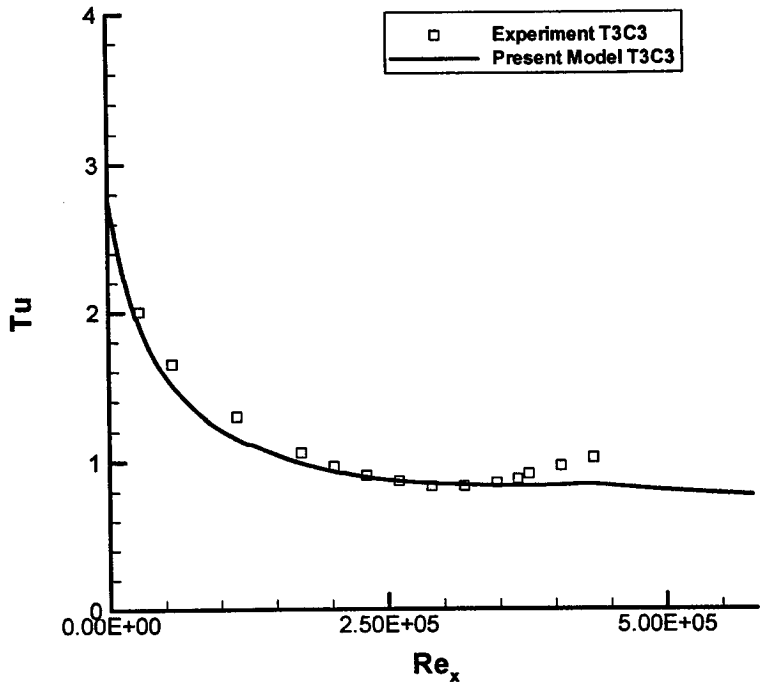

Figure 4.15 Comparison of freestream turbulence intensity (FSTI) for the T3C3 test case.

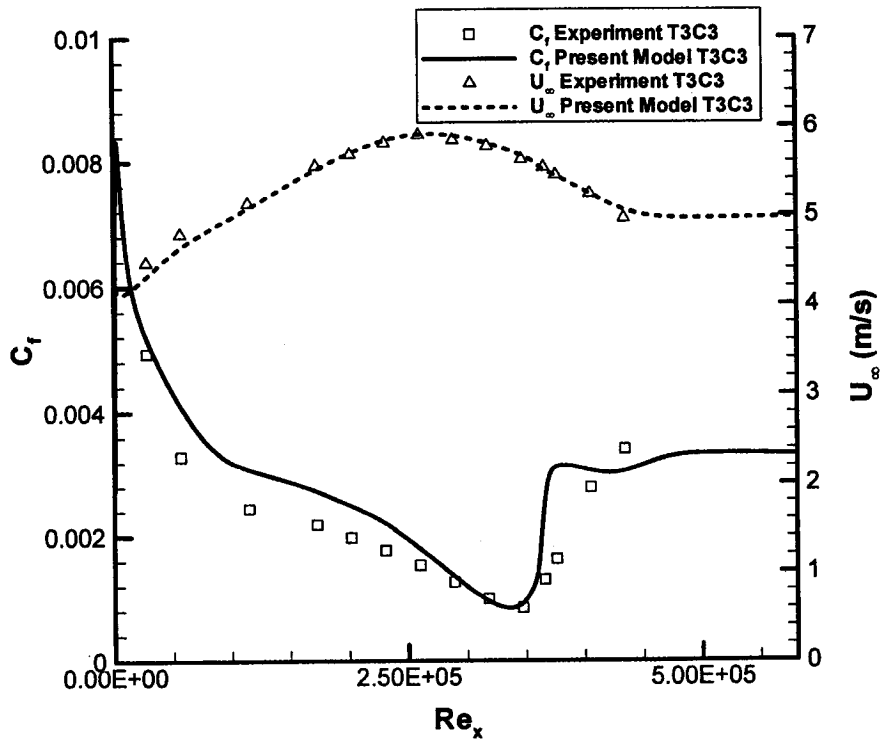

Figure 4.16 Comparison of skin friction coefficient (Cf) and freestream velocity (U_∞) for the T3C3 test case.

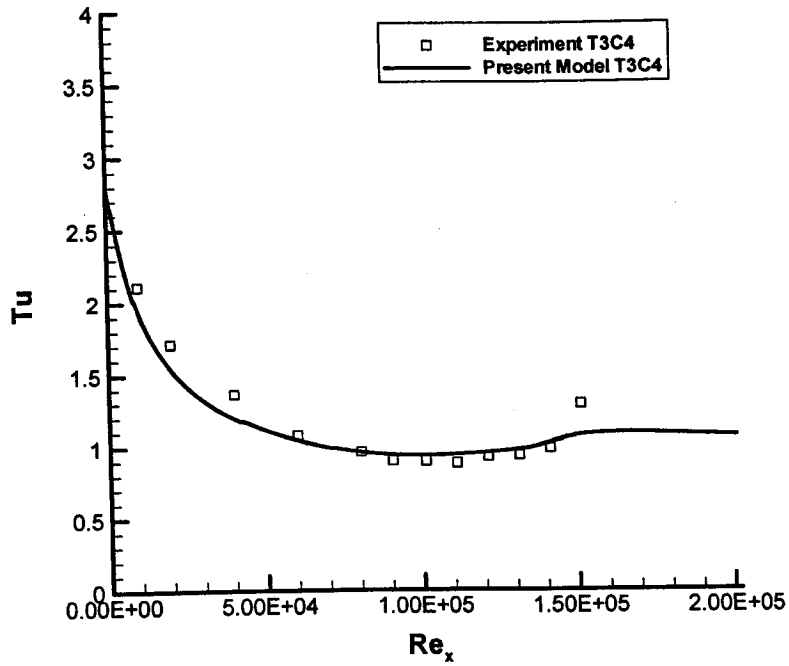

Figure 4.17 Comparison of freestream turbulence intensity (FSTI) for the T3C4 test case.

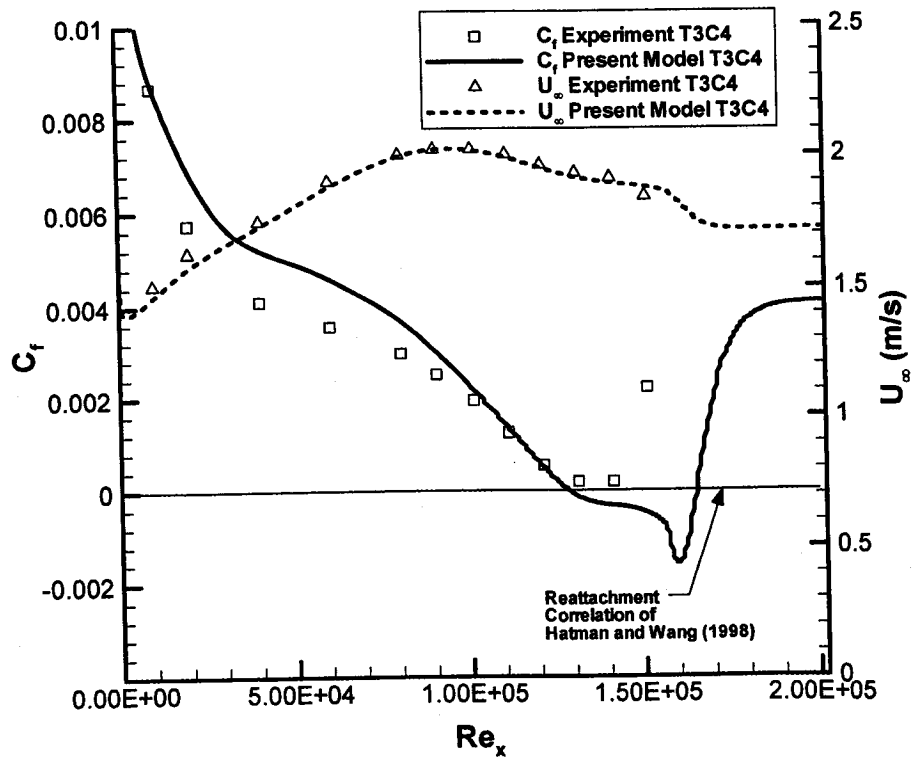

Figure 4.18 Comparison of skin friction coefficient (Cf) and freestream velocity (U_∞) for the T3C4 test case.

This concludes the validation of the new transition model against the ERCOFTAC T3 test cases. In general, good agreement was obtained and the model appears to be as accurate at predicting the onset location of transition as the available empirical correlations. Based on the encouraging results obtained from the T3 computations, particularly with respect to separation bubbles, the new transition model was applied to the Pratt & Whitney PAK-B low-pressure turbine airfoil. Low-pressure turbines are particularly challenging flow fields because the blade aerodynamics are dominated by transitional separation bubbles on the suction side. They are thus excellent test cases for the new transition models ability to predict separation induced transition. The PAK-B steady results will be the focus of the next chapter.

Chapter 5
Pak-B Low-Pressure Turbine Airfoil – Steady Results

5.1 Introduction

Based on the encouraging results obtained from the T3 computations, the new transition model was applied to the flow over the Pratt & Whitney PAK-B low-pressure turbine airfoil. The PAK-B turbine blade is a particularly interesting airfoil because it generates a loading profile similar to the rotors found in modern aircraft engines (Dorney et al, 2000). The low-pressure rotors on modern aircraft engines are extremely challenging flow fields. This is because in many cases the transition occurs in the free shear layer of a separation bubble on the suction side (Mayle, 1991). The onset of transition in the free shear layer determines whether or not the separation bubble will reattach as a turbulent boundary layer and ultimately, whether or not the blade will stall. The new transition model would therefore be of great interest to the turbine design community if it can accurately predict the transition onset location for these types of flows.

Zhang et al. (2002) have measured the blade loading and the quasi-wall-shear stress (using surface-mounted hot films) for the PAK-B airfoil in a low-speed linear cascade. The quasi-wall-shear stress was normalized by the upstream dynamic pressure, to obtain a quasi-skin-friction coefficient (C_f`). However, the hot-film sensors have not been calibrated and only qualitative comparisons should be made with the calculations. This is not a major concern because we are primarily interested in where the boundary layer separates and reattaches. It is believed that the hot-film sensors are reasonably accurate for measuring the separation and reattachment points based on a zero or near-zero output from the sensors (Zhang et al, 2002).

The results of the computations have been compared with the measurements of Zhang et al. (2002). The experiments where performed for two different freestream turbulence intensities (low and high) of 0.4 and 4.5 percent, and for Reynolds numbers, based on axial chord and inlet velocity, of 150,000, 100,000, 50,000 and 25,000. These results are detailed in sections 5.3, 5.4, 5.5 and 5.6. In section 5.7 the effect of Reynolds number on the blade profile losses is examined. The next section will discuss the mesh that was used in all the computations.

5.2 Problem Geometry and Mesh Definition

The grid used for the PAK-B computations is shown in Figures 5.1, 5.2 and 5.3. It consists of an O-mesh around the airfoil, two H meshes and a tri-primitive mesh. The first H-mesh was used to join the uniform velocity inlet boundary condition to the O-mesh. The second H-mesh is used to join the O-mesh to the tri-primitive mesh. The tri-primitive mesh is a special feature available in the FLUENT mesh generation program (GAMBIT) which splits a triangular patch into three rectangular patches. It is essentially an automatic multi-block mesh generator. The tri-primitive mesh was used because it allows the second H-mesh to be aligned along the flow direction (thus reducing the numerical discritization error) while still allowing periodic boundary conditions to be used. The O-mesh consisted of 535x60 (streamwise x tangential) cells. The streamwise cells in the O-mesh were clustered around the trailing edge on the suction side of the airfoil (see Figure 5.3) in order to properly resolve the separation bubble that was present there. The total number of cells in the grid was about 72,000. A minimum y^+ of 1.0 or less was maintained everywhere. Further grid refinement was found to have a negligible effect on the predicted blade loading and skin friction.

The inlet flow values were identical to the experiment except for the turbulent quantities in the high turbulence intensity cases. For the latter cases, the decay rate of the freestream turbulence was very small by the time the flow reached the cascade leading edge. Exceptionally high values of the freestream eddy viscosity ratio where required

($R_T \approx 1000$) to match this decay rate. These high levels of freestream eddy viscosity seemed to result in unrealistically wide wakes behind the blade. To correct this problem the turbulent length scale at the inlet was reduced by a factor of 10. The resulting freestream viscosity ratios gave more physically reasonable behavior of the wakes. To compensate for the resulting increased decay rate of the turbulence, the turbulence intensity at the inlet to the grid was increased so that at the blade leading edge the turbulence intensity was matched to the experimental value of 4.5 percent. For all the high freestream turbulence intensity cases, the inlet turbulence intensity was 5.5 percent and the length scale used to compute ω was 0.628 (mm).

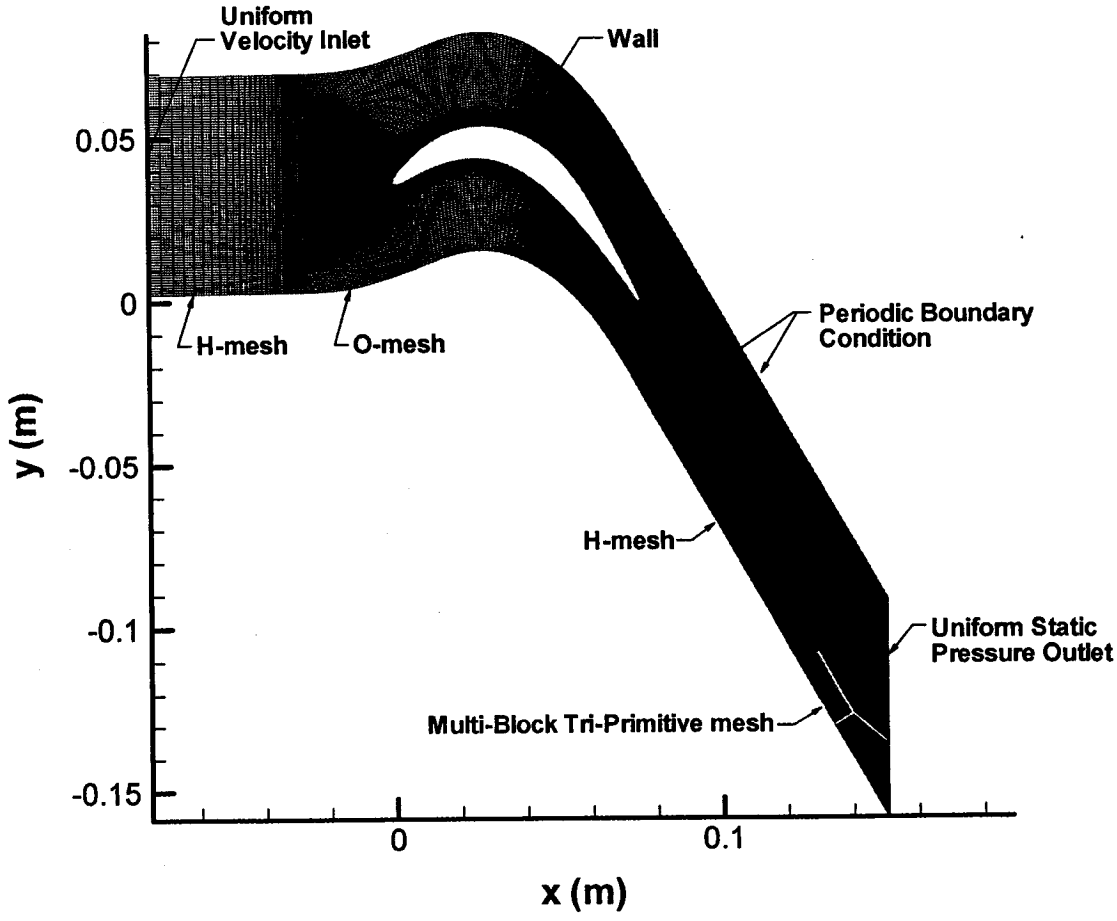

Figure 5.1 PAK-B mesh used for all steady computations.

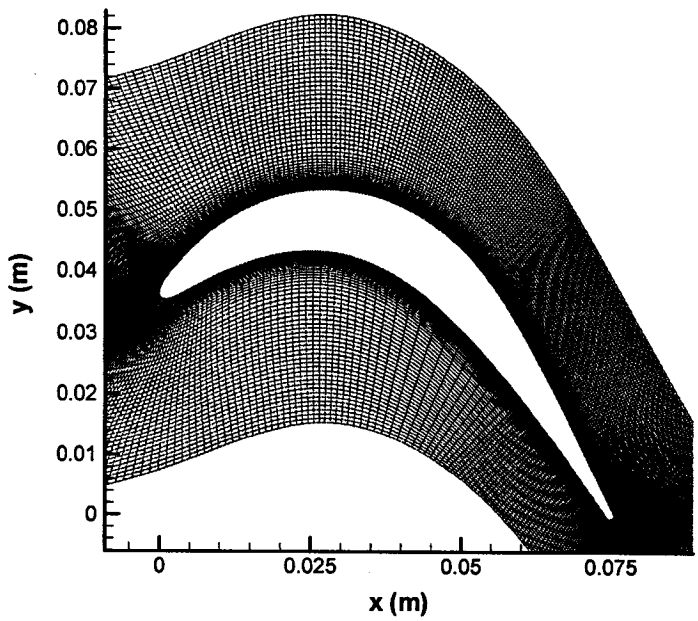

Figure 5.2 O-mesh around the PAK-B airfoil

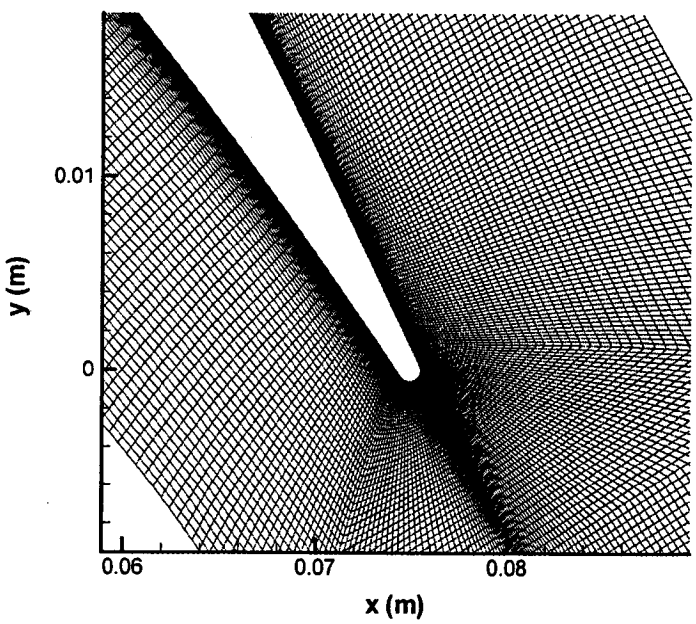

Figure 5.3 Trailing edge mesh around the PAK-B airfoil

5.3 PAK-B, $Re_x = 150{,}000$

The predicted blade loading and skin friction for a Reynolds number of 150 000 is shown in Figure 5.4. For the high turbulence intensity case, the model predicts the onset of transition before the boundary layer separates. For the low turbulence intensity case, the model predicts a small separation bubble that reattaches as a turbulent boundary layer. From the hot film data in the experiment for both low and high turbulence levels there appears to be a small separation bubble. The experimental bubble length is in very good agreement with the predictions for the low turbulence intensity case.

It should be noted that the quasi-wall-shear stress values provided by the surface hot films are only semi-quantitative in nature. The rise in the quasi-wall-shear stress on the forward half of the suction surface, seen in Figure 5.4 and subsequent figures, is believed to be the result of the effects of the varying pressure gradient on the response of the surface hot films. On the other hand, zero or near-zero output from the sensors is believed to indicate very low shear stress and therefore the presence of a separation bubble. Likewise, it is believed that the RMS of the fluctuations in the hot-film signal can be used to infer the presence of boundary layer transition.

The contours of turbulence intensity (Tu) and velocity for the high and low turbulence intensity cases are shown in Figures 5.5 and 5.6. For both turbulence intensities the model predicts a laminar boundary layer on the pressure side of the blade. Following Mayle (1991) we will refer to the region between 10 and 50 percent chord on the pressure side as the cove. In both cases there is a small cove separation bubble right after the leading edge and a noticeable increase in the local turbulence intensity is observed. This separation bubble does not appear to be strong enough to cause transition on the pressure side. The increased turbulence intensity due to the cove separation bubble slowly decays as it convects along the pressure side of the blade.

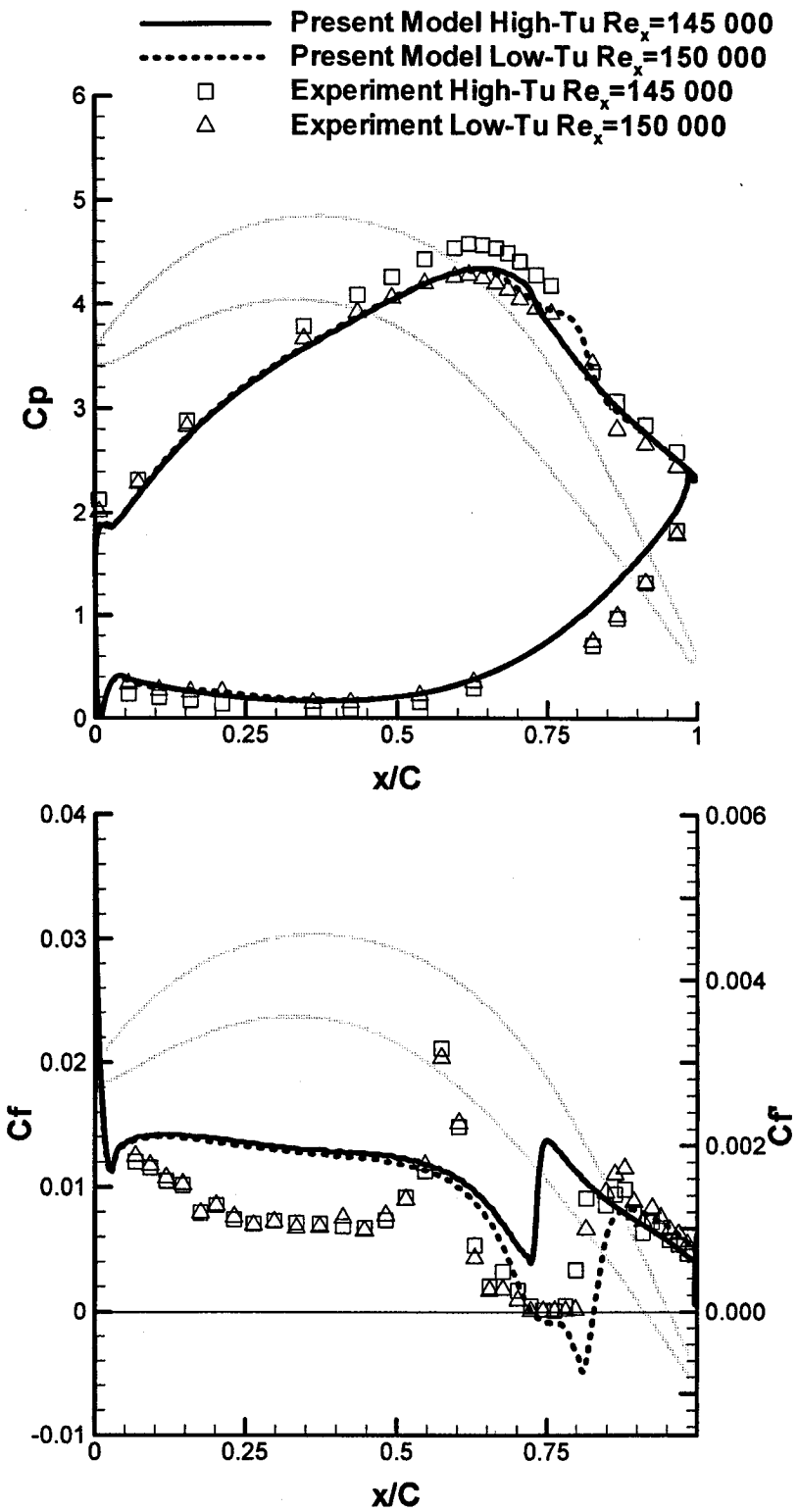

Figure 5.4 Predicted and experimental blade loading (Cp) and skin friction coefficient (Cf)/quasi-skin-friction coefficient (Cf') at an axial Reynolds number of 150,000.

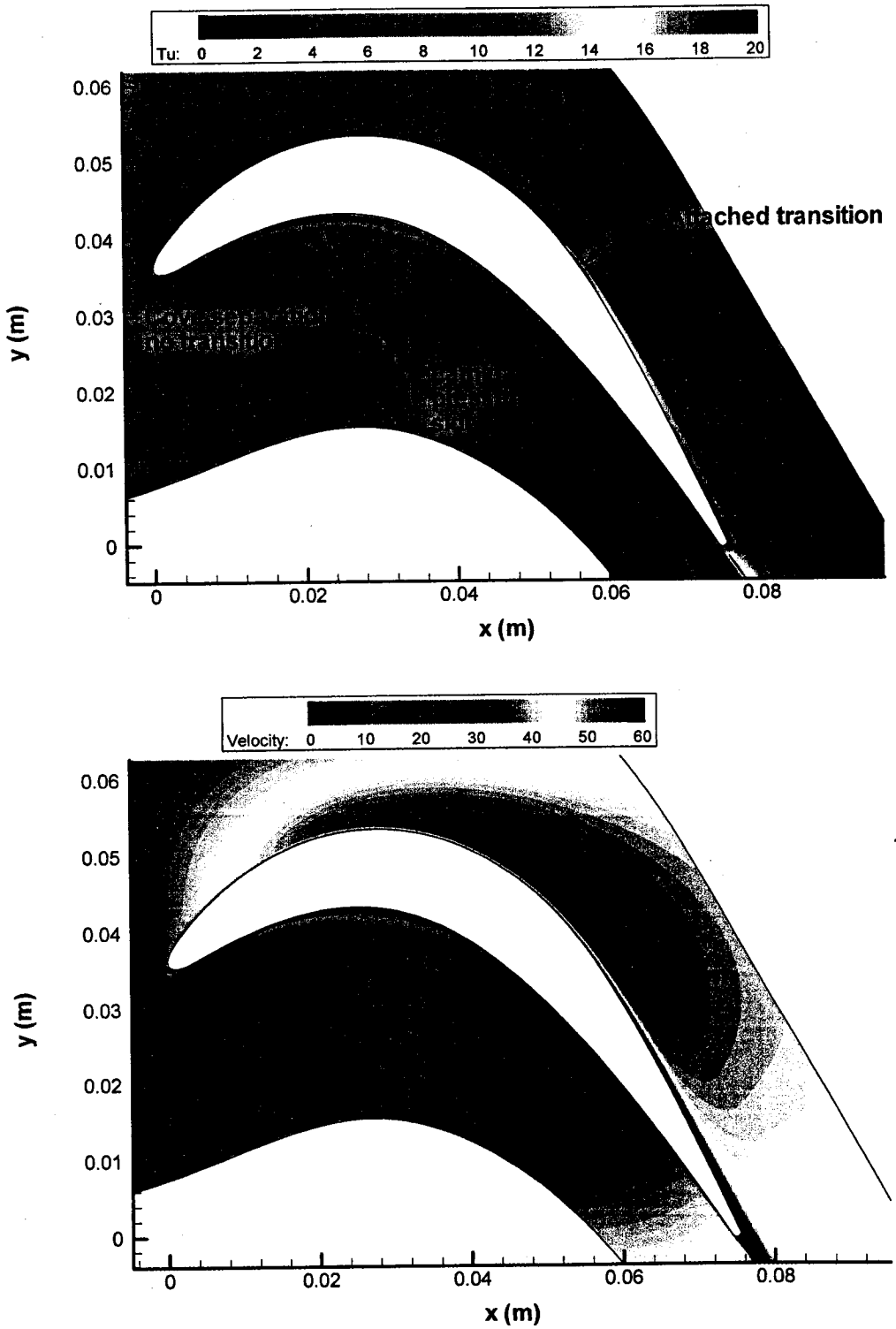

Figure 5.5 Contour plot of turbulence intensity (Tu, top) in percent and velocity (m/s, bottom) for the 150,000 axial Reynolds number, high turbulence intensity case.

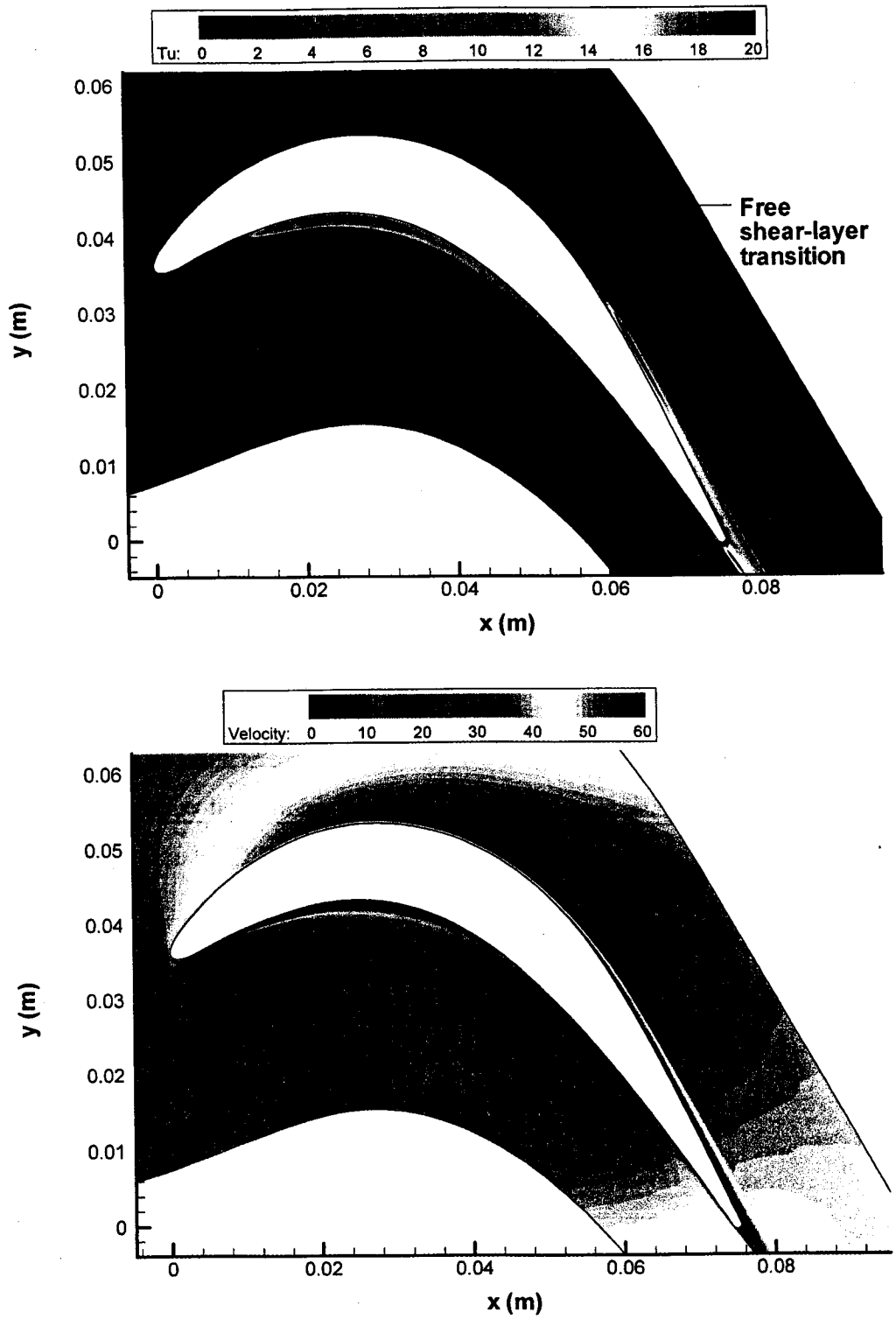

Figure 5.6 Contour plot of turbulence intensity (Tu, top) in percent and velocity (m/s, bottom) for the 150,000 axial Reynolds number, low turbulence intensity case.

5.4 PAK-B, Re_x = 100,000

The predicted and measured blade loading and skin friction for a Reynolds number of 100,000 are shown in Figure 5.7. For high turbulence intensity, the model predicts the onset of transition right at the point of boundary layer separation. For low turbulence, the model predicts a separation bubble. Both the blade loading and the hot-film results indicate the presence of a separation bubble at both turbulence intensities, with a noticeably longer bubble at the lower turbulence intensity.

The contours of turbulence intensity (Tu) and velocity for the high and low turbulence intensity cases are shown in Figures 5.8 and 5.9. Again, for both turbulence intensities the model predicts a laminar boundary layer on the pressure side of the blade with a cove separation bubble that does not cause transition. The cove separation bubble is noticeably smaller in the high turbulence intensity case. Presumably, this is because the higher turbulence quantities diffusing into the laminar boundary layer from the freestream have resulted in an increased effective viscosity. The increased viscosity in the laminar boundary layer helps to suppress the cove separation bubble. This effect was also observed in the ERCOFTAC T3A test case (see Chapter 4, Figure 4.4).

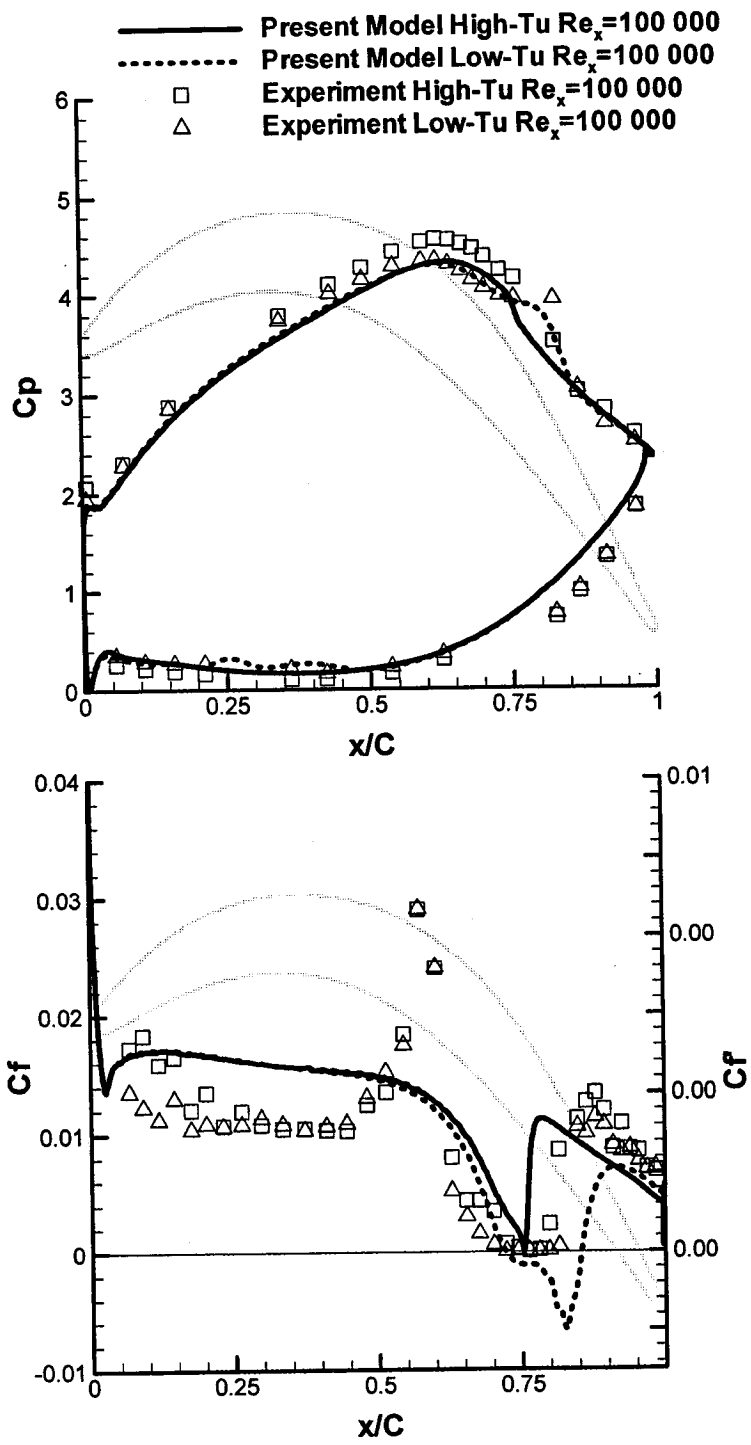

Figure 5.7 Predicted and experimental blade loading (Cp) and skin friction coefficient (Cf)/quasi-skin-friction coefficient (Cf') at an axial Reynolds number of 100,000.

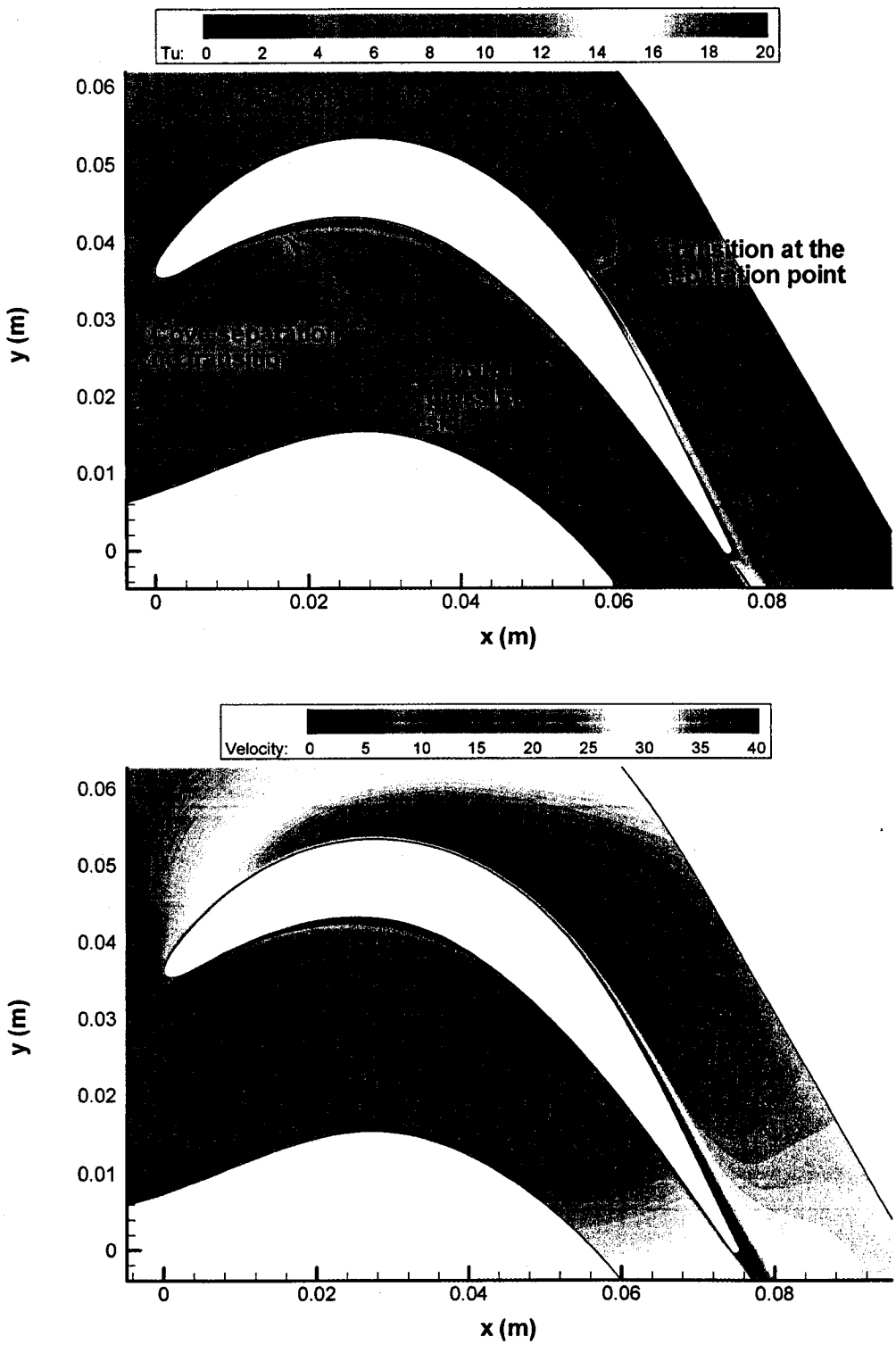

Figure 5.8 Contour plot of turbulence intensity (Tu, top) in percent and velocity (m/s, bottom) for the 100,000 axial Reynolds number, high turbulence intensity case.

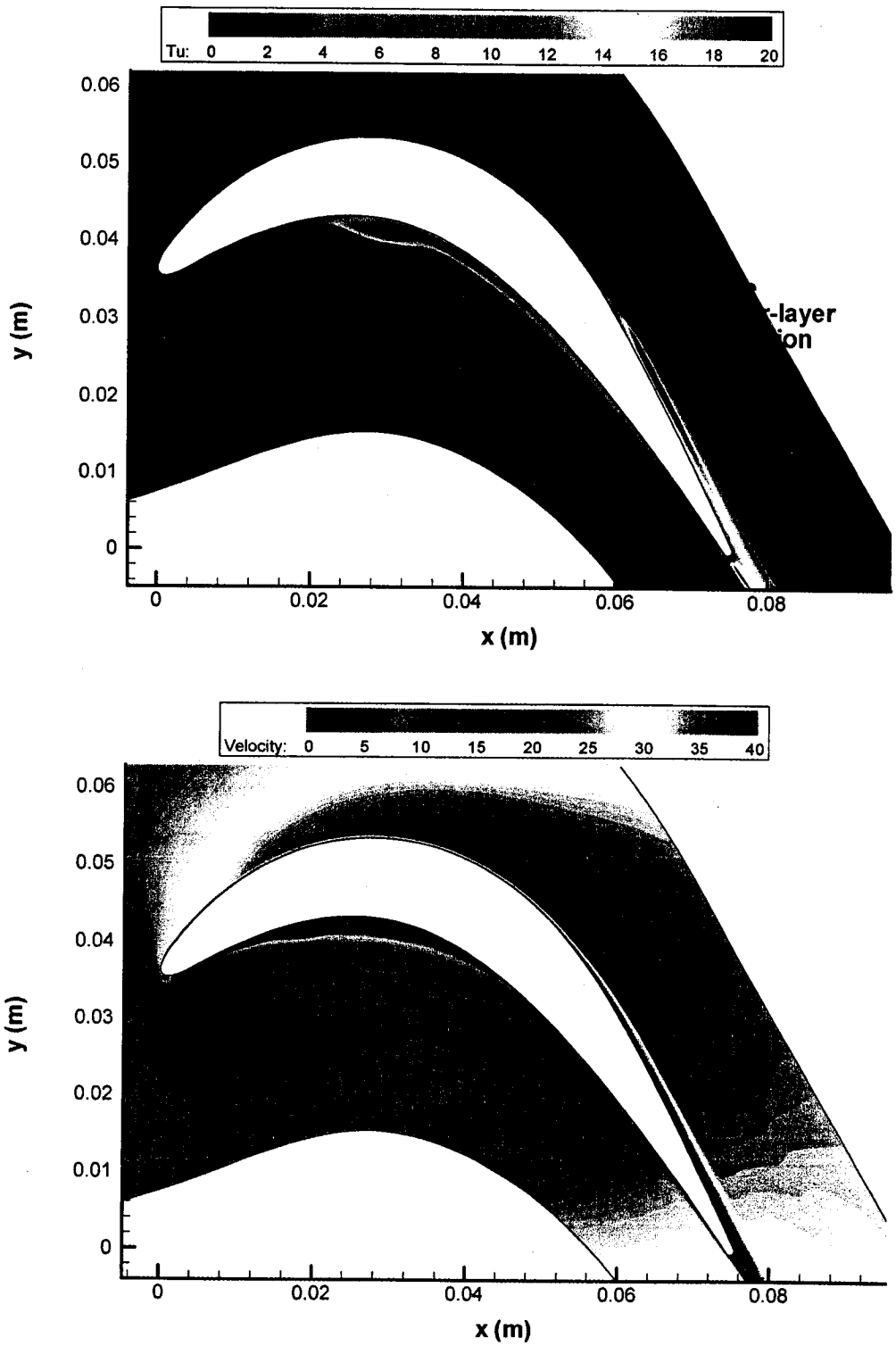

Figure 5.9 Contour plot of turbulence intensity (Tu, top) in percent and velocity (m/s, bottom) for the 100,000 axial Reynolds number, low turbulence intensity case.

5.5 PAK-B, $Re_x = 50{,}000$

The results for a Reynolds number of 50,000 are shown in Figure 5.10. For the high turbulence intensity case, the model predicts a bubble with a separation and reattachment point that is in excellent agreement with the experiment. For the low turbulence intensity case, the model predicts boundary layer reattachment right at the trailing edge of the blade. Based on the experimental blade loading and the hot film data, the separation bubble did not appear to reattach for the low turbulence level.

The contours of turbulence intensity (Tu) and velocity for the high and low turbulence intensity cases are shown in Figures 5.11 and 5.12. The cove separation in the high turbulence intensity case has now become quite large. A significant increase in k is observed and the boundary layer appears to be right on the verge of transition. However, before transition occurs the boundary layer reattaches and the large values of k slowly decay as the flow is accelerated towards the trailing edge. For the low turbulence intensity case, the cove separation is approximately the same size as the high turbulence intensity cases. There does not appear to be any noticeably increase in k and this is probably due to the fact that the freestream turbulence and local Reynolds numbers are too small.

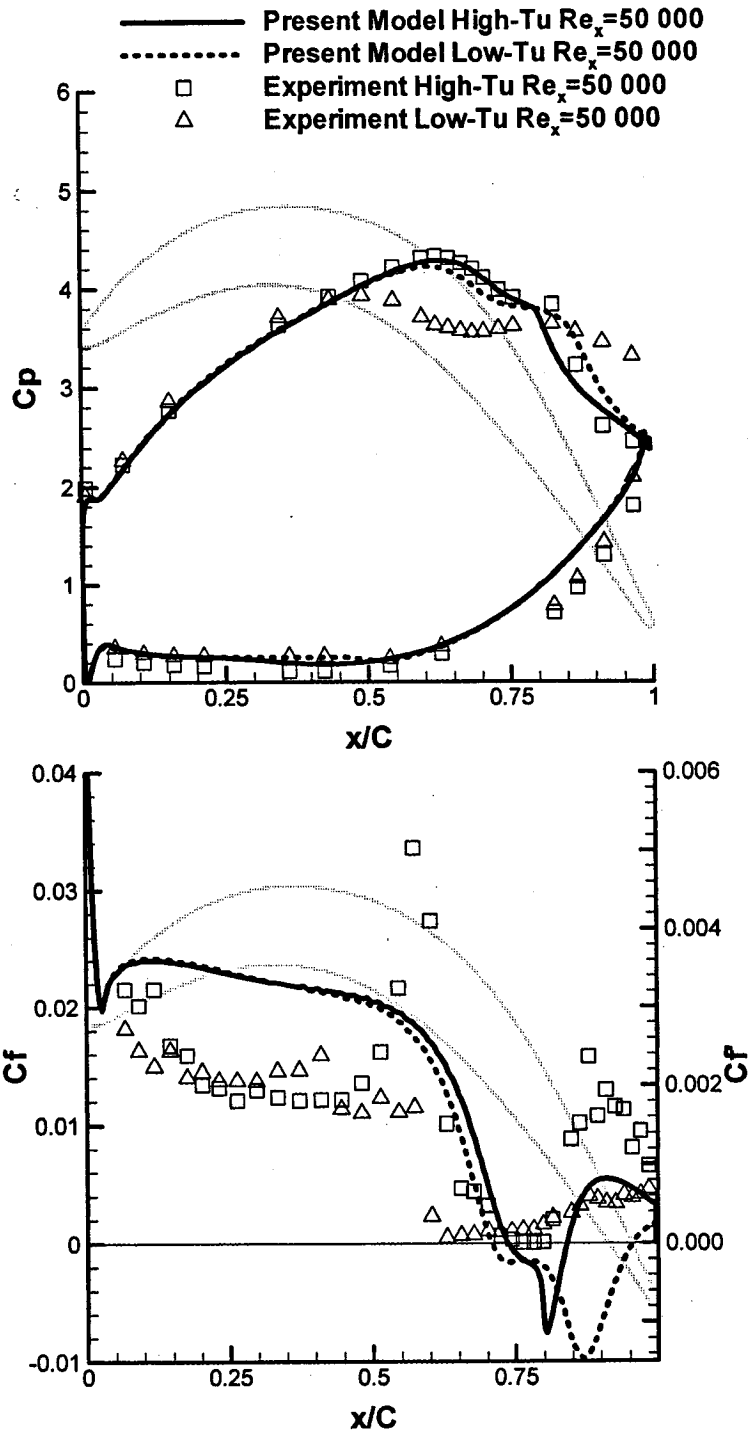

Figure 5.10 Predicted and experimental blade loading (Cp) and skin friction coefficient (Cf)/quasi-skin-friction coefficient (Cf') at an axial Reynolds number of 50,000.

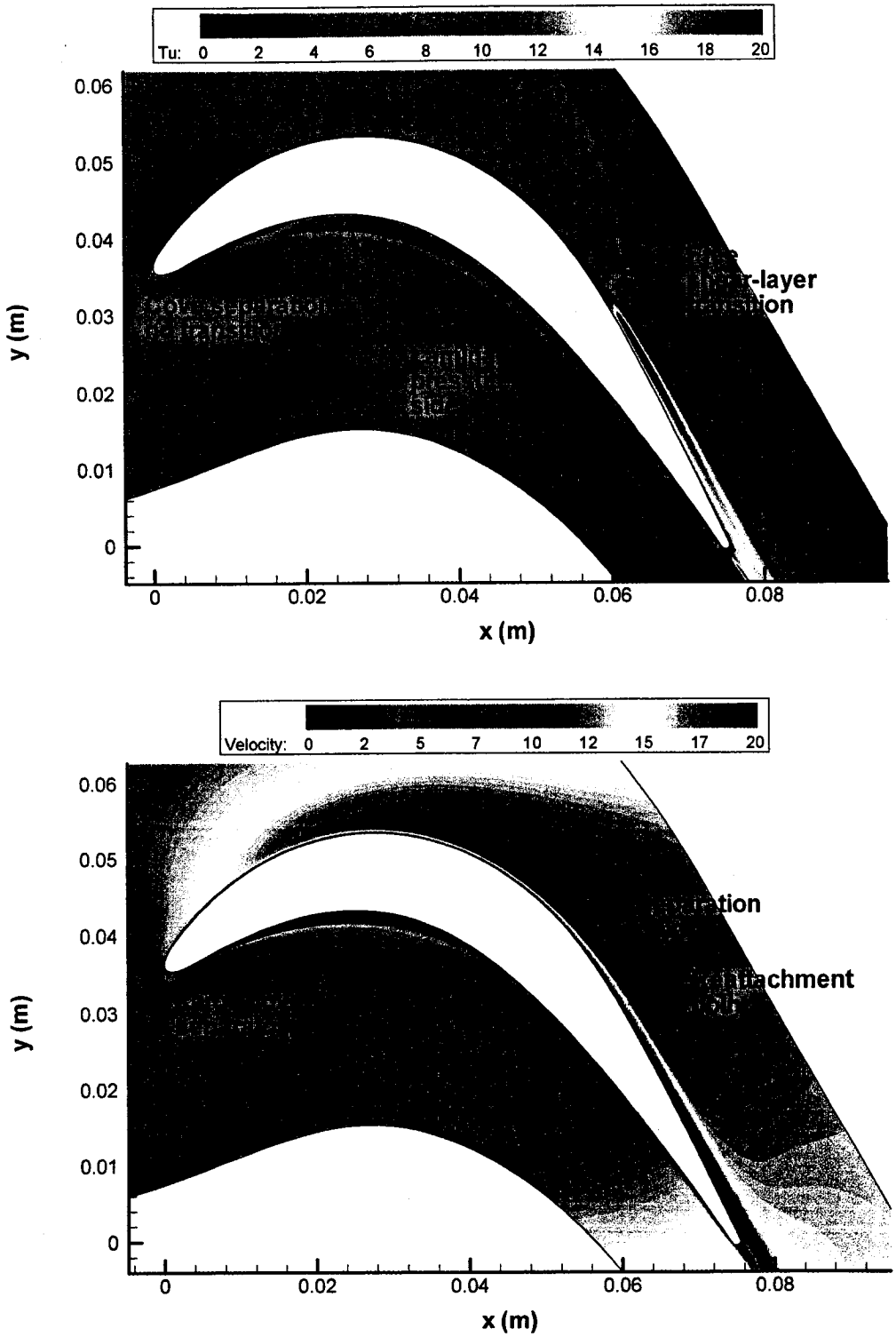

Figure 5.11 Contour plot of turbulence intensity (Tu, top) in percent and velocity (m/s, bottom) for the 50,000 axial Reynolds number, high turbulence intensity case.

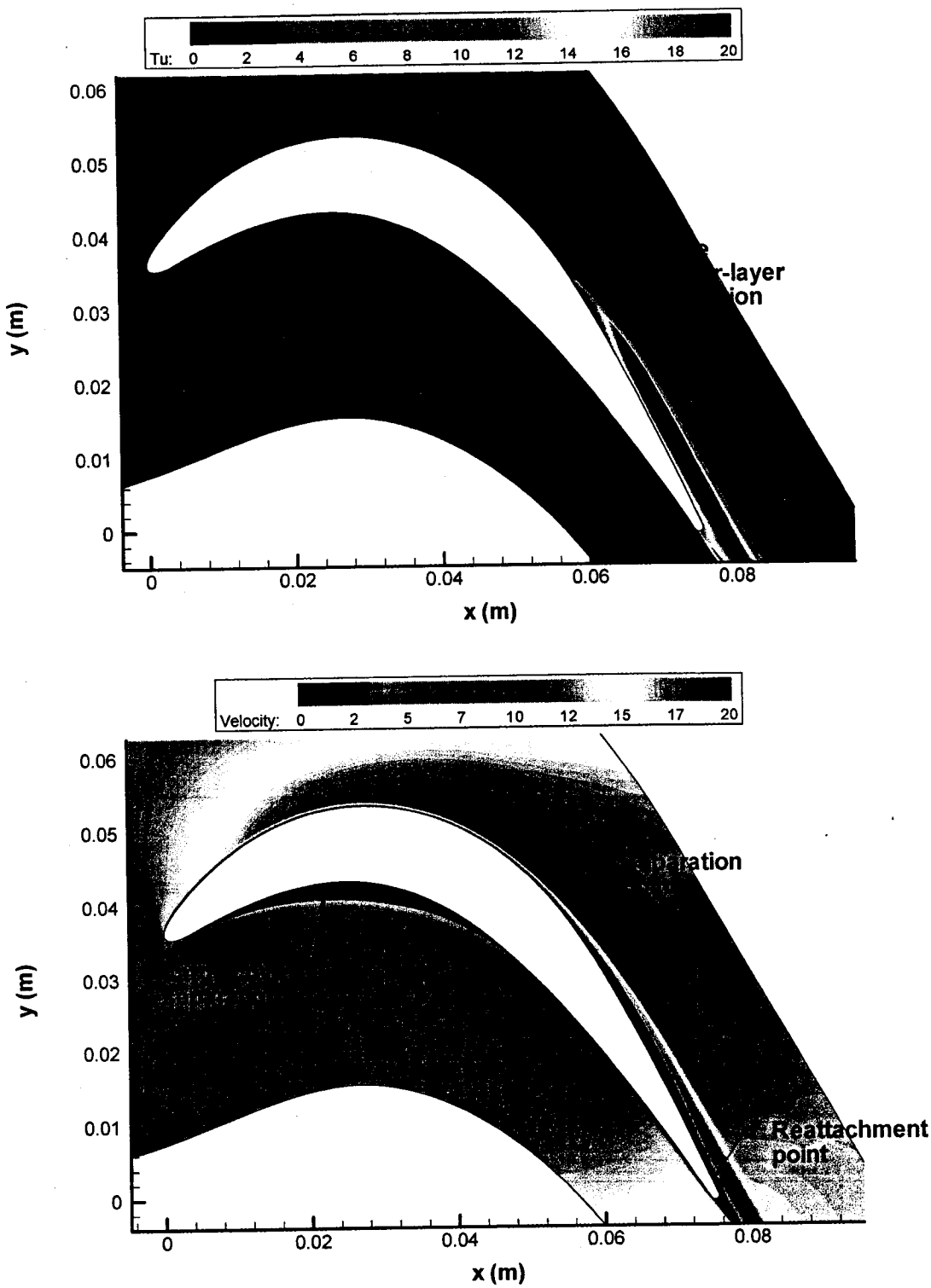

Figure 5.12 Contour plot of turbulence intensity (Tu, top) in percent and velocity (m/s, bottom) for the 50,000 axial Reynolds number, low turbulence intensity case.

5.6 PAK-B, $Re_x = 25{,}000$

For both the low and high turbulence intensity cases, a steady converged solution could not be obtained at a Reynolds number of 25,000. Experimentally, the flow again separated and failed to reattach at low turbulence intensity for this Reynolds number. Difficulty in obtaining steady converged solutions has been experienced by other researchers when the airfoil is massively stalled (Zheng et al, 1998). It is not clear whether this is the result of the inherently unsteady nature of the flow in question, or just a numerical problem. However, a steady solution was obtained for the high turbulence intensity case at Reynolds numbers of 35,000 and 30,000. The experimental and computational results for these Reynolds numbers and the measured results for 25,000, all at high turbulence intensity, are shown in Figure 5.13. At a Reynolds number of 35,000 the model predicts boundary layer reattachment right at the trailing edge of the blade. For a Reynolds number of 30,000 the model does not predict reattachment. Thus, the new transition model seems to be correctly indicating the range of Reynolds numbers for which the separation bubble may or may not reattach, depending on the level of freestream turbulence, for this airfoil.

The contours of turbulence intensity (Tu) and velocity for the 35,000 and 30,000 Reynolds number, high turbulence intensity cases are shown in Figures 5.14 and 5.15. For a Reynolds number of 35,000, the contour plots are almost identical to the low turbulence intensity case at a Reynolds number of 50,000. The only difference is that the growth of k in the cove separation is much larger due to the higher freestream turbulence level. For a Reynolds number of 30,000, the blade is completely stalled even though the onset of transition occurs shortly after the separation point. This would seem to suggest that the transitional length in the free shear layer is also an important factor in determining where the separation bubble will reattach, if at all.

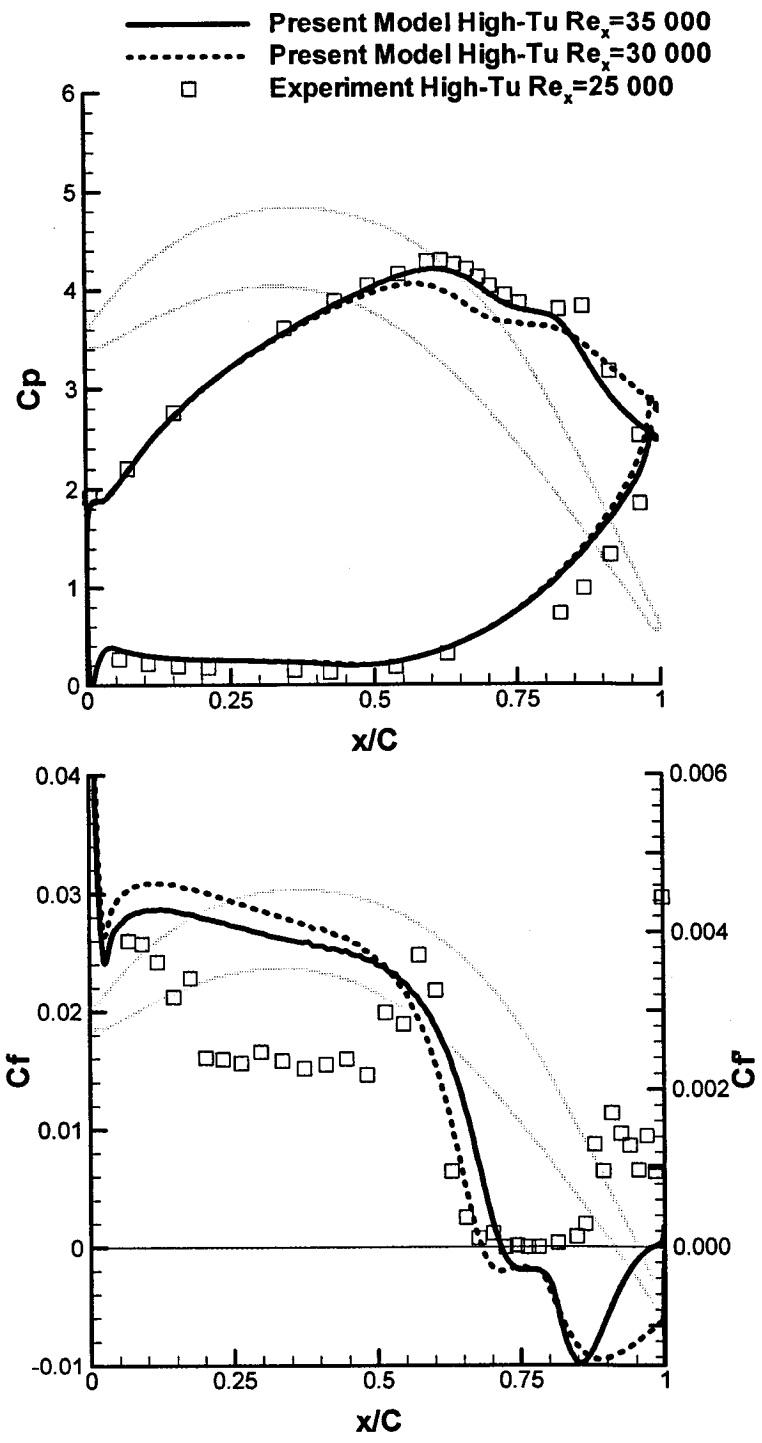

Figure 5.13 Predicted and experimental blade loading (Cp) and skin friction coefficient (Cf)/quasi-skin-friction coefficient (Cf') at an axial Reynolds number of 25,000.

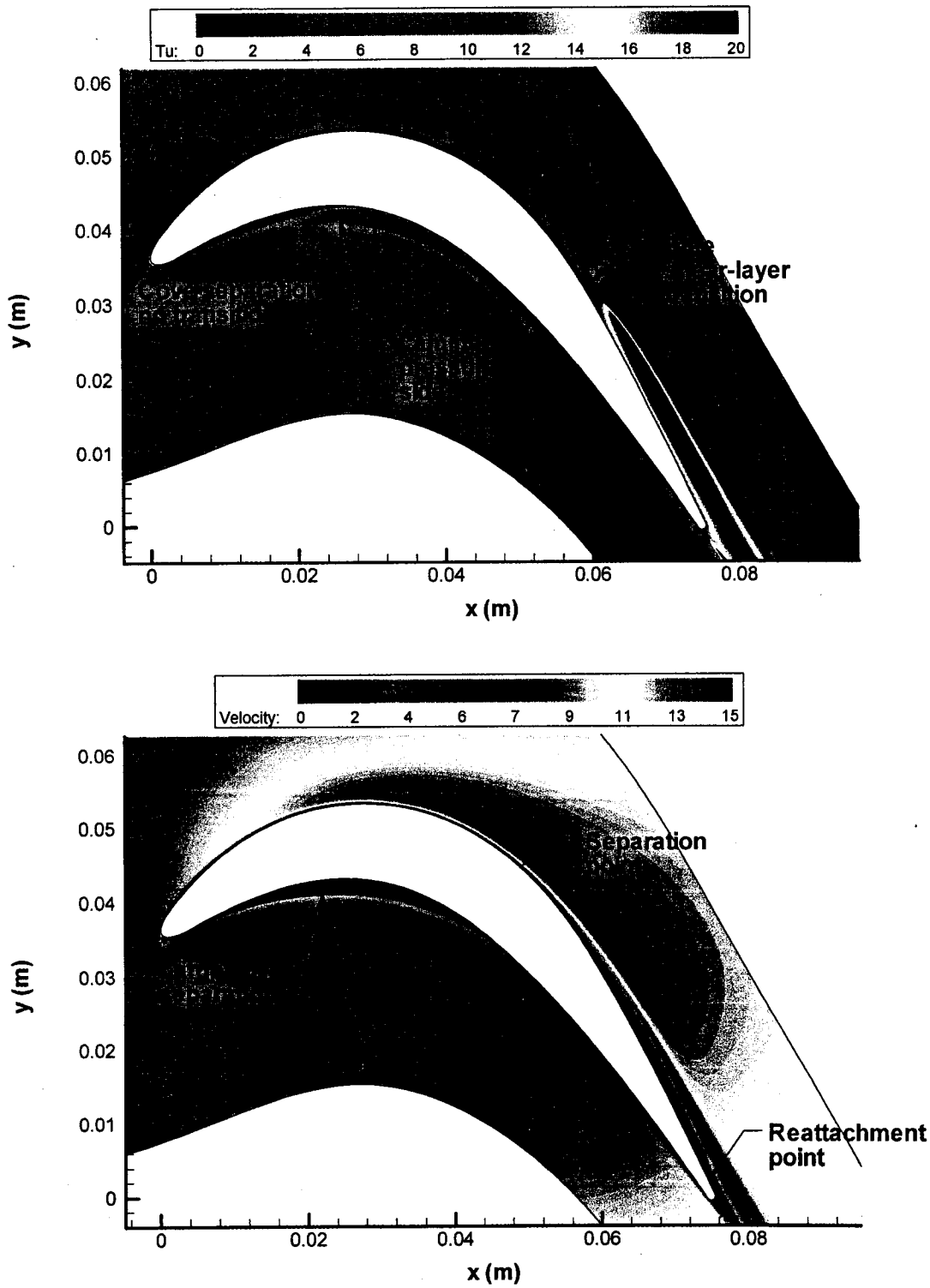

Figure 5.14 Contour plot of turbulence intensity (Tu, top) in percent and velocity (m/s, bottom) for the 35,000 axial Reynolds number, high turbulence intensity case.

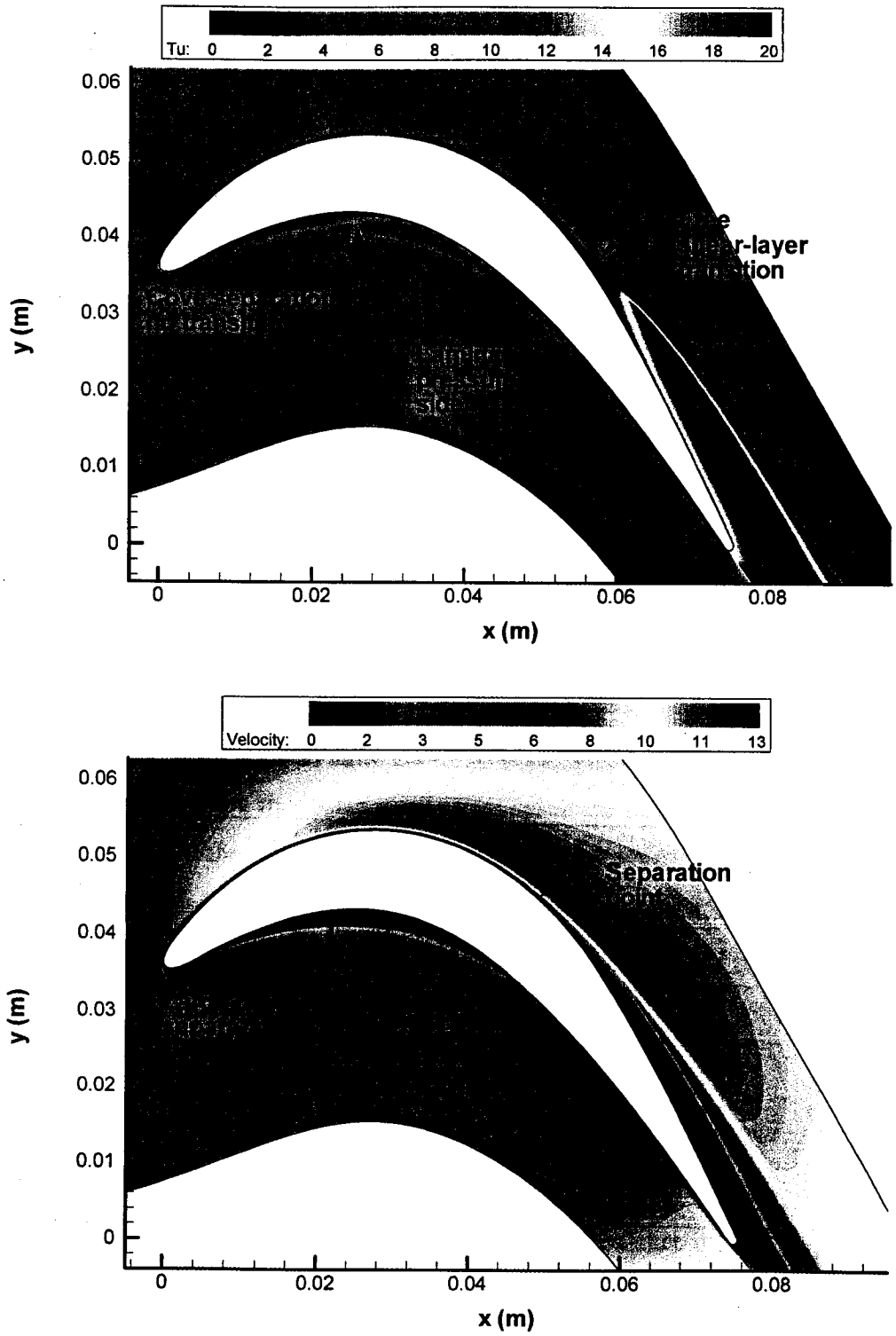

Figure 5.15 Contour plot of turbulence intensity (Tu, top) in percent and velocity (m/s, bottom) for the 30,000 axial Reynolds number, high turbulence intensity case.

5.7 Total Pressure Losses

The predicted losses from the PAK-B computations have been compared to the measured losses of Zhang et al (2002). The size of the separation bubble on the suction side of a turbine blade can have a significant effect on the profile losses (Mayle, 1991). Since the new transition model appeared to be predicting the separation and reattachment points on the PAK-B airfoil reasonably well, the computed losses should be in good agreement with the experiment. The loss coefficient (Y_p) is defined as follows:

$$Y_p = \frac{\overline{P}_{o1} - \overline{P}_{o2}}{P_{o2} - P_{s2}} \tag{5.1}$$

where $\overline{P_{o1}}$ and $\overline{P_{o2}}$ are the inlet and outlet mass-averaged total pressure and $\overline{P_{o1}} - \overline{P_{o2}}$ is the outlet mass-averaged dynamic pressure. The outlet pressures from the computations were defined at 50 percent of axial chord downstream of the blade trailing edge. This is the same location were the losses were measured in the experiment. Since the losses are being compared at the same location downstream of the blade there should be no need to calculate the mixed out losses. The mass-averaged pressures are defined as follows:

$$\overline{P} = \frac{\int P' d\dot{m}}{\int d\dot{m}} = \frac{\int_0^1 P' V_{axial} d(y/s)}{\int_0^1 V_{axial} d(y/s)} \tag{5.2}$$

The computed and measured losses for the high turbulence intensity cases are shown in Figure 5.16. The results from a fully turbulent computation using the Spalart-Allmaras turbulence model are also shown. The losses for the transitional and fully turbulent computation are almost identical for Reynolds numbers greater than 150 000. This is because the transition has occurred upstream of where the laminar boundary layer would have separated. The present transition model appears to predict reasonably well the

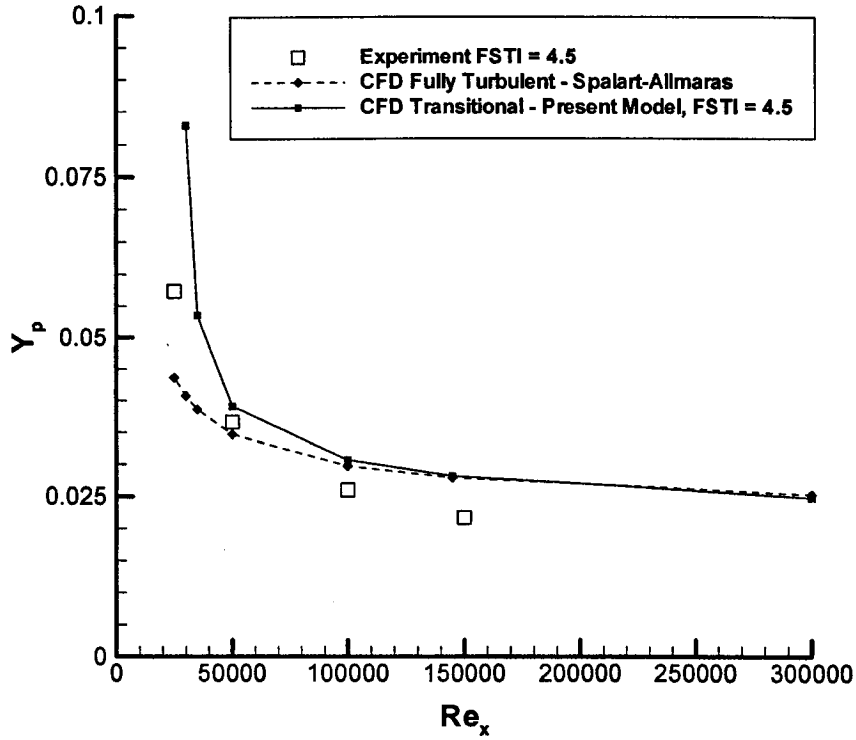

Figure 5.16 Total pressure losses (Y_p) vs. axial Reynolds number (Re_x) for the high turbulence intensity cases.

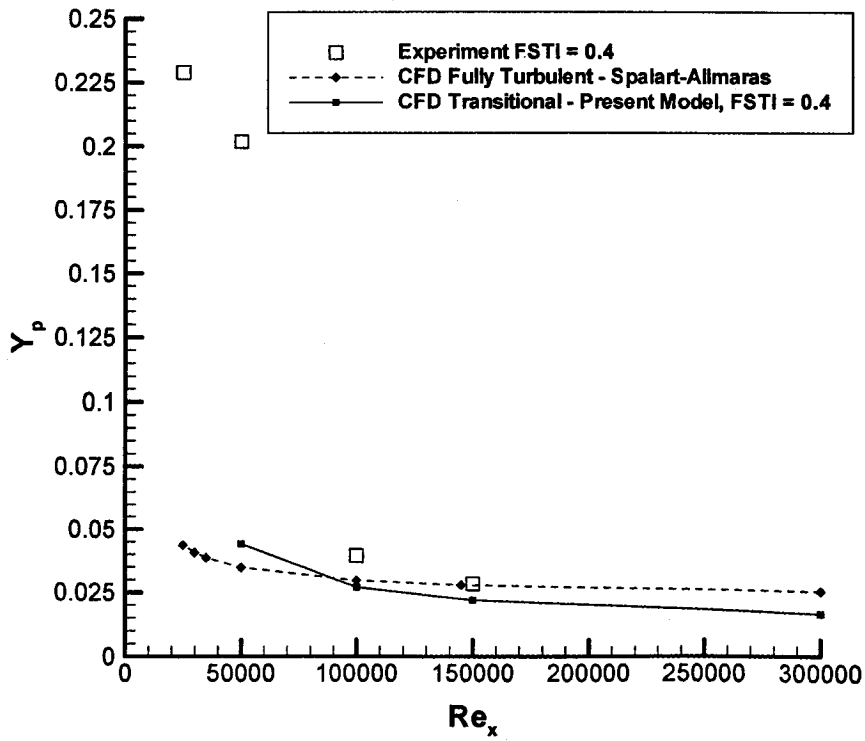

Figure 5.17 Total pressure losses (Y_p) vs. axial Reynolds number (Re_x) for the low turbulence intensity cases.

experimental Reynolds number where the losses start to climb dramatically due to blade stall.

The computed and measured losses for the low turbulence intensity cases are shown in Figure 5.17. At a Reynolds number slightly less then 50,000 (i.e. 45 000) the present transition model predicted blade stall. Unfortunately, a steady converged solution could not be obtained. If a converged solution could have been obtained one would expect the losses to be quite high (0.1 or higher). In light of this, the agreement with the trend in measured losses is fairly good.

At these very low Reynolds numbers, the reattachment or otherwise of the separation bubble is strongly a function of the location of transition in the free shear layer at the outer edge of the bubble. The new transition model did indeed predict that transition would occur in this free shear layer (see Figure 5.14). The fact that the reattachment of the bubble, or its failure to do so, was in quite good agreement between the measurements and the predictions, suggests the new model is predicting the location of transition in the free shear layer reasonably well. This apparent success of the model in predicting transition in the free shear layer of separation bubbles is surprising, especially considering the simplicity of the model and the fact that no empirical information about separation bubbles has been used to calibrate it. Through the vorticity Reynolds number, the prediction of transition is always influenced by the distance to the nearest wall. The success of the new model suggests that the dynamics of blade-surface separation bubbles is still influenced by their proximity to the wall. However, the model is almost certainly not applicable for the prediction of transition in general free shear layers that are not influenced by any adjacent walls.

Chapter 6
Pak-B Unsteady

6.1 Introduction

In the previous chapters the new transition model was shown to predict reasonably well transition in steady attached and separated flows. However, in gas turbine engines the mean flow is not steady. It is now believed that transition on actual engine blades is strongly influenced by the unsteady wakes from the upstream blade rows. There is a growing body of experimental evidence that suggests that the unsteady wakes can have a profound impact on the suction side separation bubbles and hence the losses of low pressure turbine blades (e.g. Howell et al, 2001). For this reason, in order to improve efficiency, turbomachinery designers will eventually need to be able to investigate both the steady and unsteady behavior of their blade designs. This chapter will therefore attempt to validate the new transition model for the prediction of unsteady wake induced transition on a low pressure turbine blade.

Zhang (2002) has measured the quasi-wall-shear stress (using surface-mounted hot films) for the PAK-B airfoil subjected to unsteady impinging wakes. The experiments where performed for a freestream turbulence intensity of 0.4 percent and for Reynolds numbers, based on axial chord and inlet velocity, of 100,000 and 25,000. The wake was produced by a cylindrical spoke attached to a rotating wheel if front of the blade cascade. In the experiment the number of spokes and the rotation speed of the wheel was varied to produce the correct flow coefficient and spoke passing frequency. The wake passing frequency from the spoke was chosen to be representative of that in an actual gas turbine engine. Zhang's (2002) experiment has been simulated using the new transition model

and the results are detailed in sections 6.3 and 6.4. The next section will discuss the choice of unsteady parameters and the mesh that was used in both computations.

6.2 Problem Geometry and Mesh Definition

The grid used for all the unsteady computations is shown if Figure 6.1. It is identical to the grid used for the steady computations except for the addition of the spoke in front of the blade. The spoke had a diameter of 1.58 mm. The mesh around the spoke was an O-grid with the first cell wall distance specified so that the y^+ of 1.0 or less was present at all times.

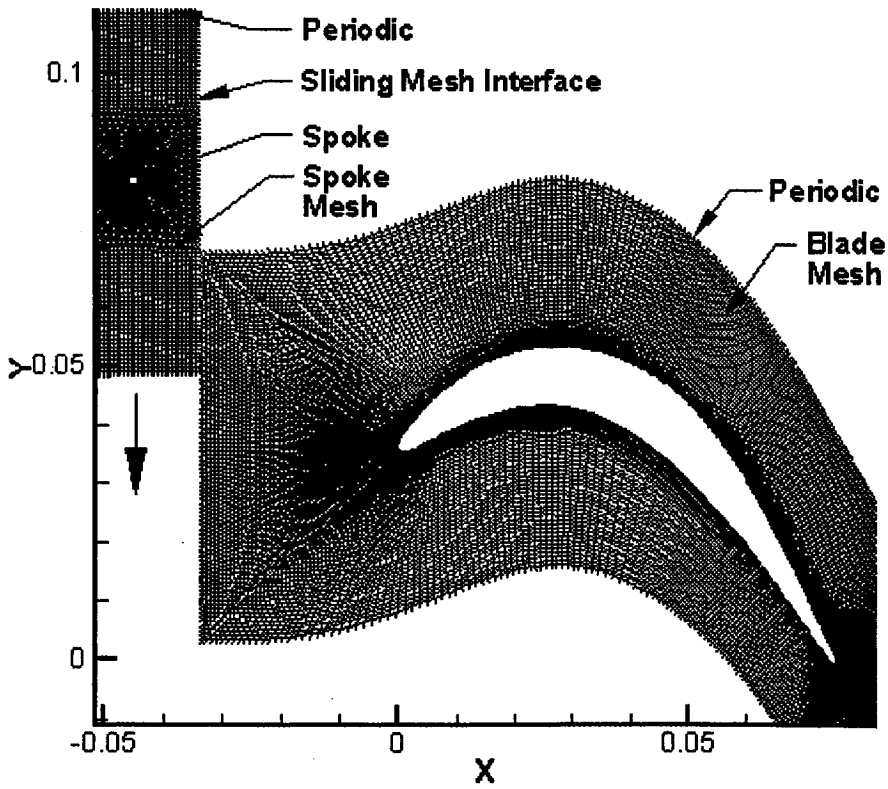

Figure 6.1 PAK-B mesh used for all unsteady computations

Since the spoke is moving relative to the blade a sliding mesh interface is used in between the spoke grid and the blade grid. The purpose of the sliding mesh interface is to

interpolate the solution from one mesh to the other during each time step. The translation speed of the spoke mesh was determined from the experimental reduced frequency of 1.52 that was used in Zhang's (2002) experiment. The reduced frequency (f) is calculated from the following formula (Zhang, 2002):

$$f = \frac{B_x U_{bar}}{V_{ax} S_{bar}} \tag{6.1}$$

where B_x is the blade axial chord, U_{bar} is the spoke speed, V_{ax} is the axial velocity and S_{bar} is the spoke spacing. It should be noted that the spoke spacing used in the computation was slightly different from the spacing in the experiment. Due to the periodic boundary condition in the computations the spoke spacing must be some fraction of the blade spacing. The spoke spacing in the experiment was 70.65 mm whereas the spacing in the computations was 66.80 mm. Because of this the spoke speed (U_{bar}) in the computations was adjusted so that the reduced frequency was the same as that of the experiment. The unsteady time step in the solver was selected so that there would be one hundred time steps per wake passing period.

Another important difference between the experiment and the computations was the choice of freestream turbulence intensity. Zhang (2002) performed both of his unsteady experiments with a freestream turbulence intensity of 0.4 percent. This was done in order to investigate the effect of the unsteady wakes on a blade that had a separation bubble (Re_x = 100,000) and a blade that was completely stalled (Re_x = 25,000). In the case of the computations a steady converged solution could not be obtained for a Reynolds number of 25,000 due to the large separation bubble present. However, a steady converged solution for a stalled blade was obtained for a freestream turbulence level of 4.5 percent and a Reynolds number of 30,000. Since we are primarily interested in comparing the differences between the steady and unsteady solutions it was decided to run the unsteady computations with a freestream turbulence level of 4.5 percent at a Reynolds number of 100,000 and 30,000. The next section will discuss the results obtained for these two Reynolds numbers.

6.3 High Reynolds Number Case

The unsteady measured and predicted quasi-wall shear stress / skin friction for a Reynolds number of 100,000 are presented as Space-Time (S-T) diagrams in Figure 6.2. In both the experiment and the computation the local values are normalized by the maximum value over time at the same chord wise position. Zhang (2002) used this form of presentation in order to emphasize the periodic change in the mean values.

Both the experimental and numerical S-T diagrams are very similar. Near the leading edge of the blade the wake passing does not have pronounced effect on the wall shear stress. After about 20 percent chord distance the effect of the wake on the wall shear becomes significant. The boundary layer at this point is still laminar and the change in wall shear is completely due to the momentum deficit of the wake. The wake induced transition can be seen to occur shortly after the boundary layer separates. Similar to the experiment, the regions of low shear which have large losses are still present but only for about 30 percent of the time. The net effect is that the time average losses are probably being reduced because the fraction of time the boundary layer is close to separating is diminished.

The steady, minimum, maximum and time averaged skin friction is shown in figure 6.3. From the minimum and maximum values it is clear that there are vary large variations in the skin friction due to the unsteady wakes. However, when time averaged, the skin friction is remarkable similar to the steady value. For this reason, turbomachinery blade design based on steady conditions would appear to be a very reasonable assumption. The only location where the steady skin friction deviates significantly from the time average is in the region where the boundary layer is close to separating. In this region the time average skin friction is higher than the steady value. This means that there is probably some additional room to increase the blade loading before the time averaged boundary layer will separate.

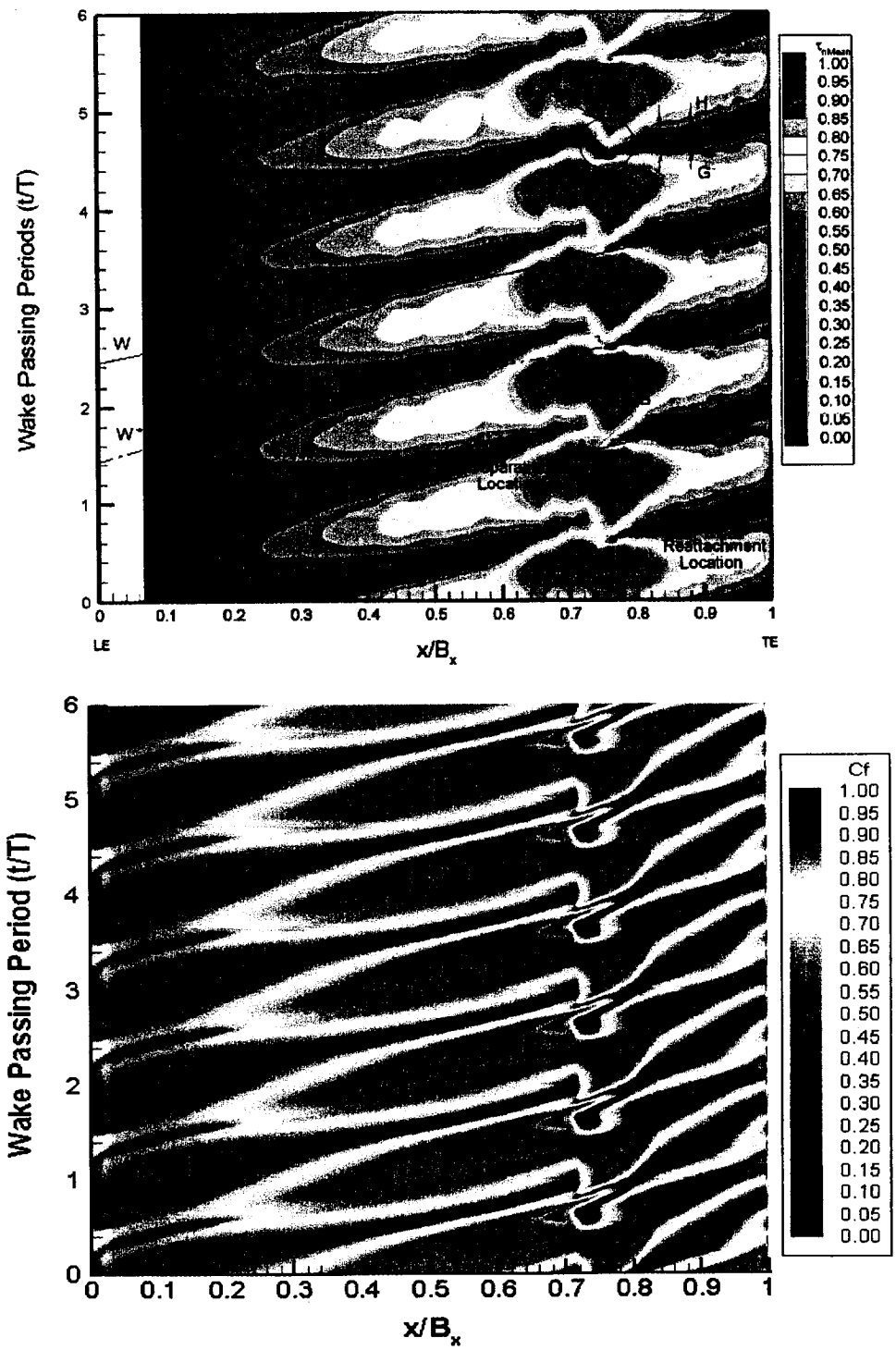

Figure 6.2 S-T diagram of experimental quasi-wall shear stress (top) and computed skin friction (bottom) at a Reynolds number of 100,000 (experimental S-T diagram reproduced from Zhang, 2002).

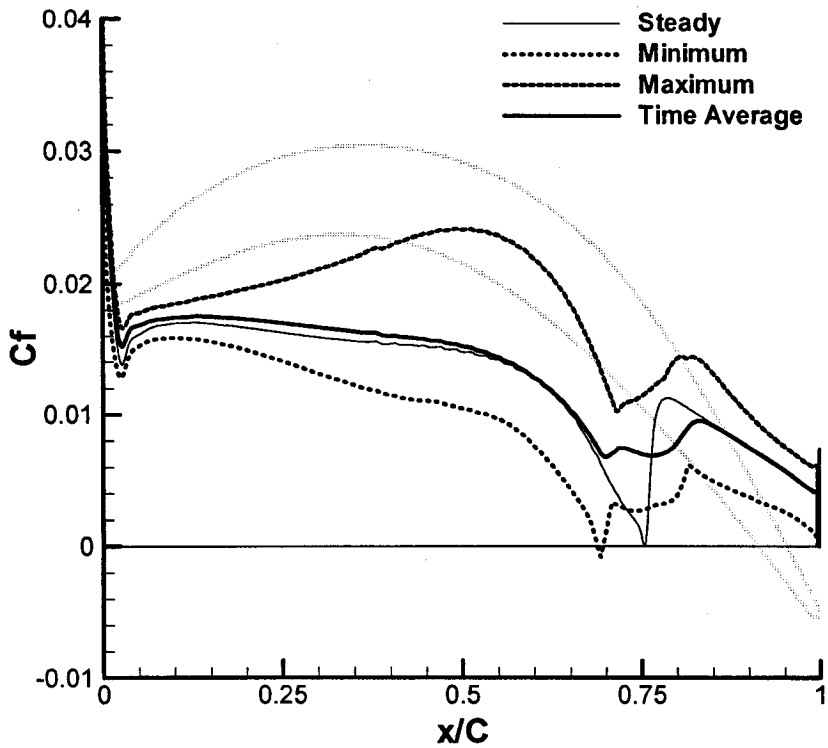

Figure 6.3 Steady, minimum, maximum and time averaged skin friction for a Reynolds number of 100,000.

The skin friction at three different points in time is shown in Figure 6.4. There were 100 time steps per spoke passing period in the computation. The results shown in Figure 6.4 are for the 25th, 50th and 75th time step. At any one time the skin friction is quite different from the steady value. One of the most striking features is how much the laminar boundary layer was distorted by the passing wake. As well, the start of wake induced transition can be clearly observed. As the turbulent region passes and the boundary layer reverts back to laminar flow the so-called calmed region is clearly visible. The calmed region is most likely responsible for the differences between the steady and time averaged skin friction. This is because it has a much fuller velocity profile and can withstand larger adverse pressure gradients before separating.

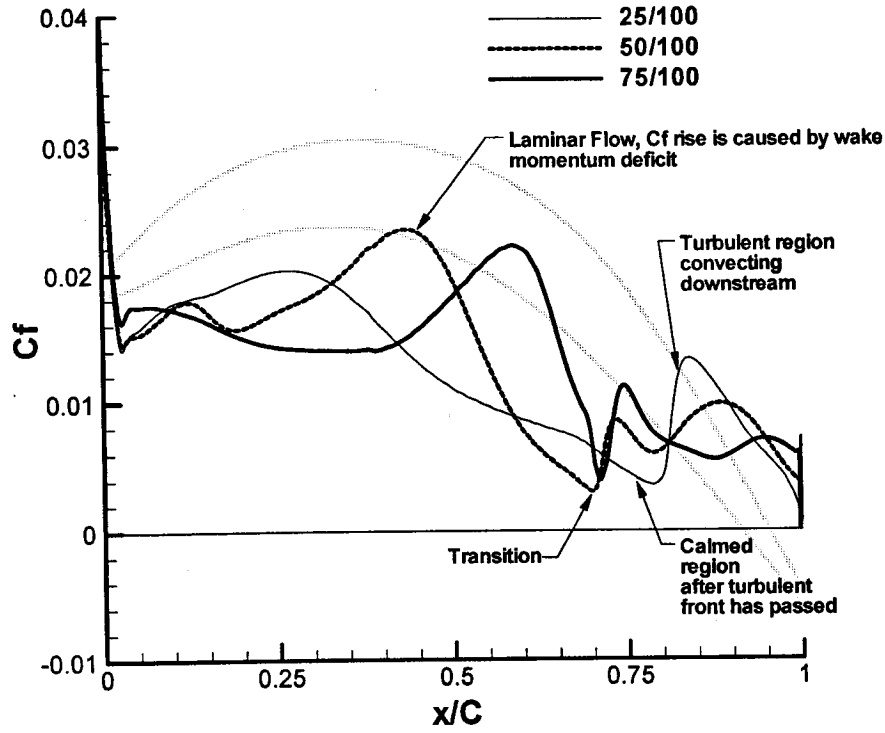

Figure 6.4 Skin friction at three different points in time for a Reynolds number of 100,000.

6.4 Low Reynolds Number Case

The unsteady measured and predicted quasi-wall shear stresses / skin friction for a Reynolds number of 25,000 / 30,000 are presented as Space-Time (S-T) diagrams in Figure 6.5. Again, the predicted and computed results are in very good agreement. A large open separation bubble was present in the steady results. When subjected to the unsteady wake the transition does appear to occur right at the separation point. However, the subsequent turbulent region is far more complicated than the higher Reynolds number case. There appears to be regions of attached turbulent flow separated by rolls of strongly recirculating flow that are convecting down the trailing edge. This is best illustrated by the S-T diagram in Figure 6.6 where the actual skin friction instead of the absolute value is shown. The results were again normalized by the maximum value at each chord wise position.

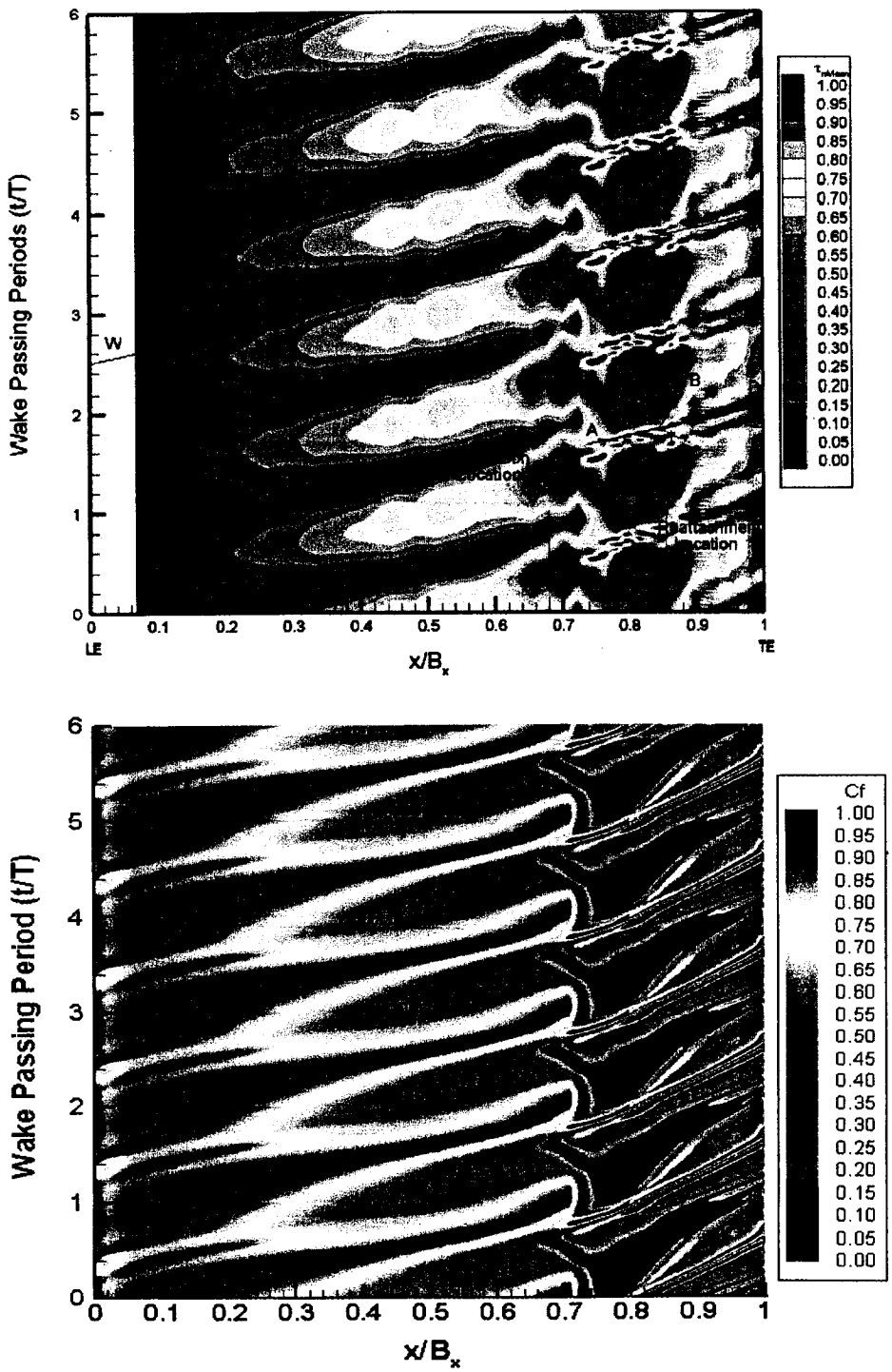

Figure 6.5 S-T diagram of experimental quasi-wall shear stress (top) and computed skin friction (bottom) at a Reynolds number of 25,000 / 30,000 (experimental S-T diagram reproduced from Zhang, 2002).

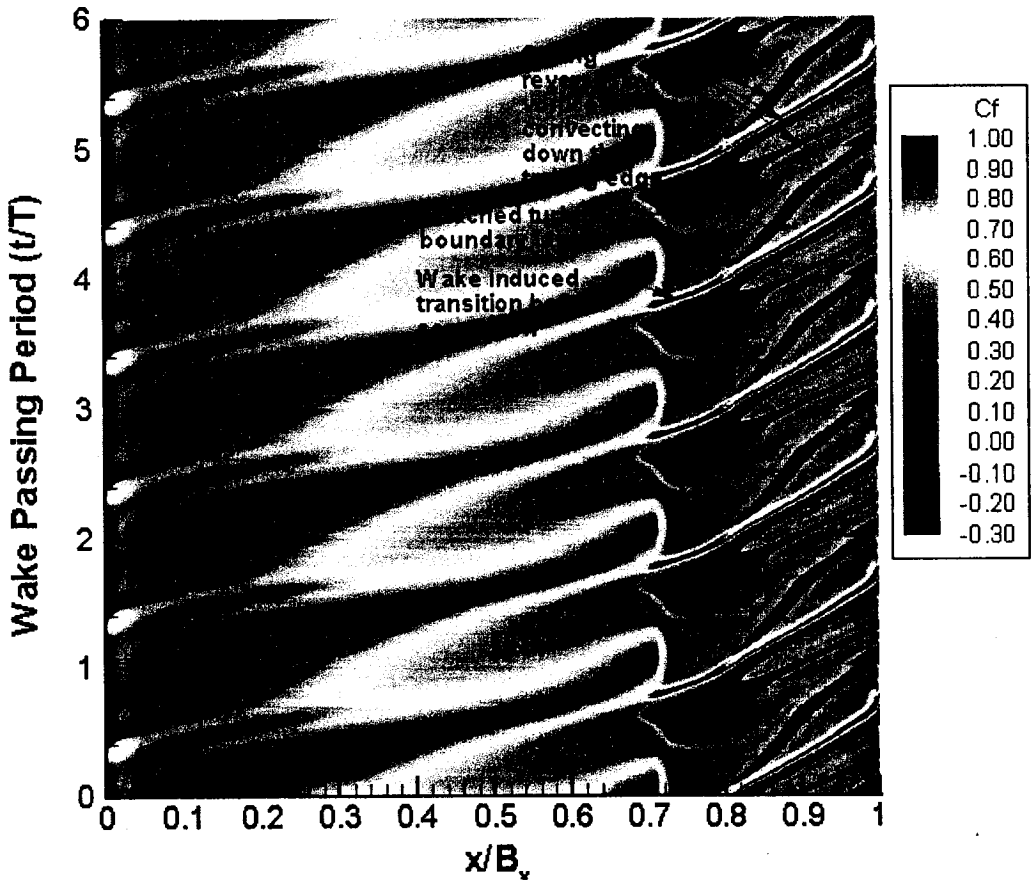

Figure 6.6 S-T diagram of actual computed skin friction at a Reynolds number of 25,000 / 30,000.

The strong reverse flow vortices have been observed before in the DNS computations performed by Wissink (2002). The geometry in Wissink's computation was very similar to Zhang's (2002) experiment. Since the hot film results from Zhang (2002) could only measure the absolute value of shear stress it is quite possible that the vortices where present but not detected.

The steady, minimum, maximum and time averaged skin friction is shown in Figure 6.7. Again, from the minimum and maximum values it is clear that there are vary large variations in the skin friction due to the unsteady wakes. For the steady flow the

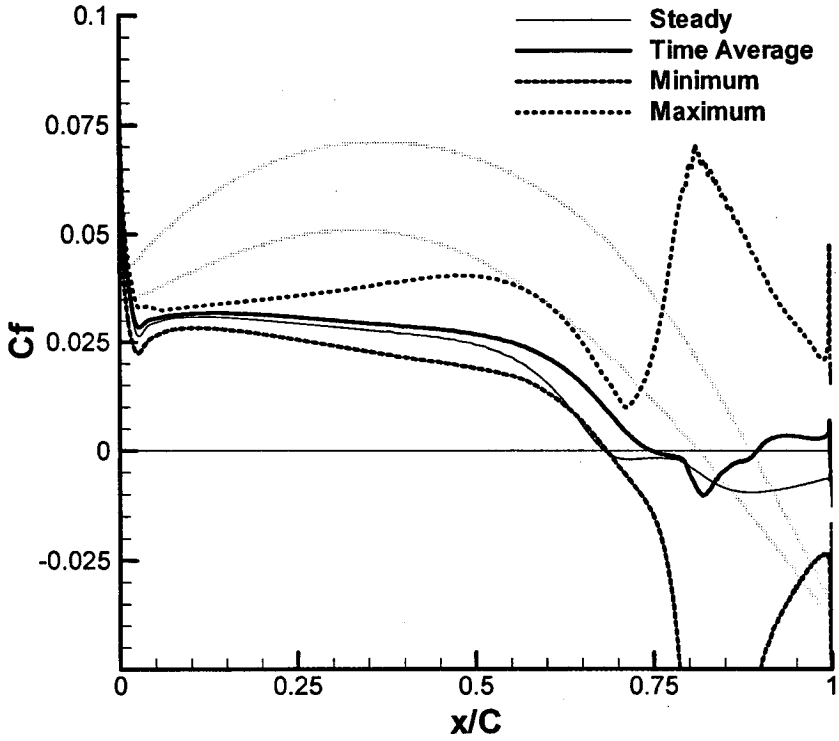

Figure 6.7 Steady, minimum, maximum and time averaged skin friction for a Reynolds number of 30,000.

boundary layer separated and did not reattach. However, when subjected to unsteady wakes the time averaged boundary layer does in fact reattach.

The skin friction at two different points in time is shown in Figure 6.8. The unsteady flow field is quite complicated. There appears to be a series of counter rotating vortices that are convecting down to the trailing edge. Of particular note is that the vortices have very high levels of shear that will result in very large losses. It is quite possible that in this case the unsteady wakes may actually be increasing the losses even though the time averaged boundary layer appeared to reattach.

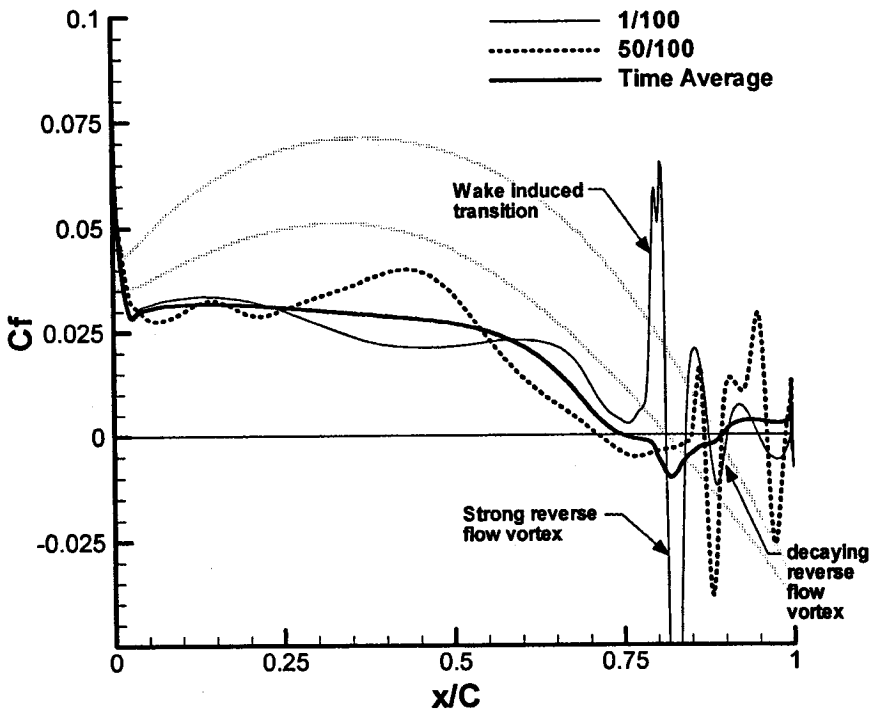

Figure 6.8 Skin friction at two different points in time for a Reynolds number of 30,000.

This concludes the validation of the new transition for the prediction of unsteady wake induced transition. The new model appears to be in very good qualitative agreement with the experiment of Zhang (2002). This came as quite a surprise because unsteady wake induced transition is an extremely complicated phenomenon. The fact that the simple transition model developed in this thesis was able to capture the most important features of these types of flows was very encouraging.

Chapter 7
Conclusions and Recommendations

A new transition model has been developed for modeling transition under the influence of freestream turbulence intensity, pressure gradients and flow separation. The new model is based on Van Driest and Blumer's (1963) concept of the vorticity Reynolds number. Since the vorticity Reynolds number is a local parameter it avoids the need to integrate boundary layer quantities such as momentum thickness Reynolds number in order to prediction the onset of transition. As a result, the model can be used with unstructured Navier-Stokes codes. The model has been calibrated empirically for use with the Menter (1994) SST model, which is a popular and robust two-equation turbulence model.

The new transition model has been validated against the T3 series (Savill, 1993a,b) of experimental test cases. In general, good agreement was obtained and the model appears to be as accurate at predicting the onset location of transition as the available empirical correlations.

The new transition model has also been validated against the steady and unsteady experiments performed by Zhang et al. (2002) for the PAK-B low-pressure turbine airfoil. In all cases the agreement with experiment was good. Of particular note was the ability of the model to predict the combined effect of freestream turbulence intensity and Reynolds number on the reattachment point of a separation bubble. With no empirical information about separation bubbles, the model appeared able to predict the blade-chord Reynolds number for which a transitional separation bubble fails to reattach to within about 10,000. From the unsteady results the model appears to have the proper sensitivity to the effect of unsteady impinging wakes on the transitional boundary layer development. Notably, the model was able to predict the early wake induced transition

and the subsequent calmed flow after the turbulent region had passed. Based on the encouraging results obtained so far, it would appear that the new transition model could be a very useful tool for the design of highly-loaded and efficient turbomachinery.

One significant drawback of the new transition model is that it is not Galilean invariant. This is because the pressure gradient term in equation 3.33 is based on the local velocity and the pressure gradient along the local streamline. Thus, if the reference frame is not stationary (as is the case for moving grids or rotating reference frames often used to simulate centrifugal machinery) than obviously equation 3.33 will not be representative of the actual pressure gradient encountered by the boundary layer. The error can be minimized by defining the local velocity and streamline direction in terms of the relative velocity. Nevertheless, Galilean invariance is an important criteria for general turbulence models and future work on this transition model should therefore focus on improving this aspect of the model.

Another important area of transition that has not been addressed in this thesis is relaminarization. This phenomena is generally believed to occur when the acceleration parameter (K) exceeds $3x10^{-6}$ (Mayle, 1991). Such accelerations are not uncommon on the pressure side of most high-pressure turbines. Due to time constraints no attempt has been made to validate the present transition model for the prediction of relaminarization. Future attempts to validate the new transition model should therefore include an investigation into how well the model predicts this phenomenon.

References

Abu-Ghannam, B.J. and Shaw, R., 1980, "Natural Transition of Boundary Layers-The Effects of Turbulence, Pressure Gradient, and Flow History," *Journal of Mechanical Engineering Science*, Vol. 22, No. 5, pp. 213 – 228.

Bardina, J.E., Huang, P.G. and Coakley, T.J., 1997, "Turbulence Modeling Validation, Testing, and Development," *Nasa Technical Memorandum 110446*, Ames Research Center, Ca.

Biswas, D. and Fukuyama, Y., 1994, "Calculation of Transitional Boundary Layers With an Improved Low-Reynolds-Number Version of the k-ε Turbulence Model," *Journal of Turbomachinery*, Vol. 116, pp. 765-773.

Cooke, P.E, McDonald, M. and Firmin, M., 1979, "Airfoil RAE2822-Pressure Distributions and Boundary Layer Wake Measurements," AGARD AR-138.

Driver, D.M., 1991, "Reynolds Shear Stress Measurements in a Separated Boundary Layer," AIAA Paper AIAA-91-1787.

Dorney, D.J., Lake, J.P., King, P.L. and Ashpis, D.E., 2000, "Experimental and Numerical Investigation of Losses in Low-Pressure Turbine Blade Rows," AIAA Paper AIAA-2000-0737, Reno, NV.

Durbin, P.A., Jacobs, R.G. and Wu, X., 2002, "DNS of Bypass Transition," *Closure Strategies for Turbulent and Transitional Flows*, edited by B.E. Launder and N.D. Sandsam, Cambridge University press, pp. 449-463.

Fashifar, A. and Johnson, M. W., 1992, "An Improved Boundary Layer Transition Correlation", ASME Paper ASME-92-GT-245.

FLUENT 5 User's Guide (1998), Fluent Inc., Lebanon, NH, US.

Garg, V.K. and Ameri, A.A., 2001, "Two-Equation Turbulence Models for Prediction of Heat Transfer on a Transonic Turbine Blade," ASME Paper 2001-GT-0165.

Gehrer, A., Lang, H., Mayrhofer, N. and Woisetschläger, J. 2000, "Numerical and Experimental Investigation of Trailing Edge Vortex Shedding Downstream of a Linear Turbine Cascade," ASME Paper 2000-GT-0434.

Hellsten, A. and Laine, S., 1998, "Extension of k-ω Shear-Stress Transport Turbulence Model for Rough-Wall Flows," *AIAA Journal*, Vol. 36, No. 9, pp. 1728-1729.

Howell, R.J., Ramesh, O.N., Hodson, H.P., Harvey, N.W. and Schulte, V., 2001, "High Lift and Aft-Loaded Profiles for Low-Pressure Turbines," *Journal of Turbomachinery*, Vol. 123, pp. 181-188.

Johnson, D.A. and King, L.S., 1985, "Mathematically Simple Turbulence Closure Model for Attached and Separated Turbulent Boundary Layers," *AIAA Journal*, Vol. 23, No.11, pp. 1684-1692.

Johnson, M.W., 1994, "A Bypass Transition Model for Boundary Layers," *Journal of Turbomachinery*, Vol. 116, pp. 759-764.

Jones, W. P., and Launder, B. E., 1973, "The Calculation of Low Reynolds Number Phenomena with a Two-Equation Model of Turbulence," *Int. J. Heat Mass Transfer*, Vol. 15, pp. 301-314.

Kato, M. and Launder, B.E., 1993, "The Modelling of Turbulent Flow Around Stationary and Vibrating Square Cylinders," Proc. 9th Symp. Turbulent Shear Flows, Kyoto, Japan, 10-4-1.

Klebanoff, P.S. and Tidstrom, K.D., 1959, "Evolution of amplified waves leading to transition in a boundary layer with zero pressure gradient," NASA TN D-195.

Mayle, R.E., 1991, "The Role of Laminar-Turbulent Transition in Gas Turbine Engines," *Journal of Turbomachinery*, Vol. 113, pp. 509-537.

Mayle, R.E., 1996a, "The Path to Predicting Bypass Transition," ASME Paper 96-GT-199.

Mayle, R.E., 1996b, "Transition in a Separation Bubble," *Journal of Turbomachinery*, Vol. 118, pp. 752-759.

Menter, F.R., 1992, "Improved Two-Equation k-ω Turbulence Models for Aerodynamic Flows," NASA TM 103975.

Menter, F.R., 1993, "Zonal Two Equation k-w Turbulence Models for Aerodynamic Flows," AIAA Paper AIAA-93-2906, July 1993.

Menter, F.R., 1994, "Two-Equation Eddy-Viscosity Turbulence Models for Engineering Applications," *AIAA Journal*, Vol. 32, No.8, pp. 1594-1605.

Savill, A.M., 1992, "A synthesis of T3 test case predictions. In: Numerical simulation of unsteady flows and transition to turbulence," Eds. Pironneau, O., Rodi, W., Ryhming, I.L., Savill, A.M. and Truong, T.V., Cambridge University Press, pp. 404-442.

Savill, A.M., 1993a, "Some Recent Progress in The Turbulence Modeling of By-pass Transition," *Near-Wall Turbulent Flows,* edited by R.M.C. So, C.G. Speciale and B.E. Launder, Elsevier Science Publishers B.V., pp. 829-848.

Savill, A.M., 1993b, "Further Progress in The Turbulence Modeling of By-pass Transition," *Engineering Turbulence Modeling and Experiments* 2, edited by W. Rodi and F. Martelli, Elsevier Science Publishers B.V., pp. 583-592.

Savill, A.M., 2002, "By-pass Transition using Conventional Closures," *Closure Strategies for Turbulent and Transitional Flows*, edited by B.E. Launder and N.D. Sandsam, Cambridge University press, pp. 464-492.

Schmidt, R.C. and Patankar, S.V., 1991, "Simulating Boundary Layer Transition With Low-Reynolds-Number k-ε Turbulence Models: Part 2 – An Approach to Improving the Predictions," *Journal of Turbomachinery*, Vol. 113, pp. 18-26.

Schubauer, G.B. and Skramstad, H.K., 1948, "Laminar-boundary-layer oscillations and transition on a flat plate," NACA Rept. 909.
Schlichting, H., 1979, *Boundary Layer Theory*, McGraw-Hill, Inc..

Sinclair, C. and Wells, Jr., 1967, "Effects of Freestream Turbulence on Boundary-Layer Transition," *AIAA Journal*, Vol. 5, No. 1, pp. 172-174.

Steelant, J., and Dick, E., 2001, "Modeling of Laminar-Turbulent Transition for High Freestream Turbulence," *Journal of Fluids Engineering*, Vol. 123, pp. 22-30.

Suzen, Y.B., Huang, P.G., Hultgren, L.S. and Ashpis, D.E., 2001, "Predictions of Separated and Transitional Boundary Layers Under Low-Pressure Turbine Airfoil Conditions Using an Intermittency Transport Equation," AIAA Paper AIAA-2001-0446, Reno, NV.

Van Driest, E.R. and Blumer, C.B., 1963, "Boundary Layer Transition: Freestream Turbulence and Pressure Gradient Effects," *AIAA Journal*, Vol. 1, No. 6, pp. 1303-1306.

Versteeg, H.K. and Malalasekera, W., 1995, *An Introduction to Computational Fluid Dynamics*, Addison Wesley Longman Limited, Longman Group Ltd.

Warren, E.W. and Hassan, H.A. 1997, "Alternative to the e^n Method for Determining Onset of Transition," *AIAA Journal*, Vol. 36, No.1, pp. 111-113.

White, F.M., 1991, *Viscous Fluid Flow*, McGraw-Hill, Inc..

Wilcox, D.C., 1988, "Reassessment of the Scale-Determining Equation for Advanced Turbulence Models," *AIAA Journal*, Vol. 26, No.11, pp. 1299-1310.

Wilcox, D.C., 1994, "Simulation of Transition with a Two-Equation Turbulence Model," *AIAA Journal*, Vol. 32, No.2, pp. 247-255.

Wissink, J.G., 2002, "DNS of Separating, Low Reynolds Number Flow in a Turbine Cascade with Incoming Wakes,"*Engineering Turbulence Modelling and Experiments 5*, edited by W. Rodi and N. Fueyo, Elsevier Science Ltd., pp. 731-750.

Zhang, X.-F., Mahallati, A. and Sjolander, S.A., 2002, "Hot-Film Measurements of Boundary Layer Transition, Separation and Reattachment on a Low-Pressure Turbine Airfoil at Low Reynolds Numbers," AIAA-2002-3643, AIAA/ASME/SAE/ASEE Joint Propulsion Conference, Indianapolis, IA, July 2002.

Zhang, X.-F., 2002, "Hot-Film Measurements of the Steady and Unsteady Boundary Layer Development on a Low-Pressure Turbine Airfoil," Master's Thesis, Carleton University, 2002.

Zheng, X., Liu, C., Liu, F., and Yang, C., 1998, "Turbulent Transition Simulation Using the k-w Model," *International Journal for Numerical Methods in Engineering*, Vol. 42, pp. 907-926.

Appendix 1

The table below illustrates the range of uniform freestream turbulence intensity (FSTI) and pressure gradient (Thwaites pressure gradient parameter, λ_θ) for which the present transition model has been validated for. For all these cases the predicted transition onset based on the local momentum thickness Reynolds number ($Re_{\theta t}$) was found to be in good agreement with either experimentally measured values or those predicted by an empirical correlation.